POLITECNICO DI TORINO

Master Degree in Aerospace Engineering

Master Degree Thesis

Solar wind turbulence in the outer heliosphere

Supervisor
Prof. Daniela Tordella

Candidate
Davide Procacci

December 18 2020

Contents

List of Figures

List of Tables

Introduction

The heliosphere is filled by the solar wind (SW), a plasma originated from the nuclear interaction into the Sun, which continuously expands. This kind of medium can be classified as a collisionless plasma and it can be seen as a laboratory to study the turbulence. This allows improving the knowledge of the space phenomena, but it can also be an opportunity to observe physics events hardly reproducible on the Earth. In fact most of the fluids on our planet are neutral; understanding the plasma behaviour can lead to a revolution in many physical fields, e.g. the energy source as the nuclear fusion. Moreover, studying turbulence permits to enhance the knowledge of the structure of the heliosphere and to better understand the observation of the energetic particles.

The only way to understand the real heliosphere structure is by using the computational models, which need constraints. These boundary conditions are provided by both remote sensing and in-situ measurements.

The aim of this work is to summarise the state of the art regarding the SW turbulence, focusing on the data provided by the Voyager probes. The discussion was carried out on the basis of papers published by the team of Polytechnic of Turin, making a comparison of the results obtained. Data have been evaluated in three different regions: the interplanetary field, the inner heliosheath (IHS) and the outer heliosheath (OHS; a region of the LISM).

The interplanetary field represents the innermost part of the heliosphere. The data analysed in this region comes from the Voyager 2 (V2), which allows to evaluating both the velocity and the magnetic field of the plasma. Thanks to these data it was possible to perform a Fourier analysis and to obtain two different regimes of the magnetohydrodynamics (MHD): the energy injection (EI) and the inertial cascade (IC).

The second region of the heliosphere taken in consideration is the IHS, where the SW is slowed down by the interaction with the LISM. The data are provided by both the Voyager 1 (V1) and V2. Throughout the spectral analysis, two different regimes of the MHD cascade have been recognised, pointing out the difference between the V1 and V2 features detected. Moreover, differences are found with the interplanetary field.

The last region examined is the OHS, which is the part of the LISM disturbed by the presence of the heliosphere. On the official NASA website only the data supplied by V1 in the OHS are publicly available. These data do not allow distinguishing the different regimes of the non linear cascade, however, it is possible to define constraints on the LISM features. In this region new kinds of analysis have been considered as the Hilbert and the wavelet methods, which permit to study the phenomena in both the time-domain and the frequency-domain.

The present thesis has been written with the following outline. In chapter 1 the intention is to provide the general mathematical framework and the definition of plasma. In chapter 2, the birth of the solar wind is addressed by explaining the fundamental processes that produce the magnetic field and the plasma flow in the Sun. Broadening the perspective, the last heliosphere models are presented in chapter 3. Finally, chapter 4, tackles the turbulence of the magnetic field.

Chapter 1

Physics of the plasma

In this first chapter, the definition of *plasma* and its features are made explicit. Moreover, theories and models that describe the plasma behavior and the relevant fields of validity are shortly explained.

1.1 The fourth state of matter

The various states of matter are well defined by unique features. By increasing temperature, it is possible to pass from one state to another. So, if a gas sufficiently increases its own temperature, it will reach the state of plasma also called *the fourth state of matter*. Providing heat to a neutral gas leads to an increase of the internal energy in its four casts: translational, rotational, vibrational and electronics, resulting in dissociated atoms, namely ions and electrons, which make up a *ionized gas*.

Definition. Say plasma is dynamic system dominated by electromagnetic forces: the plasma is the ensemble of charged particles and force fields generated by the particles themselves (Chiuderi et al. 2012).

So, only the whole particles and fields define the plasma, as a matter of fact from a quantistic point of view, fields are seen as particles too (and viceversa).

The main peculiarity is the *quasi-neutrality condition*, in other words charged particles are free to move in the space, hence attract particles with opposite sign and reject those with same sign; therefore creating an electrostatic shielding area.

It is possible to distinguish a spherical volume, with radius r_s, in which the total electric charge is $Q(r_s) \simeq 0$. In order to provide a quantitative definition of quasi-neutrality condition it is necessary to recall the *Debye length* λ_D, defined as

$$\lambda_D = \sqrt{\frac{kT}{4\pi e^2 n_0}},$$

which is valid only if $\bar{d} << \lambda_D$, whith $\bar{d}$ mean path between particles.

So the quasi-neutrality condition is written as

$$n\lambda_D^3 >> 1$$

where: $\bar{d} \simeq n^{-1/3}$ [1]. This leads to the hypothesis of electrostatic energy being neglectable, compared to thermal energy.

[1] n number density.

It is necessary to introduce the *plasma frequency*, which is a rapid oscillation of the particle density in a conducting media. It is common to refer this frequency both to electrons f_{pe} and protons f_{pi}. Electron-wise, protons are fixed in the space, because electrons are less massive than protons and so they are faster. Namely, an oscillation in electrons distribution has no effect on protons distribution.
The local violation of the quasi-neutrality condition produces an electric field, which induces harmonic motion of electrons with frequency f_{pe}.

Another plasma feature is the *collision frequency* ν_c, which determines the amount of collisions in the unit time and allows calculating the characteristic time with a specific population reaching the thermal equilibrium. Indeed *thermalization* is the process by which two different populations, initially in a non-equilibrium state, reaches thermal equilibrium through collisions.

Plasma flow is made by two different motions: ordered and disordered ones. The first is defined by f_{pe} and the latter by ν_c. Hence, if the plasma flow were orderly, it would be $f_{pe} >> \nu_c$.

When motion occurs in an electric field, the contribution of the magnetic field arises, as a matter of fact, the interaction between charged particles and magnetic field, creating a circular motion with frequency $f_c = |e|B/(mc)$, called *cyclotron frequency* (or Larmor frequency). This frequency will be calculated for both protons and electrons.
The same frequency allows to estimate when relativistic effects are relevant, namely when $kT \gtrsim mc^2$. Instead, quantistic effects, when the typical length of plasma is comparable to De Broglie length - hence when there is high density and/or high temperature - are not negligible.

1.2 General (or orbit) theory

Overlooking relativistic and quantistic effects, governing equations can be studied with a classical approach. Plasma is seen as charged particles in an empty space.
Maxwell equations are:

$$\nabla \times \boldsymbol{E} = -\frac{1}{c}\frac{\partial \boldsymbol{B}}{\partial t} \tag{1.1a}$$
$$\nabla \times \boldsymbol{B} = \frac{1}{c}\frac{\partial \boldsymbol{E}}{\partial t} + \frac{4\pi}{c}\boldsymbol{J} \tag{1.1b}$$
$$\nabla \cdot \boldsymbol{E} = 4\pi q \tag{1.1c}$$
$$\nabla \cdot \boldsymbol{B} = 0 \tag{1.1d}$$

where q is the charge density and $\boldsymbol{J}$ is the current density.
The continuity equation for the charged particle has to be considered

$$\nabla \cdot \boldsymbol{J} + \frac{\partial q}{\partial t} = 0. \tag{1.2}$$

Relations (1.1c) and (1.1d) are linearly dependent from other equations, hence it is necessary to add the motion equation for every particles

$$m_i \ddot{\boldsymbol{r}}_{\boldsymbol{i}} = e_i\big(\boldsymbol{E} + \frac{1}{c}\dot{\boldsymbol{r}}_{\boldsymbol{i}} \times \boldsymbol{B}\big). \tag{1.3}$$

The whole number of equations is $3N + 6$ (N is the number of particles), but the unknowns are $3N + 10$ ($\boldsymbol{E}, \boldsymbol{B}, \boldsymbol{J}, q$). Therefore, charge and current density have to be related to the fundamental dynamical quantities.

$$q(\boldsymbol{r},t) = \sum_{i=1}^{N} e_i \delta[\boldsymbol{r} - \boldsymbol{r_i}(t)] \tag{1.4a}$$

$$\boldsymbol{J}(\boldsymbol{r},t) = \sum_{i=1}^{N} e_i \boldsymbol{v} \delta[\boldsymbol{r} - \boldsymbol{r_i}(t)]\delta[\boldsymbol{v} - \boldsymbol{v_i}(t)] \tag{1.4b}$$

A set of equation made of (1.1), (1.3) and (1.4) theoretically have a solution, but it is impossible to find it. However, claiming to know the solution, there are too much information to verify with purely exerimental data.

This kind of description of the plasma physics, in which microscopic features are negligible, it is also called *orbit theory*. It is very useful for rarefied gases because it is possible to ignore particle interactions.

1.3 Kinetic theory

In standard situations it is complicated to use the classical approach for the high number of particles present. This makes it difficult to know the initial position and momentum for every particle. Moreover, assuming to know the initial conditions, the computational capacity nowadays available is not sufficient and only a few conditions can be determined (Izmodenov et al. 2006). In order to reduce computational costs it is helpful to adopt a *statistical approach*, but information about particles trajectory get lost.

For the statistical approach, it is more advisable to introduce the *phase space*, defined by $\boldsymbol{r}$ and $\boldsymbol{v}$ (6D). In this way the dynamical state of each particle is described in a given moment.
Considering an elementary volume $dr = dxdydz$, it is possible to define the *density function*, which defines the average number of particles contained in dr. This volume must be large enough to contain a number of particles sufficient to obtain significant statistical measures. In other words, the density function must be continuous and it is assumed to be proportional to dr. So

$$dN = f(\boldsymbol{r},\boldsymbol{v},t)d\boldsymbol{r}d\boldsymbol{v} \tag{1.5}$$

where f is called *distribution function* and dN is the average number of particles between $(\boldsymbol{r}, \boldsymbol{r}+d\boldsymbol{r})$ and $(\boldsymbol{v}, \boldsymbol{v}+d\boldsymbol{v})$.
The total number of particles (number density) is

$$N = \int_{V_6} f(\boldsymbol{r},\boldsymbol{v},t)d\boldsymbol{r}d\boldsymbol{v}$$

constant in the absence of relativistic or nuclear processes.
The nabla operator will be written as follows, to take into account the variation of f with respect to $\boldsymbol{r}$ and $\boldsymbol{v}$.

$$\nabla \to \nabla + \nabla_v$$

Hence, the continuity equation in the phase space is

$$\frac{\partial f}{\partial t} + \nabla \cdot (f\boldsymbol{v}) + \nabla_v \cdot (f\boldsymbol{a}) = 0$$

where $\boldsymbol{a}$ is the elementary volume acceleration.
Expanding

$$\frac{\partial f}{\partial t} + f\nabla \cdot \boldsymbol{v} + \boldsymbol{v} \cdot \nabla f + f\nabla_v \cdot \boldsymbol{a} + \boldsymbol{a} \cdot \nabla_v f = 0,$$

it is worth knowing that $\boldsymbol{r}$ and $\boldsymbol{v}$ are independent, therefore $\nabla \cdot \boldsymbol{v} = 0$. Besides, the acceleration is $\boldsymbol{a} = \boldsymbol{F}/m$ and the only dependent force velocity is the Lorentz force

$$\boldsymbol{F_L} = \left(\frac{e_0}{c}\right)(\boldsymbol{v} \times \boldsymbol{B})$$

but $\nabla_v \cdot \boldsymbol{F_L} = 0$, so

$$\frac{\partial f}{\partial t} + \boldsymbol{v} \cdot \nabla f + \frac{\boldsymbol{F}}{m} \cdot \nabla_v f = 0. \tag{1.6}$$

It is important to discuss the $\boldsymbol{F}$-term. Until now, it has been assumed that all particles inside the elementary volume have the same acceleration. This assumption works only for *collective effects*. This kind of effects generates slowly variable forces with position, which lead to regular particle paths. But there are forces generated by the particles interaction too. These are called *collisional effects* and take to abrupt trajectory variation.
Hence, the collisional contribution can be written as

$$\left(\frac{\partial f}{\partial t}\right)_{coll} = -\frac{\boldsymbol{F}_{coll}}{m} \cdot \nabla_v f,$$

where $\boldsymbol{F} = \boldsymbol{F}_{coll} + \boldsymbol{F}_{SlowlyVariable}$.
Replacing this one in the equation (1.6), one obtains the so called *kinetic equation*

$$\frac{\partial f}{\partial t} + \boldsymbol{v} \cdot \nabla f + \frac{\boldsymbol{F}}{m} \cdot \nabla_v f = \left(\frac{\partial f}{\partial t}\right)_{coll} \tag{1.7}$$

where terms without subscript are collective terms. The group force results to be

$$\boldsymbol{F} = e_0 \left(\boldsymbol{E} + \frac{1}{c}\boldsymbol{v} \times \boldsymbol{B}\right) + \boldsymbol{f}$$

with $\boldsymbol{f}$ being the non-electromagnetic force term. Neglecting this one only the electromagnetic force remains, hence the equation (1.7) becomes

$$\frac{\partial f}{\partial t} + \boldsymbol{v} \cdot \nabla f + \frac{e_0}{m}\left(\boldsymbol{E} + \frac{1}{c}\boldsymbol{v} \times \boldsymbol{B}\right) \cdot \nabla_v f = \left(\frac{\partial f}{\partial t}\right)_{coll}, \tag{1.8}$$

which has to be associated with both Maxwell equations and the $(\partial f/\partial t)_{coll}$ model relations.

Through these equations it is possible to describe either neutral gases or plasmas. The difference is in the model selected to specify the collisional term.
The most important models are:

- *Vlasov* model, where collisional term is neglected

$$\frac{\partial f}{\partial t} + \boldsymbol{v} \cdot \nabla f + \frac{e_0}{m}\left(\boldsymbol{E} + \frac{1}{c}\boldsymbol{v} \times \boldsymbol{B}\right) \cdot \nabla_v f = 0, \tag{1.9}$$

  provide good rarefied gases description;

- *Boltzmann* model, where only elastic binary collision is considered

$$\frac{\partial f}{\partial t} + \boldsymbol{v} \cdot \nabla f + \frac{e_0}{m}\left(\boldsymbol{E} + \frac{1}{c}\boldsymbol{v} \times \boldsymbol{B}\right) \cdot \nabla_v f = S(f) \tag{1.10}$$

  with $S(f)$ called *integral of collisions* (Izmodenov et al. 2006). A neutral gas is well described;

- *Fokker-Planck* model, to consider the multiple particle interactions, the Boltzmann collisional term must be modified.

It is impossible to find an analytic solution for any model chosen, and it is very difficult to reach a numerical solution. Actually, the only known solutions are derived from symmetrical problems or apply to an average speed process. The latter method leads to a loss of information about the velocity of each particle, therefore it is necessary to redefine the (1.5) in the following way

$$n(\boldsymbol{r},t) = \int f(\boldsymbol{r},\boldsymbol{v},t)d\boldsymbol{v} \tag{1.11}$$

where $n(\boldsymbol{r},t)$ is the *number density* and quantifies the mean number of particles between $\boldsymbol{r}$ and $\boldsymbol{r}+d\boldsymbol{r}$, no matter their speed.
The average of a generic function dependent on velocity $\phi(\boldsymbol{v})$ (also called *moments*) is

$$\langle\phi\rangle = \frac{1}{n(\boldsymbol{r},t)}\int \phi(\boldsymbol{v})f(\boldsymbol{r},\boldsymbol{v},t)d\boldsymbol{v}, \tag{1.12}$$

whereby

$$n\langle\phi\rangle = \int \phi(\boldsymbol{v})f(\boldsymbol{r},\boldsymbol{v},t)d\boldsymbol{v}, \tag{1.13}$$

multiplying by (1.6) and integrating in phase space, one has that:

the first term is

$$\int \phi(\boldsymbol{v})\frac{\partial f}{\partial t}d\boldsymbol{v} = \frac{\partial}{\partial t}\left(n\langle\phi\rangle\right);$$

the second term is

$$\int \phi\boldsymbol{v}\cdot\nabla f d\boldsymbol{v} = \nabla\cdot\left(n\langle\boldsymbol{v}\phi\rangle\right);$$

the third term has to be decomposed in electromagnetic and other external forces

$$\int \phi\frac{\boldsymbol{F}}{m}\cdot\nabla_v f d\boldsymbol{v} = \frac{1}{m}\int \phi\left(\boldsymbol{f}\cdot\nabla_v f\right)d\boldsymbol{v} + \frac{e_0}{m}\int \phi\left(\boldsymbol{E}+\frac{1}{c}\boldsymbol{v}\times\boldsymbol{B}\right)\cdot\nabla_v f d\boldsymbol{v} = \\ -\frac{n}{m}\boldsymbol{f}\cdot\langle\nabla_v\phi\rangle - \frac{ne_0}{m}\langle\left(\boldsymbol{E}+\frac{1}{c}\boldsymbol{v}\times\boldsymbol{B}\right)\cdot\nabla_v f\rangle;$$

hence, the *general transport moments equation* is written as

$$\frac{\partial}{\partial t}\left(n\langle\phi\rangle\right) + \nabla\cdot\left(n\langle\boldsymbol{v}\phi\rangle\right) - \frac{n}{m}\boldsymbol{f}\cdot\langle\nabla_v\phi\rangle - \frac{ne_0}{m}\langle\left(\boldsymbol{E}+\frac{1}{c}\boldsymbol{v}\times\boldsymbol{B}\right)\cdot\nabla_v f\rangle = \int\phi\left(\frac{\partial f}{\partial t}\right)_{coll}d\boldsymbol{v} \tag{1.14}$$

where it was assumed that $f\phi\to 0$ for $|\boldsymbol{v}|\to\infty$. Obviously the collisional term still depends on the chosen model.

Now it is clear that the distribution function assumes a physical meaning which is comparable to experimental data.
The simplified assumption of average speed leads to *Landau damping*. In fact, it is impossible to know if a group of particles behaves differently from the average.

1.4 Simplified models: fluid approximation

The distribution functions are essential to find a solution for kinetic equation, but these functions are not always known. Only in few cases f are known. So it is important to find some ways to resolve this kind of problems. Normally the *fluid models* are used. They consist of looking for a set of differential equations where there are only moments, without considering distribution functions.

The moments relation ϕ is a generic function linearly dependent on velocity. So, the n-order moment of the distribution function f is written as

$$n - moment = \int (v_i v_j \dots v_k) f(\boldsymbol{r}, \boldsymbol{v}, t) d\boldsymbol{v} = n(\boldsymbol{r}, t) \langle (v_i v_j \dots v_k) \rangle.$$

To solve the problem, the general moments equation is the starting point. One equation for each moment will be written. So there will be infinite equations, because there are moments of higher order in the general equation. Namely, if the n order equation is considered, then the $\langle \boldsymbol{v}\phi \rangle$ will be $n+1$ order moment. This is the *closure problem.*

Since $\phi(\boldsymbol{v})$ is linearly dependent on velocity, it is correct to define the n-order as

n=0 : $\phi(\boldsymbol{v}) = m$;

n=1 : $\phi(\boldsymbol{v}) = m\boldsymbol{v}$;

n=2 : $\phi(\boldsymbol{v}) = \frac{1}{2} m v^2$.

In a plasma there are many kinds of chemical species (s), hence there are many distribution functions f_s, one for each species. Hence, kinetic equations are written as

$$\frac{\partial f_s}{\partial t} + \boldsymbol{v} \cdot \nabla f_s + \frac{\boldsymbol{F}}{m_s} \cdot \nabla_v f_s = \left(\frac{\partial f_s}{\partial t} \right)_{coll}. \tag{1.15}$$

1.4.1 Two-fluids model

Assuming a completely ionized hydrogen gas, there are only protons and electrons. Moreover, non-electromagnetic forces are neglected $\boldsymbol{f} = 0$.
Using the previous definition of $\phi(\boldsymbol{v})$, and the hypothesis just described, the zero-order equations become

$$\frac{\partial n_s}{\partial t} + \nabla \cdot \left(n_s \boldsymbol{u}^{(s)} \right) = m \left(\frac{\partial n_s}{\partial t} \right)_{coll}, \tag{1.16}$$

also called *continuum equation*, where

$$n_s = \int f_s(\boldsymbol{r}, \boldsymbol{v}, t) d\boldsymbol{v}$$

and

$$\boldsymbol{u}^{(s)} = \frac{1}{n_s} \int \boldsymbol{v} f_s d\boldsymbol{v}.$$

The first-moment equations become

$$\frac{\partial}{\partial t} \left(n_s m_s u_i^{(s)} \right) + \frac{\partial}{\partial x_k} \left(n_s m_s \langle v_i v_k \rangle_s \right) - e_s n_s E_i - \frac{e_s n_s}{c} \left(\boldsymbol{u}^{(s)} \times \boldsymbol{B} \right)_i = \left[\int m_s \boldsymbol{v} \left(\frac{\partial f_s}{\partial t} \right)_{coll} d\boldsymbol{v} \right]_i, \tag{1.17}$$

written for components i.
A pressure tensor written as

$$P_{ik}^{(s)} = n_s m_s \langle w_i w_k \rangle = P^{(s)} \delta_{ik} + \Pi_{ik}^{(s)}$$

leads to the *momentum equations*

$$\frac{\partial}{\partial t}\left(n_s m_s u_i^{(s)}\right) + \frac{\partial}{\partial x_k}\left(n_s m_s u_i^{(s)} u_k^{(s)} + P_{ik}^{(s)}\right) - e_s n_s E_i - \frac{e_s n_s}{c}\left(\boldsymbol{u}^{(s)} \times \boldsymbol{B}\right)_i = \left[\int m_s \boldsymbol{v} \left(\frac{\partial f_s}{\partial t}\right)_{coll} d\boldsymbol{v}\right]_i . \quad (1.18)$$

In the same way it is possible to derive the second-order equation

$$\frac{\partial}{\partial t}\left[\frac{1}{2} m_s n_s \left(u^{(s)}\right)^2 + \frac{3}{2} P^{(s)}\right] + \frac{\partial}{\partial x_k}\left\{\left[\frac{1}{2} n_s m_s \left(u^{(s)}\right)^2 + \frac{5}{2} P^{(s)}\right] u_k + u_i^{(s)} \Pi_{ik}^{(s)} + q_k^{(s)}\right\} - e_s n_s E_i u_i^{(s)} = \int \frac{1}{2} m_s v^2 \left(\frac{\partial f_s}{\partial t}\right)_{coll} d\boldsymbol{v} \quad (1.19)$$

also called *energy equation.* Collisional terms of momentum and energy equations, could be shortly written as

$$\boldsymbol{R}^{(s)} = \int m_s \boldsymbol{v} \left(\frac{\partial f_s}{\partial t}\right)_{coll} d\boldsymbol{v}$$
$$Q^{(s)} = \int \frac{1}{2} m_s v^2 \left(\frac{\partial f_s}{\partial t}\right)_{coll} d\boldsymbol{v}$$

where

$$C(s, s') = \left(\frac{\partial f_s}{\partial t}\right)_{coll}$$

with $s, s' = e, p$. This latter term considers the collisions between the same species and different species. Differently from a neutral gas, in a plasma the particles do not have the same bulk.
From the conservation of particles number

$$\int C(s, s') d\boldsymbol{v} = 0$$

independently from which particle species interact.
When the same particles interface, the collisional terms become

$$\int m_s \boldsymbol{v} C(s, s) d\boldsymbol{v} = 0$$
$$\int \frac{1}{2} m_s v^2 C(s, s) d\boldsymbol{v} = 0,$$

and for different species

$$\int m_s \boldsymbol{v} C(s, s') d\boldsymbol{v} + \int m'_s \boldsymbol{v} C(s', s) d\boldsymbol{v} = 0 \quad (1.20a)$$

$$\int \frac{1}{2} m_s v^2 C(s, s') d\boldsymbol{v} + \int \frac{1}{2} m'_s v^2 C(s', s) d\boldsymbol{v} = 0, \quad (1.20b)$$

so for the continuum equation the collisional term is always zero. For the other collisional terms the same species interaction contribution is null. As a matter of fact, when two identical particles interact the mass is the same and if only elastic collision is considered , the momentum and the energy do not change.
For these reasons, collisional terms can be simplified and only the different species part remains, so

$$\left(\frac{\partial n_s}{\partial t}\right)_{coll} = 0$$
$$\boldsymbol{R}^{(s)} = \int m_s \boldsymbol{v} C(s, s') d\boldsymbol{v}$$
$$Q^{(s)} = \int \frac{1}{2} m_s v^2 C(s, s') d\boldsymbol{v}.$$

Replacing these above into (1.16), (1.18) and (1.19), there is a set of equations that describe the problem as two different fluids interacting. Furthermore, it is worth to notice that momentum and energy loss from one species is gained by the other one.

$$\boldsymbol{R}^{(e)} = -\boldsymbol{R}^{(p)}$$
$$Q^{(e)} = -Q^{(p)}$$

The temperatures of the two fluids could be different, as heat fluxes.

Considering this set of equations, the closure problem still remains. To solve this issue, two fluids should be supposed to be in *locally* thermodynamic equilibrium, each at its own temperature. The coupling, between the equations, still remains and it is impossible to close the problem if exchange momentum and energy terms are not expressed as macroscopic quantities.

This type of model describes very well the behaviour of two different species in thermodynamic non-equilibrium. This is possible in a collisionless plasma (rarefied plasma) due to the low collisions efficiency among different species, as solar wind (SW).

1.4.2 One-fluid model

The two-fluids model is still too complicated to solve. So, it is important to find another model to further simplify the discussion.
An artificial fluid can be used assuming the same temperature for the two fluids. This hypothesis leads to the concepts of:

- *total number density* $n = n_e + n_p$;
- *mass density* $\rho(\boldsymbol{r}, t) = n_p m_p + n_e m_e$;
- *charge density* $q(\boldsymbol{r}, t) = e(n_p - n_e)$;
- *current density* $\boldsymbol{J}(\boldsymbol{r}, t) = e(n_p \boldsymbol{u}^{(p)} - ne\boldsymbol{u}^{(e)})$;
- *bulk velocity* $\boldsymbol{U} = \frac{m_e n_e \boldsymbol{u}^{(e)} + m_p n_p \boldsymbol{u}^{(p)}}{m_e n_e + m_p n_p}$;

where for the quasi-neutrality condition $n_e \simeq n_p$, so the bulk velocity is a sort of centre mass velocity.
Now it is possible to re-write the governing equations. The *continuum equation* for one-fluid model is

$$\frac{\partial \rho}{\partial t} + \nabla \cdot (\rho \boldsymbol{U}) = 0 \tag{1.21}$$

and the charge continuum equation is

$$\frac{\partial q}{\partial t} + \nabla \cdot \boldsymbol{J} = 0. \tag{1.22}$$

Obtaining the motion relation is more complicated than the previous two ones. This because the pressure tensor $P_{ik}^{(s)}$ is defined from the decomposition of the single species velocity

$$\boldsymbol{v} = \boldsymbol{u} + \boldsymbol{w}$$

where $\boldsymbol{u} = \langle \boldsymbol{v} \rangle$ is the mean velocity and represents the organized motion, $\boldsymbol{w}$ is the peculiar velocity and represents the chaotic motion. Hence, $P_{ik}^{(s)}$ is defined by $\boldsymbol{w} = \boldsymbol{v} - \boldsymbol{u}^{(s)}$, but it should be related to $\boldsymbol{w'} = \boldsymbol{v} - \boldsymbol{U}$. Therefore, the new peculiar velocity is

$$\langle \boldsymbol{w'} \rangle_s = \boldsymbol{u}^{(s)} - \boldsymbol{U} \neq 0$$

that provides new terms in the (1.18).
Introducing the total pressure tensor

$$P_{ik} = P_{ik}^{(e)} + P_{ik}^{(p)},$$

it is possible to write the *momentum equation*

$$\rho \frac{\partial U_i}{\partial t} + \rho U_k \frac{\partial U_i}{x_k} = -\frac{\partial P_{ik}}{\partial x_k} + qE_i + \frac{1}{c} \left(\boldsymbol{J} \times \boldsymbol{B} \right)_i . \tag{1.23}$$

Now, kinetic temperature can be introduced

$$T^{(s)} = \frac{P_{ii}^{(s)}}{3 n_s k}$$

and the energy equation can be determined following the same method as before and redefining heat flux $\boldsymbol{q}^{(s)}$ with respect to peculiar velocity $\boldsymbol{w'}$. Hence, the total heat flux is $\boldsymbol{q} = \boldsymbol{q}^{(e)} + \boldsymbol{q}^{(p)}$, therefore the *energy equation* is

$$\frac{\partial}{\partial t} \left(\frac{1}{2} \rho U^2 + \frac{3}{2} P \right) + \frac{\partial}{\partial x_i} \left[U_i \left(\frac{1}{2} \rho U^2 + \frac{5}{2} P \right) + \Pi_{ik} U_k + q_i \right] - J_k E_k = 0 \tag{1.24}$$

manipulating $\boldsymbol{J} \cdot \boldsymbol{E}$ term can be written as

$$\boldsymbol{J} \cdot \boldsymbol{E} = -\nabla \cdot \boldsymbol{S} - \frac{\partial}{\partial t} \left(\frac{B^2}{8\pi} + \frac{E^2}{8\pi} \right)$$

where $\boldsymbol{S} = (c/4\pi)(\boldsymbol{E} \times \boldsymbol{B})$ is the Poynting vector, which represents the electromagnetic energy flux. Replacing it in (1.24)

$$\frac{\partial}{\partial t} \left(\frac{1}{2} \rho U^2 + \frac{3}{2} P + \frac{B^2}{8\pi} + \frac{E^2}{8\pi} \right) + \frac{\partial}{\partial x_i} \left[U_i \left(\frac{1}{2} \rho U^2 + \frac{5}{2} P \right) + \Pi_{ik} U_k + q_i + S_i \right] = 0$$

it is worth seeing that the dissipative effects modify the total energy. Moreover, magnetic energy can be turned into thermal or kinetic energy if diffusivity η is different from zero.

The set of equations (1.21), (1.22), (1.23) and (1.24), is made up of 21 unknowns and 12 scalar equations. Considering the closure problem, a vectorial equation is still missing.

The momentum equation was derived by adding motion relation (1.18) for each species, so the last equation can be found by subtracting them. To achieve this result, the (1.18) must be multiplied by e_s/m_s, summarized, taking into account $m_e << m_p$, $n_e \simeq n_p$, and neglecting viscous terms and external forces. The *generalized Ohm's law* is the last equation

$$E_i + \frac{1}{c}(\boldsymbol{U} \times \boldsymbol{B})_i - \frac{J_i}{\sigma} = \frac{m_e}{e^2 n_e}\left[\frac{\partial J_i}{\partial t} + \frac{\partial}{\partial x_k}(J_i U_k + J_k U_i)\right] + \frac{1}{e n_e c}(\boldsymbol{J} \times \boldsymbol{B})_i - \frac{1}{e n_e}\frac{\partial P_{ik}^{(e)}}{\partial x_k} \quad (1.25)$$

where

$$\sigma = \frac{e^2 n_e}{m_e \nu_{ep}}$$

is the electrical conductivity of plasma[2]

Supposing that the closure problem has been solved, the Ohm's general equation and Maxwell's equations complete the equations system, which does not provide a unique solution. There are two ways to give a single solution: the first is overlooking thermal effects. In other words, an ideal plasma is considered where there are no collisions. The second method is assuming a collisional plasma, where the gas is in locally thermal equilibrium, hence the distribution function complies with the Maxwellian one.

1.5 Magnetohydrodynamic regime and equations

The one-fluid collisional model greatly simplifies the treatment compared to other models, but it includes too many solutions. Hence, the need to narrow the validity of the solutions *regime*, e.g. hydrodynamic approximation is valid for a fully ionized collisionless plasma. Determining the approximation means changing the equations.

Firstly, characteristic quantities, such as time τ and length $\mathcal{L}$, have to be defined. Then it is possible to introduce the typical fluid velocity value

$$\mathcal{U} \simeq \mathcal{L}/\tau, \quad \mathcal{U} << c$$

where c is the light speed. The first relation implies that the typical velocity of hydrodynamic phenomena has the same magnitude of the electromagnetic ones. The latter means that relativistic effects are neglected. In other words, at frequencies lower than the ion cyclotron ones, the behaviour of plasma can be modelled through MHD approximation.

Through dimensional analysis, Maxwell's equations become

$$\nabla \times \boldsymbol{E} = -\frac{1}{c}\frac{\partial \boldsymbol{B}}{\partial t} \quad (1.26)$$

$$\nabla \times \boldsymbol{B} = \frac{4\pi}{c}\boldsymbol{J}, \quad (1.27)$$

hence, overlooking displacement current means that MHD is a *low frequency* regime. Indeed, the displacement current becomes important when electric field rapidly changes over time.
The *charge continuum equation* is rewritten as

$$\nabla \cdot \boldsymbol{J} = 0, \quad (1.28)$$

the *continuum equation* as

$$\frac{\partial \rho}{\partial t} + \nabla \cdot (\rho \boldsymbol{U}) = 0 \quad (1.29)$$

[2] ν_{ep} is the average collision frequency between s and s'.

the *momentum equation*[3] as

$$\rho\frac{d\boldsymbol{U}}{dt} = -\nabla P + \frac{1}{c}\boldsymbol{J}\times\boldsymbol{B}, \tag{1.30}$$

and the *energy equation* as

$$\frac{1}{\gamma-1}\rho^{\gamma}\frac{d}{dt}\left(P\rho^{-\gamma}\right) = \frac{J}{\sigma}. \tag{1.31}$$

By appropriately combining the (1.26) with the following

$$\boldsymbol{E} + \frac{1}{c}\boldsymbol{U}\times\boldsymbol{B} = \frac{\boldsymbol{J}}{\sigma}$$

one gets the *magnetic induction equation*

$$\frac{\partial\boldsymbol{B}}{\partial t} = \nabla\times(\boldsymbol{U}\times\boldsymbol{B}) + \eta\nabla^2\boldsymbol{B} - \nabla\eta\times(\nabla\times\boldsymbol{B}) \tag{1.32}$$

where

$$\eta = \frac{c^2}{4\pi\sigma}$$

is the magnetic diffusivity. To complete the set of equations, one needs the current density

$$\boldsymbol{J} = \frac{c}{4\pi}(\nabla\times\boldsymbol{B})$$

and the charge density

$$q = \frac{1}{4\pi}(\nabla\cdot\boldsymbol{E}).$$

Using MHD is the simplest way to describe a plasma as a continuous conductive medium, because it is impossible to reduce the number of equations further.

It is interesting to know that, after some manipulations, the equation (1.30) can be rewritten as

$$\rho\frac{d\boldsymbol{U}}{dt} = -\nabla\left(P + \frac{B^2}{8\pi}\right) + \frac{1}{4\pi}\nabla(\boldsymbol{B}\cdot\nabla)\boldsymbol{B} \tag{1.33}$$

where $P = nkT$ is the kinetic pressure and $B^2/8\pi$ is the magnetic pressure. The latter equation can be written in a different way keeping in mind that $\nabla\cdot\boldsymbol{B} = 0$, hence

$$\rho\frac{dU_i}{dt} = \frac{\partial}{\partial x_k}T_{ik}$$

where T_{ik} is a tensor. By rotating the reference system and bringing the z axis parallel to the magnetic field, the tensor becomes

$$\begin{pmatrix} P+\frac{B^2}{8\pi} & 0 & 0 \\ 0 & P+\frac{B^2}{8\pi} & 0 \\ 0 & 0 & P-\frac{B^2}{8\pi} \end{pmatrix}$$

one can always find this tensor locally. There are two types of contribution: the pressure and the tension term. The former is made up of the kinetic plus the magnetic pressure and it is isotropic. The latter only works when the magnetic field lines are curved, straightening them. In other words,

[3] Remembering that $\frac{d}{dt} = \frac{\partial}{\partial t} + \boldsymbol{U}\cdot\nabla$ is the Lagrangian (or material) derivative.

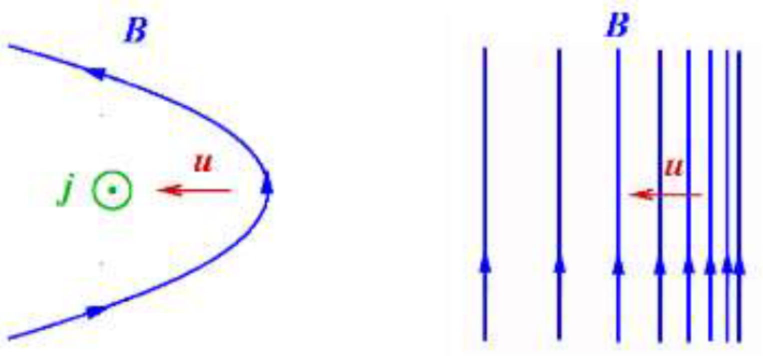

Figure 1.1: The blue lines represent the magnetic field, the red ones are the plasma velocity and the green circle represents the current density, which diretion is obtained using the right-hand rule. On the left, the magnetic tension acts only on curved lines, which behave as elastic bands. On the right, the magnetic pressure acts on the force lines and spread them toward the weaker magnetic field zones. (Bemporad 2019)

the pressure term works perpendicularly on the force lines and spreads them toward the weaker magnetic field. The tension term acts only on curved force lines, which behave as elastic bands and tend to become linear, as shown in figure 1.1. Therefore the Lorentz's force supports the magnetic field topology change.
The relative importance between the two terms is quantified by

$$\beta = \frac{P}{B^2/8\pi} \tag{1.34}$$

when $\beta >> 1$, hydrodynamic effects are more important than magnetic ones and vice versa when $\beta << 1$.

1.5.1 The magnetic Reynolds number

By using a kinematic approach, whereby the field $\boldsymbol{U}$ is considered as known, the Faraday equation (1.32) says that

$$\frac{\partial \boldsymbol{B}}{\partial t} = \nabla \times (\boldsymbol{U} \times \boldsymbol{B}) + \eta \nabla^2 \boldsymbol{B}$$

assuming $\eta =$const. The temporal variation of the magnetic field is due both to a convective term, which is associated to mass motion, and to a diffusive term. This kind of contributions act on different temporal scales, therefore, to quantify the relative importance of the two terms *Reynolds' magnetic number* will be defined as

$$R_m = \frac{\tau_d}{\tau_c} = \frac{\mathcal{U}\mathcal{L}}{\eta} \tag{1.35}$$

where, if $\mathcal{U} = c_a$ (Alfvén velocity), it is called Lundquist number too.

The magnetic diffusion

When $R_m << 1$, the convective term can be neglected and the Faraday equation becomes

$$\frac{\partial \boldsymbol{B}}{\partial t} = \eta \nabla^2 \boldsymbol{B}$$

therefore, it is a linear differential equation. Now, the Fourier analysis can be used

$$\boldsymbol{B}(\boldsymbol{r},t) = \int \boldsymbol{B}(\boldsymbol{k},\omega)e^{i(\boldsymbol{k}\cdot\boldsymbol{r}-\omega t)}d\boldsymbol{k}d\omega$$

which can be included in the first equation.
The magnetic field behaviour is described by

$$\boldsymbol{B}(\boldsymbol{r},t) = \int \boldsymbol{B}(\boldsymbol{k})e^{i\boldsymbol{k}\cdot\boldsymbol{r}}e^{-\eta k^2 t}d\boldsymbol{k} \tag{1.36}$$

where, different considerations can be done:

1. the general Fourier components of generic magnetic field decrease over time;
2. the magnetic energy value decreases over time due to the resistivity effect, which turns the magnetic energy into kinetic and thermal energy[4];
3. an higher k value or, in other terms, a shorter wave length corresponds to smaller magnetic field fluctuations.

So, the magnetic field becomes more regular over time.

The magnetic convection

When $R_m >> 1$, the conductivity is high and/or the length scale is large, therefore the diffusive term can be neglected $\eta = 0$, then the Farady equation becomes

$$\frac{\partial \boldsymbol{B}}{\partial t} = \nabla \times (\boldsymbol{U} \times \boldsymbol{B})$$

from which derives the

Theorem (Alfvén)**.** *Through any closed line the magnetic field, which moves with the flow, is constant over time (Chiuderi et al. 2012, p. 73).*

This theorem provides the notion of the freezing of the force line, which means that all the particles that lie on a force line will follow that force line. In other words, the $\boldsymbol{B}$ force lines can be twisted, but the topology of the magnetic field will not be changed. In an ideal plasma ($\eta = 0$) magnetic field and matter are linked together and the dynamic depends on the value of β. If $\beta > 1$, the kinetic pressure is more important than the magnetic one, hence, the matter carries the magnetic field along with it. Furthermore, if $\beta < 1$, magnetic pressure is higher than kinetic pressure, the magnetic field drags the matter.

It is worth to know that natural plasmas behave like the ideal ones, but the resistive term can not be overlooked. Indeed, this examination is based on a dimensional analysis, therefore these are average results. The ideal plasma condition can be not true in some cases ($\boldsymbol{U} = 0$, $\boldsymbol{U} \times \boldsymbol{B}$ and $\nabla \times (\boldsymbol{U} \times \boldsymbol{B}) = 0$), so natural plasma can be handled as ideal plasma where locally the resistivity cannot be neglected.

[4] When $\partial \boldsymbol{B}/\partial t \neq 0$ arise an electric field which can accelerate charged particles

1.5.2 The Elsässer's variables

The dynamic stability is the study of the effect of the perturbations on the equilibrium state. This means that a physical quantity oscillates around its average value. Hence, it is possible to write the generic quantity as

$$f = f_0 + \epsilon f_1$$

where f_0 is the equilibrium (background) value and ϵf_1 is the perturbation ($\epsilon << 1$ states that the fluctuation is small compared to the average value). From now on taking the ϵ for granted will be neglected.

Considering the incompressible case of MHD equations, it is worthwhile to highlight that the bulk velocity background vector can be eliminated through a Galileian transformation, but this is not possible with the magnetic field. Thus, a change of variables is needed to perform a more symmetrical form of the governing relations. Saying the Elsässer's variables $\boldsymbol{z}^{\pm} = \boldsymbol{U} \pm \boldsymbol{B}/\sqrt{4\pi\rho}$, the MHD equations for an ideal plasma become

$$\frac{\partial \boldsymbol{z}^{\pm}}{\partial t} + (\boldsymbol{z}^{\mp} \cdot \nabla)\boldsymbol{z}^{\pm} = -\frac{1}{\rho}\nabla\left(P + \frac{B^2}{8\pi}\right) \tag{1.37}$$

and $\nabla \cdot \boldsymbol{z}^{\pm} = 0$ complete the set of equations.

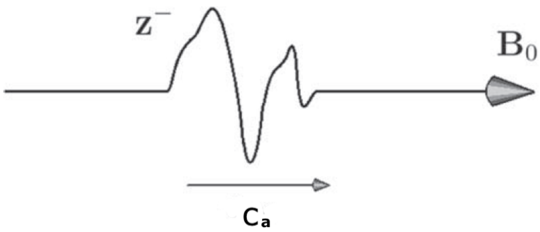

Figure 1.2: The $\boldsymbol{z}^{-}$ Elsässer's variable representing the Alfvén wave packet propagation parallel to the background magnetic field $\boldsymbol{B_0}$, with the Alvén speed $\boldsymbol{c_a}$. Picture taken from Magyar et al. (2019).

Now, by using the perturbation theory the dynamic equilibrium is easier to study. Thus, considering the velocity and magnetic field background, $\boldsymbol{U_0}$ and $\boldsymbol{B_0}$ respectively, the Elsässer's variables can be written, as $\boldsymbol{z}^{\pm} = \boldsymbol{z_0^{\pm}} + \boldsymbol{z'}^{\pm}$. Therefore

$$\boldsymbol{z}^{\pm} = \boldsymbol{U_0} \pm \boldsymbol{c_a} + \left(\boldsymbol{U_1} \pm \frac{\boldsymbol{B_1}}{\sqrt{4\pi\rho}}\right)$$

where $\boldsymbol{c_a} = \boldsymbol{B_0}/\sqrt{4\pi\rho}$ is the equilibrium Alfvén speed. Taking into account only the perturbed Elsässer's variables $\boldsymbol{z'}^{\pm}$, the equations (1.29), (1.30), (1.31), (1.32) and (1.1d) can be written as

$$\frac{\partial \boldsymbol{z}^{\pm}}{\partial t} \mp (\boldsymbol{c_a} \cdot \nabla)\boldsymbol{z}^{\pm} + (\boldsymbol{z}^{\mp} \cdot \nabla)\boldsymbol{z}^{\pm} = -\frac{1}{\rho}\nabla\left(P + \frac{B^2}{8\pi}\right) \tag{1.38}$$

where $\nabla \cdot \boldsymbol{z}^{\pm} = 0$ complete the set of equations, noting that the prime has been dropped from them. For the sake of clarity, the system has not been linearized until now, hence there are no restrictions on the perturbations amplitude. When one of the two Elsässer's variables vanishes, the pressure gradient undoes, so it is possible to write two uncoupled relations

$$\begin{cases} \dfrac{\partial \boldsymbol{z}^+}{\partial t} + (\boldsymbol{c_a} \cdot \nabla)\boldsymbol{z}^+ = 0, \quad \boldsymbol{z}^- = 0 \\ \dfrac{\partial \boldsymbol{z}^-}{\partial t} + (\boldsymbol{c_a} \cdot \nabla)\boldsymbol{z}^- = 0, \quad \boldsymbol{z}^+ = 0 \end{cases} \tag{1.39}$$

which have two exact solutions: $\boldsymbol{z}^+(\boldsymbol{x}+\boldsymbol{c_a}t)$ and $\boldsymbol{z}^-(\boldsymbol{x}-\boldsymbol{c_a}t)$. These solutions describe the arbitrary nonlinear pure Alfvén wave packages propagating $\boldsymbol{B_0}$-wise and $\boldsymbol{B_0}$-counterwise, respectively (as shown in figure 1.2). The Alfén waves are due to the magnetic tension and in the incompressible limit they are transversal waves. Moreover, the energy content is equally partitioned between the kinetic and magnetic forms.

The Alfvén velocity $\boldsymbol{c_a}$ assumes a physical meaning: it is the velocity with which Alfvén waves propagate into the plasma, neglecting the dissipative coefficients and the external forces. It is worthwhile to know that the equation (1.38) has the same structure as the Navier-Stokes equation. The difference consists in the non-linear coupling happens only among opposite wave directions, which leads to an intrinsically anisotropic behaviour.

Chapter 2

The birth of the solar wind

The solar wind is a stream of plasma released from the upper atmosphere of the Sun, called the corona. The solar wind is affected by eruptions and coronal mass ejections (CMEs). So, it is important to understand how the Sun is formed and how it affects the solar wind.
The aim of this chapter is to provide the main features of the Sun and to understand what kind of impact it has on the heliospheric structure.

2.1 The Sun

The nearest star to the Earth is the Sun. It is a spherical hot plasma kept together by its own gravity and it gets energy from the plasma's internal fusion reactions.

The Sun is formed by a gaseous core with temperature about $T_c = 1.5 \times 10^7$ K, which means that it is completely ionized. In this area most of the energy is produced and the 99% of the total comes from the pp-cycle. This type of process generates energy from mass conversion, due to the famous Einstein's formula $E = mc^2$. Part of this energy is converted into particles kinetic energy and the other one into radiative energy through emission of γ-photon rays.

The energy transfer is made up of the radiative and convective terms. The former is the result of many Compton scattering, which can be seen as photons absorbed by particles and re-emitted at different frequencies and directions. The latter takes form through the gradients of temperature and density inside the plasma, which become instable due to perturbations. Via the Schwarzschild criteria one can evaluate which contribution dominates.

$$\left|\frac{dT}{dr}\right|_{ad} < \left|\frac{dT}{dr}\right|_{rad} \rightarrow \text{convective terms dominate}$$
$$\left|\frac{dT}{dr}\right|_{ad} > \left|\frac{dT}{dr}\right|_{rad} \rightarrow \text{radiative terms dominate}$$

One of the most interesting things to understand is how magnetic field is generated by an electrically conductive fluid. The answer was proposed by Joseph Larmor (1919), who introduced the solar dynamo.

The inductive equation (1.32) can be written in two limit realms:

- the *perfectly conducting limit*, where $\sigma \rightarrow \infty$, hence

$$\frac{\partial \boldsymbol{B}}{\partial t} = \nabla \times (\boldsymbol{U} \times \boldsymbol{B})$$

looks like the Crocco's formula for an incompressible and non viscous fluid. Due to the hydrodynamic similarity, a plasma, with zero magnetic diffusion and initial magnetic field, cannot generate magnetic field ($\partial \boldsymbol{B}/\partial t = 0$). Therefore the Sun must have a primitive magnetic field;

- the *diffusive limit*, where $\sigma \to 0$, hence

$$\frac{\partial \boldsymbol{B}}{\partial t} = \eta \nabla^2 \boldsymbol{B}$$

in the presence of an electrically conductive fluid, the magnetic field spreads.

2.1.1 Dynamo principle

The perfectly conducting limit is always valid in the Sun, excepted for the magnetic reconnection zones. So, the Alfvén's theorem is valid in most cases and it explains how magnetic fields can be amplified.

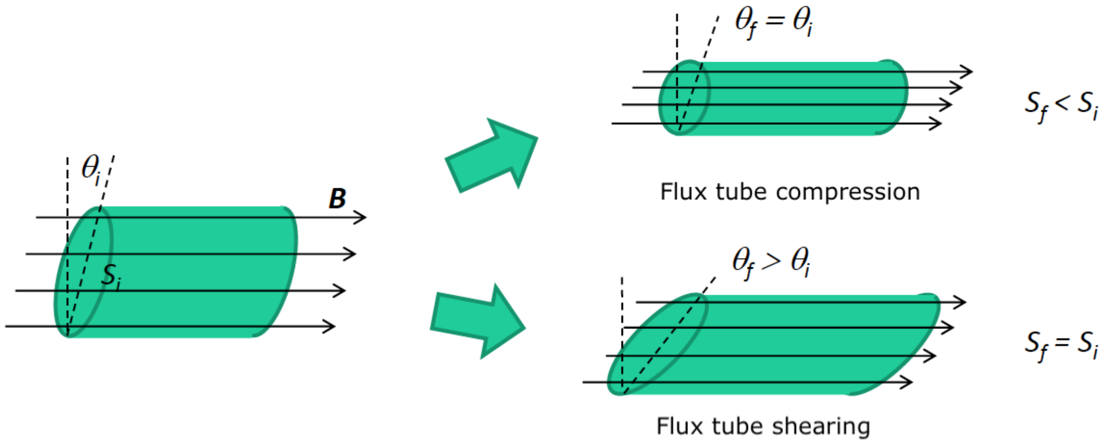

Figure 2.1: In the first case, the flux tube is compressed and the final section area is smaller than the initial one. In the second case, the sectional area does not change, but the flux tube is sheared and the section area axis is tilted. (Bemporad 2019)

As shown in figure 2.1, it can happen in two ways: by compression or shearing phenomena. Considering the Alfvén's theorem

$$BS\cos\theta = \text{const.}$$

where B can only vary if the angle θ or the section area S change.
The Sun rotation is not uniform, namely the angular speed changes with the latitude, thereby the magnetic shearing occurs and the magnetic field is amplified.

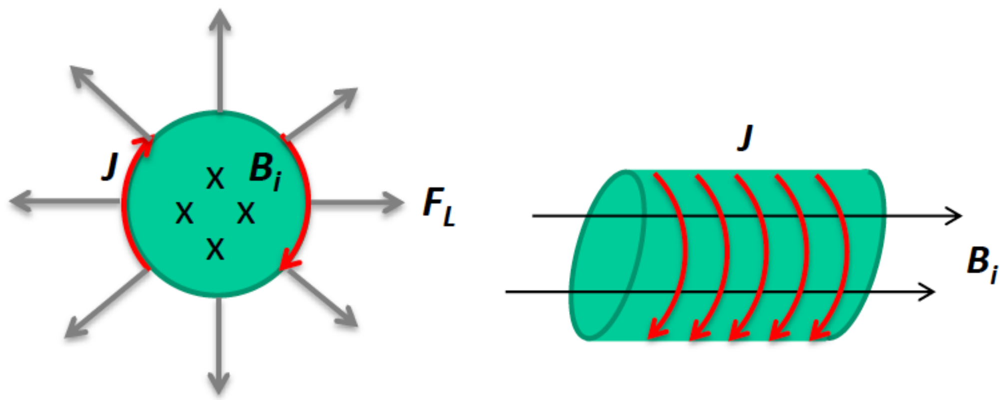

Figure 2.2: The flux tube expands due to the Lorentz's force (grey arrows) caused by current sheet. J is the current density and B_i is the magnetic field. (Bemporad 2019)

As explained before, the Sun is liable to the *amplification* phenomenon, on the other hand there is also the *transport* phenomenon. This one is made up of the magnetic buoyancy, which can be seen as a magnetic field constant within a radius R and linearly decreasing up to zero, generating a current sheet (CS) which produces a Lorentz force directed externally, as shown in figure 2.2. So, if the flux tube expands, its density decreases and climbs toward the external convective zone.

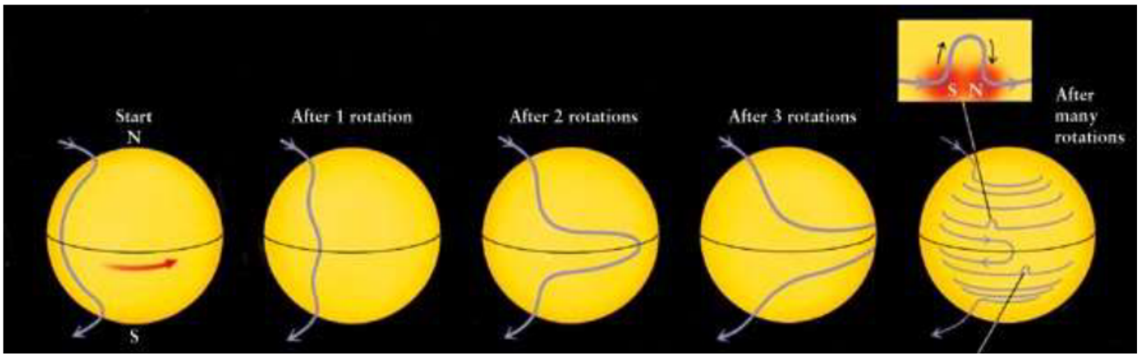

Figure 2.3: Amplification phenomenon due to shearing after some Sun revolution. (Bemporad 2019)

The *dynamo principle* comes from merging the inductive equation (1.32) with the Alfvén's theorem (amplification property) and the magnetic buoyancy. The plasma motion, with velocity $\boldsymbol{v}$, through a magnetic field produces an electric field and for the Ohm's law induces a current $\boldsymbol{J} = \sigma(\boldsymbol{E} + \boldsymbol{v} \times \boldsymbol{B})$. This one for the Ampère's law (in the MHD approximation) generates a magnetic field, which in turn creates an electric field (for the Faraday's law). Therefore a Lorentz's force arises in opposition to the force that drives the motion. After this cycle, the amplification property sets in. Indeed the differential rotation and the turbulent flows stretch the tubes flux and the magnetic field results amplified. The magnetic pressure grows into the tube flux and it expands. Hence, for the magnetic buoyancy the tube flux climbs toward the photosphere.

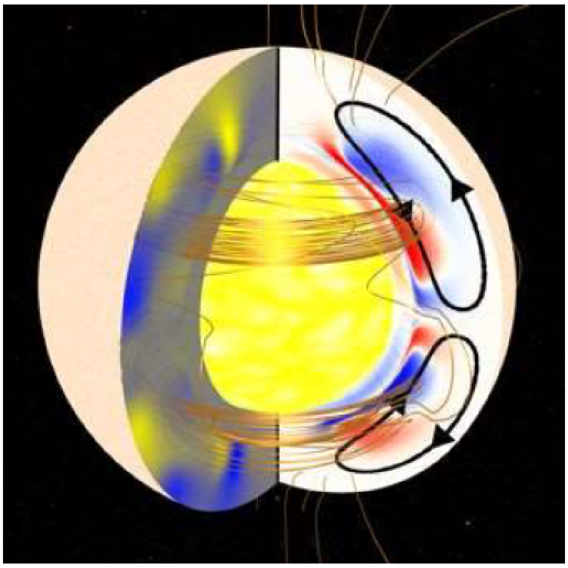

Figure 2.4: Convective cells are created due to the meridian motion. (Bemporad 2019)

The Sun rotates in the same direction as the Earth, but it cannot be studied as a rigid body. In fact, the angular speed of the Sun depends on the latitude, the radius [1] and the time. Moreover, there is a meridian motion which transports mass from the equator to the poles (on the surface) and an opposite motion below the Sun surface, as shown in figure 2.4.

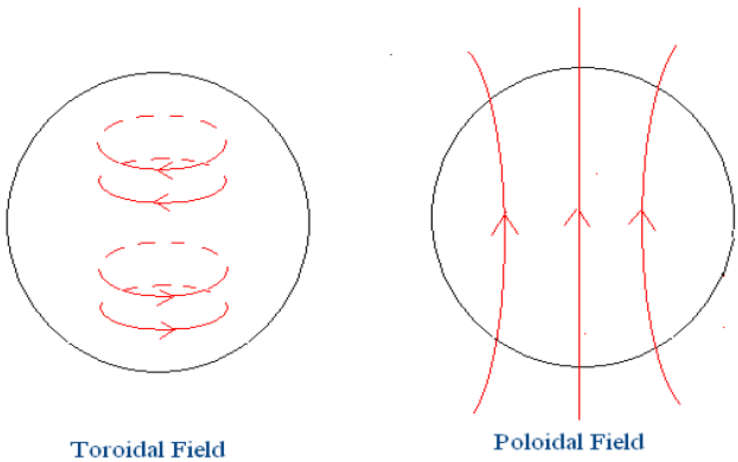

Figure 2.5: The Sun magnetic field is made up of the toroidal and the poloidal field. The farmer is the sum of the axial and radial speed components. The latter is made only by the azimuthal component. (Bemporad 2019)

The Sun magnetic field is not a steady state and it is split into two components, the *poloidal*

[1]The inner zones of the Sun (core and radiative zones, $r < 0.7R_{Sun}$) behave as a rigid body, with angular speed $\Omega_{poles} < \Omega < \Omega_{equator}$

and the *toroidal* field, as shown in figure 2.5. The latter is generated by the different angular speed, in particular the equator has a higher velocity than the poles and produces the toroidal field. The development process is also called ω-*effect*.

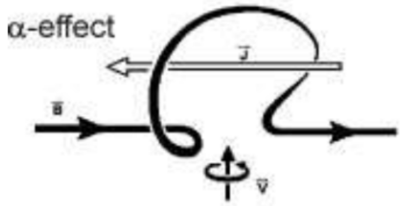

Figure 2.6: The tube flux is tilted due to the Coriolis' force. (Bemporad 2019)

Parker 1955 proposed the way to convert the toroidal field into the poloidal one. Considering a plasma volume in a convective cell, the volume expands when it raises and turns due to the Coriolis' force, this is called α-*effect*. If in the volume there are magnetic flux tubes, the magnetic field changes its features. As a consequence, the toroidal field is converted into the poloidal one and vice versa. This explanation leads to the result of skewness in the convective cell motions.

2.1.2 Sunspots and solar activity

As can be seen from the figure 2.7, the solar magnetic field periodically changes its polarity, then a *solar cycle* can be defined. This cycle lasts in time approximately 22 years and it ends when the polarity returns to the starting moment. Every 11 years, minimum and maximum solar activity alternate.

Throughout the maximum activity sunspots appear, which are marks on the photosphere caused by the α-effect. They are the visible part of the tubes flux that come out due to the instability.

The spots are presented as black holes in the photosphere due to the lower temperature ($\sim 3000 - 4500\,\mathrm{K}$) than the surrounding plasma ($\sim 5780\,\mathrm{K}$). Moreover, two areas can be distinguished: the inner and the outer ones. The former is called umbra and it is colder and darker and it has a magnetic field perpendicular to the Sun surface. The latter is called penumbra, it is lighter and its magnetic field is more inclined.

Typically, the sunspots appear in pairs with opposite polarity, which changes when the poloidal field reverses its direction. In the other hemisphere, the sunspot couple has reversed polarity.

The magnetic field of sunspots suppresses convection and prevents the surrounding plasma from sliding sideways into sunspot, hence the convection transport is blocked under the spot. Considering that the solar plasma is always characterized as high conductivity plasma, the Alfvén's theorem is valid everywhere, regardless of the β parameter. In other words, the plasma and magnetic field are frozen together. In the convective zone $\beta >> 1$, so the plasma controls the motion (thermal effects dominate). In the low corona $\beta << 1$, so the magnetic field controls the motion (magnetic effects dominate).

Watching the Sun magnetic field there are open and closed field zones, as shown in figure 2.9. The open field zones are characterised by weaker extreme ultraviolet (EUV) emissions and unipolar magnetic field regions. This results in less bright areas on the solar surface, as shown by the UV picture; indeed the plasma is much less dense and colder than the surrounding areas. The open field zones are less bright in the visible spectrum than in the closed zones and they are associated to the *fast solar wind*.
The closed field zones are also called active zones since they are high dynamic areas. In these

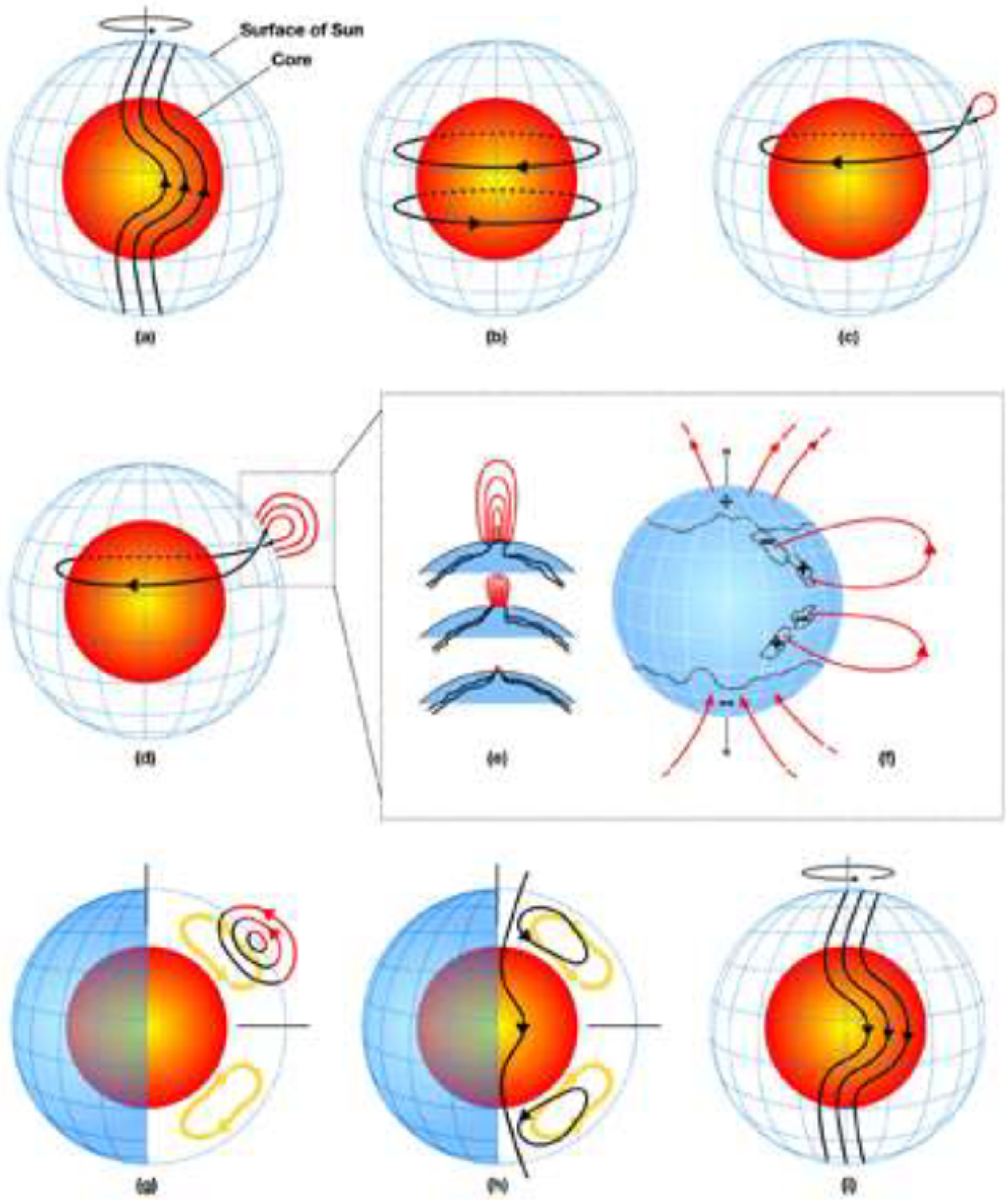

Figure 2.7: The red sphere is the radiative core which moves as a rigid body. The blue mesh is the convective zone, where there are different speeds. Beyond the changing field, it is clear how sunspot is born. (Bemporad 2019)

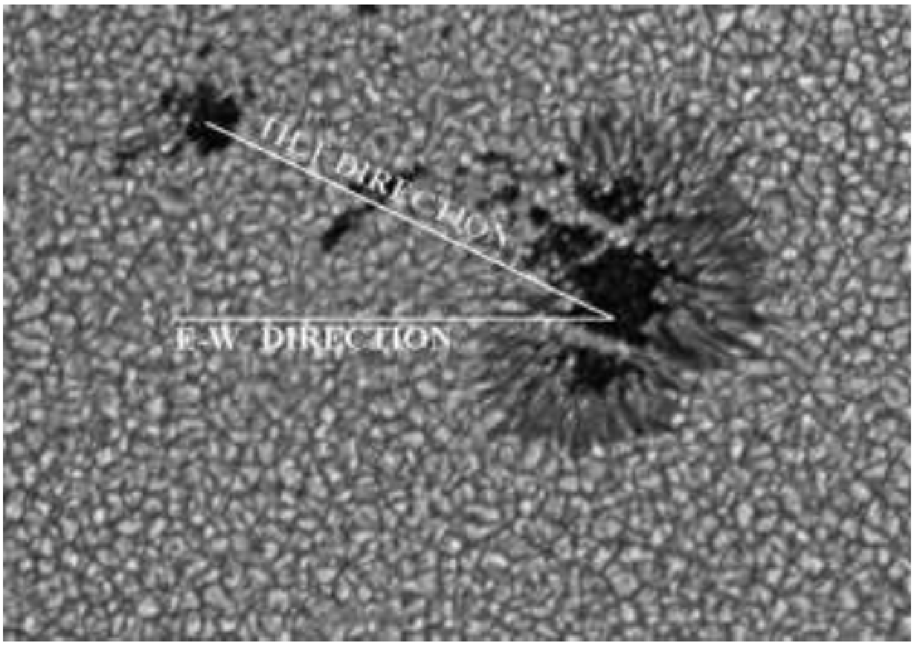

Figure 2.8: The sunspots appear in pairs, tilted 10° from the East-West direction. Two zones are visible, the inner one is the coldest and the outer presents a sloped magnetic field. (Bemporad 2019)

regions, the plasma is denser and hotter than the surrounding areas, therefore it results to be brighter than coronal holes in the EUV spectrum. In the visible spectrum, the active zones are brighter and are associated to the coronal streamers and to the *slow solar wind*.

2.2 Magnetic reconnection

Until now, the Faraday's equation has been considered as valid in the perfectly conducting limit, consequently the flow was assumed frozen with respect to the magnetic field. Analysing the complete inductive equation, there are two main components: the convective and the diffusive term. As explained before, each term works on different time scales and the relative importance is taken into account by the magnetic Reynolds number (or Lundquist number). If there were only the diffusive effects to dissipate the magnetic field, the diffusive scale would be the effective time scale of the magnetic field life. Considering the sunspots diffusive scale $\tau_d = 10^{14}$ s, the sunspots (or more in general the starspots) would live for millions of years, but this is not true. In addition to this, through observations of flares, coronal mass ejections (CMEs), and solar EUV pictures, it is clear that there are some other mechanisms which transform the magnetic topology.

The Lunquist number is evaluated over the global length scale, so the importance of the *local* phenomena is lost. This means that locally the resistive term can be different from zero. Moreover, the convective term has a vector nature, then in some regions the convective term vanishes, namely when $\boldsymbol{U}$ is parallel to $\boldsymbol{B}$. In these regions the length scale must be smaller than the global one, ergo the Lundquist number is smaller and the Alfvén's theorem is no longer valid, as well as the frozen condition. Thus, the magnetic field can change its topology and can reach minimum energy levels, which could not be achieved before in an ideal MHD regime.

Supposing to have two parallel flow tubes, with opposite polarity and separated by the so called *neutral layer*, the Lorentz force works perpendicularly to the field lines and pushes them towards

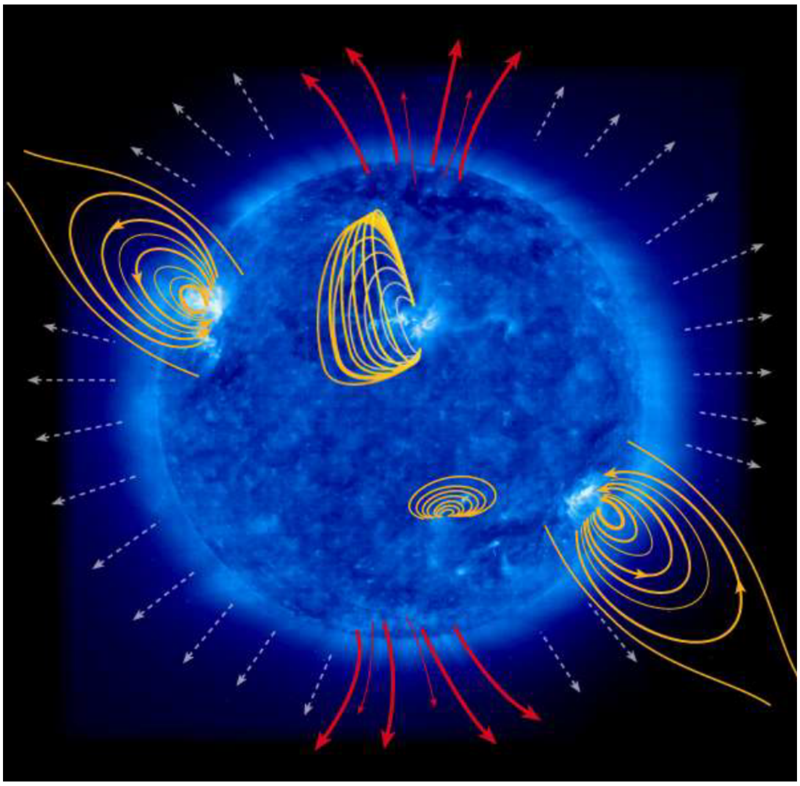

Figure 2.9: The solar UV picture shows the active zones and the coronal holes. Open and closed fields are drawn overlapping the UV images. The yellow arrows define the coronal loops, while the red arrows define the unipolar regions. (Bemporad 2019)

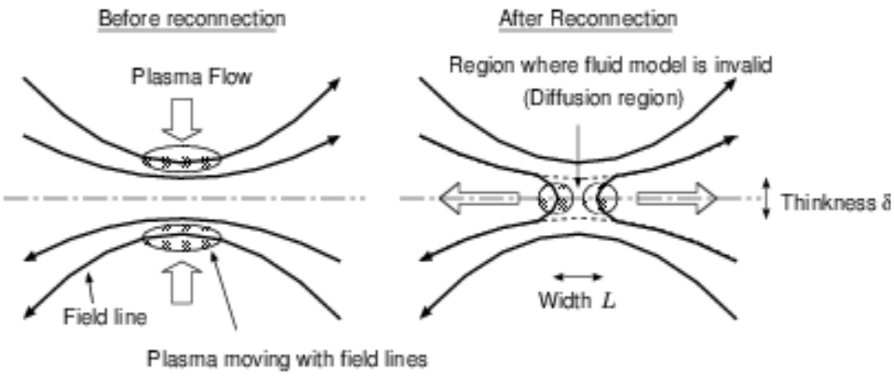

Figure 2.10: The dash-dot line is the neutral layer. On the left there is the separate tubes flow with opposite polarity. On the right the reconnection occurs, the diffusion region has thickness δ and length L. The arrows indicate the plasma flow directions. (Numata 2018)

the neutral layer. Since the magnetic field is frozen-in the plasma, it is compressed in a small region in which the diffusive limit is valid, as shown in figure 2.10. A current sheet appears due to the polarity change of $\boldsymbol{B}$, in which the plasma is pushed back by the magnetic pressure as long as field lines do not break, when it happens they reconnect and the magnetic tension straightens them, like a rubber band. In this region, the magnetic energy is turned into thermal and kinetic energies, the plasma pressure decreases and further plasma flow will be induced to carry another field line. This process is called *magnetic reconnection* and it can be driven or natural.

2.2.1 Driven reconnection

When the reconnection happens because of pressure force, it is defined as driven. It is worth knowing that the magnetic field can be destroyed, but the matter must find a way to run away from the resistivity region.

Different theoretical models were developed in the past, e.g. the Sweet and Parker model, or the Petschek model.

Sweet and Parker model

Historically, the first model presented was the Sweet and Parker model, which schematically describes a *steady state* reconnection without the analytic knowledge of $\boldsymbol{B}$ and $\boldsymbol{v}$ (where bmv is the flow speed).

Assuming a 2D geometry, $\boldsymbol{B} = (B_i, B_o, 0)$, $\boldsymbol{v} = (v_i, v_o, 0)$, $\boldsymbol{E} = (0, 0, E_z)$ (where i=inflow and o=outflow) a steady state condition and an incompressible flow, the dynamic equation is

$$\boldsymbol{E} + \frac{1}{c}\boldsymbol{v} \times \boldsymbol{B} = \frac{1}{\sigma}\boldsymbol{J} = \frac{\eta}{c}\nabla \times \boldsymbol{B}, \tag{2.1}$$

with $\nabla \cdot \boldsymbol{B} = 0$ and $\nabla \cdot \boldsymbol{v} = 0$.

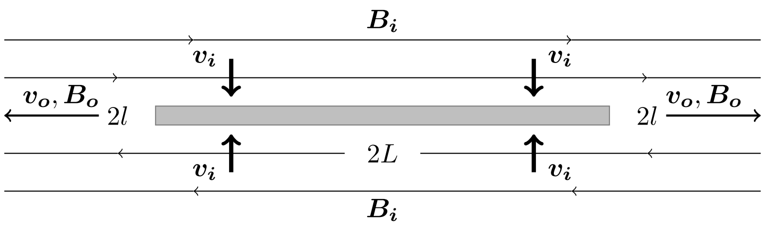

Figure 2.11: The current sheet (the grey rectangle) divides the upper and the lower magnetic field, which have different polarity. The vectors $\boldsymbol{v_i}$ indicate the plasma inflows, indeed $\boldsymbol{v_o}$ the outflows. The thickness of the current sheet is $2l$ and it is thin with respect to the global length.

In the middle of the current sheet, the magnetic field is zero, but outside the current sheet, the frozen condition is still valid, hence $\boldsymbol{B_i}$ is dragged into the resistive zone at v_i speed. The steady state condition imposes constraint on the value of the inflow speed v_i and on the current sheet thickness l, because the inflow speed is directly linked with the magnetic diffusivity η.

The problem is described by four equations and assuming to know η, there are six unknowns: v_i, B_i, v_o, B_o, L and l. It is necessary to impose two of this unknowns to solve the system of equations, so it is convenient to choose B_i and L. Evaluating the 2.1 at the current sheet boundary layer, where $\boldsymbol{J} = 0$, the electric field results to be

$$E = \frac{v_i}{c} B_i,$$

in the middle of the resistivity region $\boldsymbol{B} \simeq 0$, so

$$E = \frac{J_c}{\sigma},$$

the subscript c indicates the centre of the region. Considering the current density formula, the inflow speed is

$$v_i = \frac{\eta}{l}. \tag{2.2}$$

From the mass conservation law

$$l = L\frac{v_i}{v_o} \tag{2.3}$$

noting that $v_o > v_i$. From the magnetic flux conservation law

$$B_o = B_i\frac{v_i}{v_o} = B_i\frac{l}{L} \tag{2.4}$$

where $B_o < B_i$.
All of these equations are written depending on v_o, thus using the motion equation

$$\rho(\boldsymbol{v}\cdot\nabla)\boldsymbol{v} = -\nabla P + \frac{1}{4\pi}\boldsymbol{J}\times\boldsymbol{B} = -\nabla\left(P + \frac{B^2}{8\pi}\right) + (\boldsymbol{B}\cdot\nabla)\boldsymbol{B} \tag{2.5}$$

and doing a dimensional analysis

$$\rho\frac{v_o^2}{L} \simeq \frac{1}{4\pi}\frac{B_iB_o}{l}$$

from which the outflow speed is writable as

$$v_o = \frac{B_i}{\sqrt{4\pi\rho}} \equiv c_{ai} \tag{2.6}$$

where c_{ai} is the inflow Alfvén speed. Therefore the flow enters the resistive region with v_i and it is ejected with c_{ai}.

The adimensional rate is defined as

$$R_i = \frac{v_i}{c_{ai}} = \left(\frac{\eta}{Lc_{ai}}\right)^{1/2} = R_m^{-1/2} \tag{2.7}$$

and it depends only on the inflow parameters.

This model is simple and can explain very well what happens when two plasma flows, with opposite polarity, interact, but considering the typical values measured during the solar flares, the R_i results to be:

$$R_i = 3.16\times10^{-7}$$

hence the time scale results $\tau_{rec}\sim 10^7$ s, but from the observations it is known that $\tau_{flares} = 10^2$ s.

In this dissertation, the pressure term was neglected because it was imposed that $\nabla P = 0$. Considering the presence of this term, the reconnection rate is

$$R_i = \frac{c_{ai}}{v_o}R_m^{-1/2}$$

where it still does not depend only on the inflow term. If $\Delta P = P_o - P_i > B_i^2/4\pi$, the reconnection rate would be larger than the previous case, thus the time scale decreases, but it is still high. Additionally, Sweet–Parker reconnection neglects three-dimensional effects, collisionless physics, time-dependent effects, viscosity and compressibility.

Petschek model

As explained before, high magnetic energy conversion is not allowed as a result of the low efficiency process, which is probably due to the imposed geometry. Moreover, the Sweet-Parker model studies the configuration near the resistive region, a small part in relation to the global dimension of the event (i.e. flares, CMEs, ...). This leads to the consideration that v_i and B_i depend on the global features of the system, thus a larger region must be considered and the new variables will have the subscript "e" (i.e. external). Now the problem is how to link the external variables with the inner ones.

From the magnetic flux conservation $v_i B_i = v_e B_e$, so

$$\frac{R_i}{R_e} = \frac{c_{ae}}{c_{ai}} \frac{v_i}{v_e} = \frac{B_e^2}{B_i^2}. \tag{2.8}$$

Using the 2.8, 2.7 and 2.3, the length scales are

$$\frac{L_i}{L_e} = \frac{1}{R_{me}} R_i^{-3/2} R_e^{-1/2} \tag{2.9}$$

and

$$\frac{l}{L_e} = \frac{1}{R_{me}} R_i^{-1/2} R_e^{-1/2} \tag{2.10}$$

the diffusion region is determined knowing B_e/B_i and using 2.8, 2.9 and 2.10.

This presence of four steady state slow MHD-shocks is the particular property of this kind of models. These shocks allow the plasma to increase the reconnection efficiency, because the energy conversion is done both in the front shock and in the current sheet.

The reconnection rate is

$$R_e \propto (\ln R_{me})^{-1} \tag{2.11}$$

varying with the natural logarithm of the Lundquist number. Therefore, if R_{me} changes the R_e does not change much due to the logarithm function.
In the Petschek model the reconnection rate is higher than the one in the Sweet-Parker model. The former model works well with an anomalous resistivity, which is probably originated by other effects. In fact until now, the resistivity has been considered as the only reason that could violate the frozen condition. Recalling the 1.25, the presence of the electronic pressure gradient and the Hall current can cause the anomalous resistivity.

2.2.2 Natural reconnection

Up to now, the magnetic field has been considered frozen-in the plasma and the plasma flow origin has been neglected. Moreover, the steady state has been assumed a priori.

There are some interesting cases in which the resistive region develops naturally, without the velocity field being imposed. This leads to talk about the *resistive instabilities*, which are important if the reconnection rate is bigger than the diffusive rate.

Nowadays, the most corroborated proposals are the micro-instabilities and the macro-instabilities. The former consists in the trend of the current sheets to unravel, thus the current filaments diffuse. This fact can happen because of local variation in density or in resistivity and brings about local structures, which have no effect on the global magnetic field. This kind of instabilities are called *gravitational mode* and *rippling mode* and produce turbulence.
The macro-instabilities are associated to the global structure of the magnetic field and the most important one is called *tearing mode*. It is distinguished from the high length wave $kL << 1$ and it develops as well as in the absence of the neutral line. Another feature of this kind of instability is the *fractal* current sheet due to the multiple tearing mode which produces the magnetic islands as shown in figure 2.13.

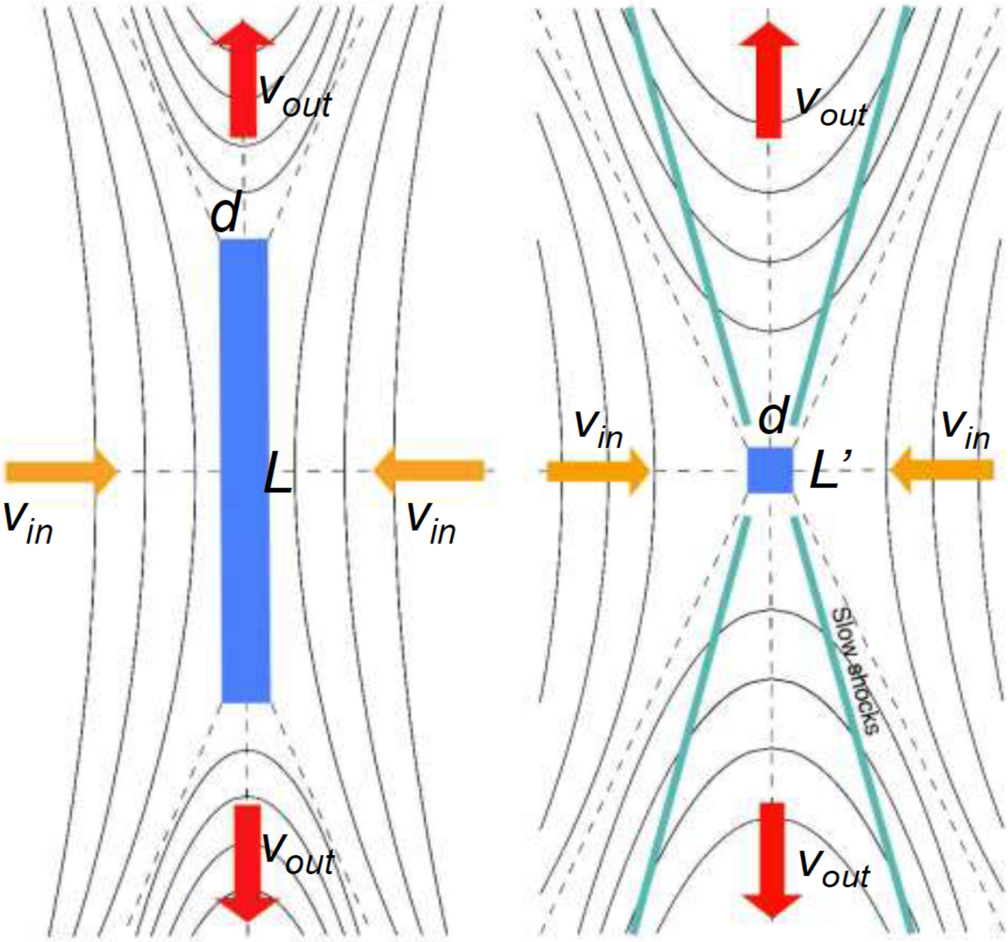

Figure 2.12: The blue rectangles represent the diffusive region. On the left, the Parker model, with the null point in the middle of the current sheet. On the right, the Petschek model, where the current sheet is smaller than the previous one. In the latter the slow MHD-shocks are present. (Bemporad 2019)

2.3 The solar wind

Observing the comets and the angle between the gas tail and the dust tail, Biermann (1951) postulated the existence of the solar wind. He calculated the solar wind speed ($\sim 500\,\mathrm{km\,h^{-1}}$) as well.
In 1958, Parker theoretically demonstrated the presence of a steady particles flux from the Sun and the impossibility of a static corona.
The experimental data, provided by Lunnik-2/-3 (1960) and by Mariner-2 (1962), confirmed the Parker's theory.

The solar wind is made up of protons p^+, electrons e^-, α-particles and heavy ions, with higher presence of protons and electrons. The intensity of these emissions change during the solar cycle, because of the presence of sunspots throughout the solar maximum.

During the solar minimum, the flow speed can be different if the particles considered come from

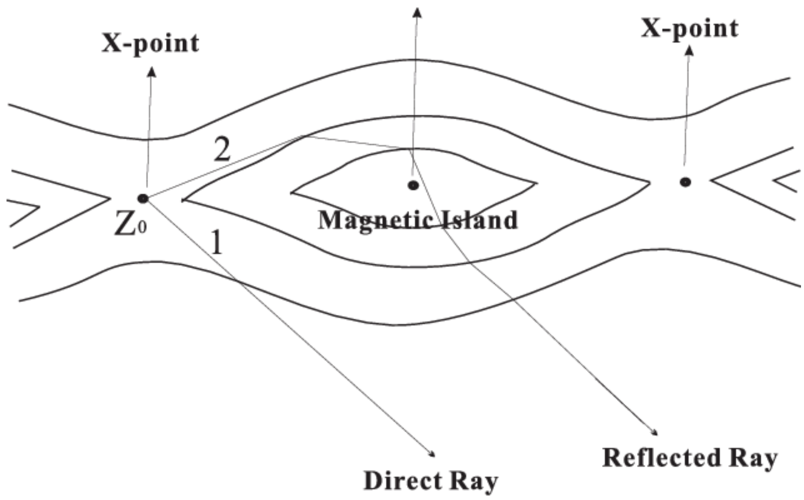

Figure 2.13: This is the final configuration if the reconnection happens more times. Two topologies are distinguishable, the closed force lines (magnetic islands) and the open force line. The neutral line disappears and it transforms in a discrete distribution of point called O-type or X-point. The farmer when the point is in the magnetic islands. The farmer when two open lines cross each other. (Tan 2009)

the coronal hole regions (low activity regions) or from the coronal loops (high activity regions). From the open regions, the solar wind velocity reaches $\sim 750\,\mathrm{km\,s^{-1}}$ and the flow is called *fast solar wind*. From the closed regions, the flow velocity is around $\sim 400\,\mathrm{km\,s^{-1}}$ and it takes the name of *slow solar wind*.
Meanwhile in the solar maximum, the high presence of sunspots increases the solar emissions over the whole solar surface. Thus, the two different regimes are not distinguishable.

These two kinds of flow are associated to different sources, the fast wind from the cold sources and the slow solar wind from the hot ones. Therefore, the physical processes ahead the flows are different.

The Parker's theory

The solar wind model has been developed by Parker (1958) on the basis of one-fluid and one dimensional continuity, momentum and energy hydrodynamic equations. Assuming a spherical symmetry, isotherm and a not static corona, the dynamic equation gets

$$\rho\frac{DU}{Dt} = -\nabla P + F \tag{2.12}$$

where D/Dt is the material derivate. Supposing a steady-state $d/dt = 0$ and the only one external force is the gravitational force, the equation becomes

$$U\frac{dU}{dr} = -\frac{1}{\rho}\nabla P - \frac{GM_{Sun}}{r^2}$$

specifying with G the gravitational constant, M_{Sun} the solar mass and r is the heliocentric distance. Considering the solar wind composts only of protons and electrons, the pressure can be written as

$$P = \rho k_b T/\mu m_H,$$

where m_H is the mass of the singular solar wind proton ($m_p \simeq m_H$). So the 2.3 assumes the form

$$U\frac{dU}{dr} = -\frac{1}{\rho}\frac{k_B T}{\mu m_H}\frac{d\rho}{dr} - \frac{GM_{Sun}}{r^2},$$

after some manipulations and scribing $v_c^2 = k_B T/\mu m_h$ and $R_c = \mu m_H G M_{Sun}/2k_B T$, the dynamic equation becomes

$$\left(U - \frac{v_c^2}{U}\right)\frac{dU}{dr} = 2v_c^2\left(\frac{1}{r} - \frac{R_c}{r^2}\right) \tag{2.13}$$

known as *Parker's equation*.
To complete the system of equations, one has to write

$$\rho U r^2 = const. \tag{2.14}$$

$$\frac{d}{dr}\left(\frac{P}{\rho^n}\right) = 0 \tag{2.15}$$

the continuity 2.14 and the energy 2.15 equations.

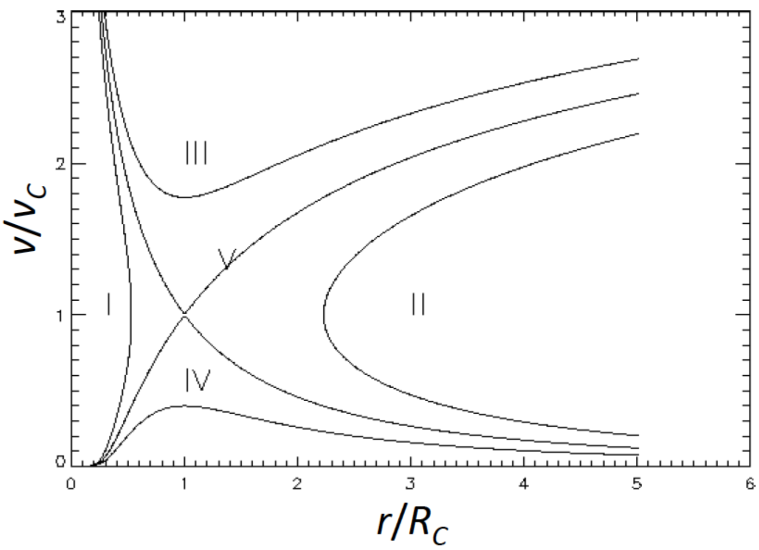

Figure 2.14: Integral curves of equation 2.13, where the Sun is in the origin of the coordinate system.

The Parker's equation 2.13 can be solved through the separation of variables method (or Fourier method) and different solutions can be found as in figure 2.14.
The first and the second curves show double solutions for a single value of r/R_c, moreover the second curve has no solution at the Sun surface $r/R_c = 0$.
The third curve has higher values than the experimental data.
The solutions of the fourth curve are called solar breeze due to the high density and pressure values (unrealistic).
The fifth curve represent the solutions for the solar wind as detected by in-situ measures.

It is worth knowing that when $U/v_c = 1$ (in figure $v/v_c = 1$) and $r/R_c = 1$, the solar wind velocity is $U = a$, i.e. the sound speed of a isothermal gas. The point (R_c, a) is the *saddle point*. The wind is *subsonic* when $r < R_c$ and *supersonic* when $r > R_c \sim 5.7R_{Sun}$.

Parker's method demonstrates the solar wind existence, which expands through the heliosphere thanks to the opposition of thermal pressure and the gravitational force. Parker did not consider the magnetic field, so he only used the hydrodynamic equations. The presence of the gravitational force allows the wind to transition, in fact in case of absence of this force, the whole field motion is either subsonic or supersonic.

Solar wind features

By in-situ measures, protons p^+ and electrons e^- shown temperature anisotropies: $T_{p\perp} > T_{p\parallel}$ in the fast solar wind and vice versa in the slow wind.

Table 2.1: Features of slow and fast solar wind.

	Slow wind	Fast wind
Speed [km s^{-1}]	400	750
Number density [cm^{-3}]	10	3
Flux [cm^{-2}s^{-1}]	3×10^8	2×10^8
Magnetic field [nT]	3	3
Proton temperature[K]	4×10^4	2×10^5
Electron temperature [K]	1.3×10^5	1×10^5
Composition (He/H)	1-30%	5%

The solar wind can be split into fast and slow and its features at 1 au (au is the distance between the Sun and the Earth) are summarized in the table 2.1. It is to be noted that the electrons temperature, in the solw wind, is higher both than in the fast wind and than proton temperature in slow wind. As the number density as the flux are higher in the slow wind. The magnetic field is the same in both cases.

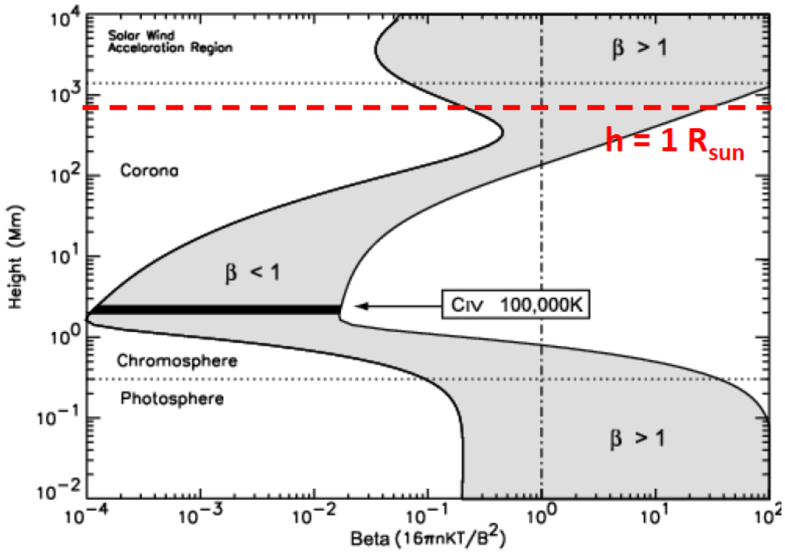

Figure 2.15: Variation of β from the photosphere to the solar wind. (Bemporad 2019)

The coronal plasma is highly conductive, so the Alfv'en theorem is valid and the magnetic field diffuse more than the plasma $\beta > 1$. When $\beta > 1$ the flow accelerates, indeed when $\beta < 1$ the flow decelerates as in figure 2.15

Chapter 3

The heliosphere structure

The Sun and the Local InterStellar Medium (LISM) are not dynamically coherent cosmic structures, so the heliosphere framework roughly depends on their interaction. More kinds of field can be found inside the heliosphere and all of them are the result of the Sun rotation and motion into the LISM. The real shape of the heliosphere is actually not understood in depth. It depends on the constrains and on the computational model selected.

In this chapter, the general features and structures of the heliosphere are described, starting from near the Sun and moving away to the LISM.

3.1 The Parker's spiral

Both the rotation of the Sun around its own axis and the magnetic field, which is carried by the wind and it is characterized by changing polarity, give rise to particular structures in the heliosphere.

In the light of that, a corotating reference system is the best choice to study the inner heliosphere. The Sun is at rest and the solar wind "gains" a longitudinal speed U_ϕ (v_ϕ in figure 3.1). Assuming that the flow radial speed is constant $U_r = const.$ (in figure 3.1 is v_r), in other words the region considered is where the wind is steady ($\beta > 1$).

At the generic latitude θ

$$U_\phi = \Omega(r - r_0)cos\theta \tag{3.1}$$

where Ω is the angular speed of the Sun at that specific latitude, r_0 is the Sun radius and r is the directrix. The two components, U_ϕ and U_r, give rise to the speed vector U, which is inclined of ψ with respect to the radial vector. So the ψ angle is

$$\psi = \arctan\frac{U_\phi}{U_r} = \arctan\frac{\Omega(r - r_0)cos\theta}{U_r}$$

when $r \to \infty$: $\psi \to \pi/2$.

It is worthwhile to notice that the spiral starts from the *source surface*, the layer where β go from less than 1 to larger than 1. Moreover, the Parker spiral pass through the whole heliosphere and its span depends on distance and what kind of solar wind there is (e.g. at Earth distance 1 au and with slow wind $400\,\mathrm{km\,s^{-1}}$, $\phi = 45°$).

Since the Alfvén theorem is still valid, the magnetic field and the wind speed are parallel. The wind blows from the Sun with a constant direction, but the magnetic field changes its own polarity. Therefore, there is a current sheet which defines the polarity boundaries called *sector boundaries* (SC). Thus, the phenomenon where $B_\parallel$ changes direction is the *polarity switch*. The shape of the CS follows the Parker's spiral (figure 3.2) and it takes the name of *ballerina skirt*. Due to the

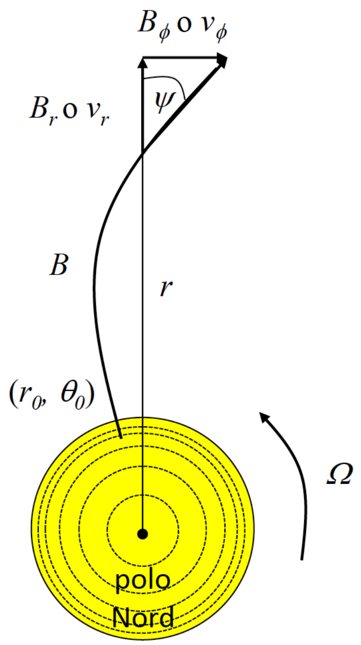

Figure 3.1: This view from above of the Sun shows the solar angular speed Ω, the solar radius r_0 and the distance from the solar center r. The component B_ϕ grows up and the Parker's spiral is born. (Bemporad 2019)

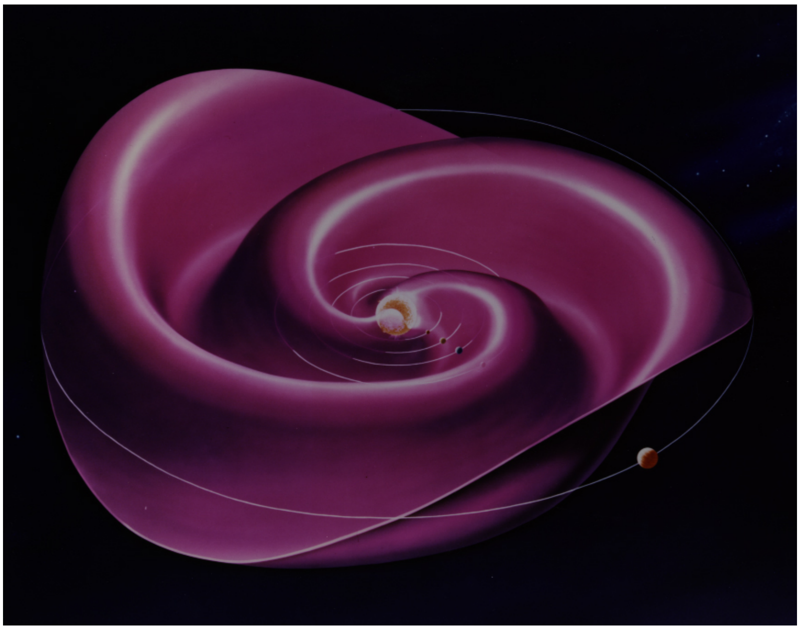

Figure 3.2: The Sun is in the center and the purple spiral is the current sheet with the particular shape called ballerina skirt. (Zell 2013)

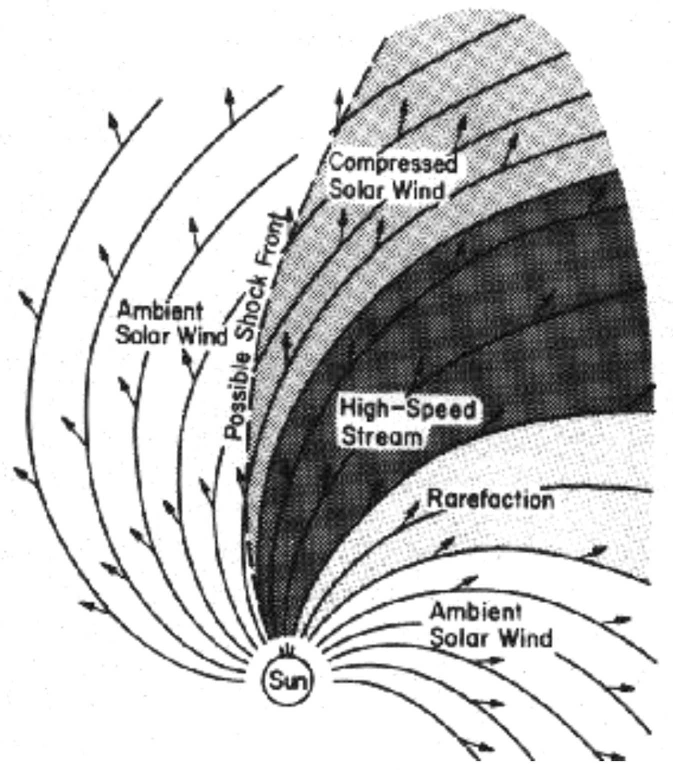

Figure 3.3: When there is a high speed stream, the spiral is getting larger. Thus, there is a rarefaction zone (expansion of the plasma) and a compressed zone. In this last region, a shock can occur. (Bemporad 2019)

dependence on the latitude, the CS is sloped compared to the ecliptic plane, so the CS produces a magnetic field component B_z perpendicular to the ecliptic.

A particular phenomenon of the Parker model is the formation of corotating interaction regions (CIR). These zones are produced due to the different wind speed, which means that ψ assumes several values. This leads to the definition of compression and expansion zones, as reported in figure 3.3.

3.2 The termination shock

Disregarding what type of SW is taken into account (fast or slow), the plasma expands radially from the Sun with a supersonic speed. This means that the flow cannot decelerate in absence of a shock. This one is called the termination shock (TS) and it was theoretically predicted before the Voyagers 1 (V1) passes through it. The TS separates the inner heliosphere from the so called heliosheath (HS), which is the region where the SW is subsonic and interacts with the LISM.

In the absence of a solid surface, the SW and LISM pressures must be the same or a discontinuity originates and the pressure follows the Rankine-Hugoniot relations. Therefore, as Pogorelov et al. (2017b) said, the TS is responding to changes in the ratio between the SW and LISM ram pressures ($\rho U_R^2/\rho_\infty U_\infty^2$).

In the first attempts, the TS was predicted to be squashed and symmetric (with respect to the ecliptic) due to the fact that the analysis were done by using the bow shock relations, e.g. the stand-off distance

$$\Delta_{TS} = 1.1 R_{HP} \frac{N_1}{N_2}$$

where N_1 is the total solar wind density inside the heliosphere, and N_2 is the total plasma density outside the TS in the turbulent HS.

$\Delta_{TS} \sim 36\,\mathrm{au}$ and $R_{TS} \sim 94\,\mathrm{au}$ was computed from this equation (Balogh et al. 2013). The result was achieved without considering the charge exchange, which is a fundamental phenomenon in the heliosphere physics. In fact, the charge exchange involves a different momentum and energy transfer. It is worth highlighting the presence of anomalous cosmic rays (ACRs), galactic cosmic rays (GCRs) and termination shock protons (TSPs), where the latter are subsets of the pick-up ions (PUIs). PUIs are produced from the charge exchange between an ion and a neutral atom, while ACRs are assumed to be produced by interstellar neutral atoms that drift into the heliosphere and become singly ionized by charge exchange with a solar wind ion or by photoionization. The cause of ACRs acceleration is not yet understood, in fact Pogorelov et al. (2017b) endorses the theory where the first order Fermi acceleration in the TS is the main cause.

These particles must be considered in the motion equations and different sort of models have been proposed to implement them, as single-ion multi-fluid models (SI-MF), multi-ion multi-fluid models (MI-MF), single fluid model (SF) and many more. It is important to consider the PUIs because only they are the $20-30\%$ of the total particles in the SW. Moreover, PUIs' carry the majority of the thermal pressure upstream of the TS, with a temperature of $10^6\,\mathrm{K}$ compared to the thermal SW's temperature of $10^4\,\mathrm{K}$. It comes by itself that PUIs roughly influence the structure and dynamic of the TS.

With the Voyager probes (V1 and V2) data, it is possible to study the real heliosphere configuration and in this way computational models can be validated. V1 crossed the TS in 2004 at a helioradius and heliolatitude of 94 au and 34°N, while V2 first did so in 2007 at 84 au and 28°S. There is a difference of 10 au between the two distances. This can be explained considering that the magnetic field in the unperturbed LISM is directed to the southern hemisphere by 45°, then it is logical to think that the interstellar magnetic field (ISMF) tends to make the heliosphere asymmetric.

From the Ulysses data analysis, differences in the slow and fast SW ram pressure are discovered, for example during solar cycle 22, the slow SW ram pressure was ~ 0.8 of the fast one. The differences in the ram pressure values depend on the solar cycle and sometimes the slow wind could reach a higher value than the fast wind.

The charged particles are probably accelerated by the TS, in fact the V1 and V2 measured different value of particles speed downstream and upstream of the TS, as shown in figure 3.4.

The TS thickness is smaller than the PUI gyroradius at least of a factor of 10, therefore the shock can be considered as a discontinuity. In particular the TS is a *quasi-perpendicular shock* [1], which differs from the quasi-parallel one for the less turbulence produced.

3.3 The inner heliosheath

The heliosheath is the region between the helipause (HP) and the termination shock, where the HP is the surface that separates the LISM and the SW and it will be tackled in the next section. In

[1] The perpendicular shock is a discontinuity in the magnetic and motion field. The shock surface is parallel to the magnetic field lines, but moves perpendicularly to them. The magnetic field appears compressed downstream, so the magnetic field lines are closer than upstream, and plasma speed is reduced. The kinetic energy is converted into magnetic and thermal energy.

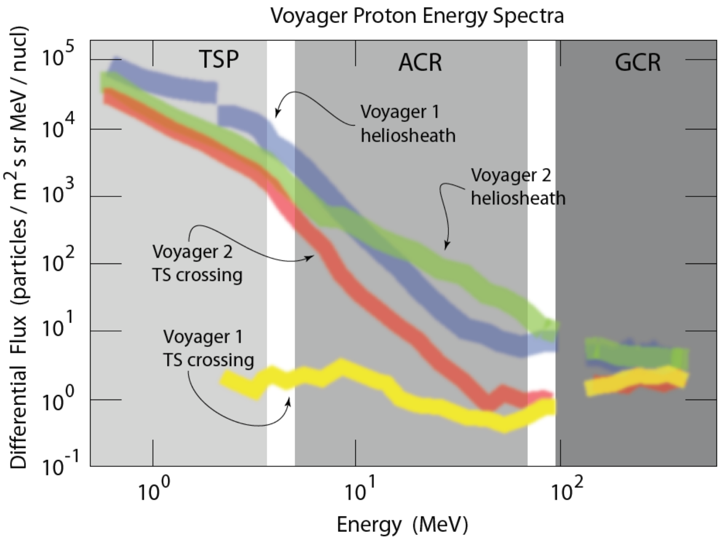

Figure 3.4: High energy proton spectra at TS and at HS. The width of line shows the measurement error. The TSP flux was $3-4$ times higher before crossing the TS. Moreover, TSPs have less energy than ACRs and GCRs. There are differences in the flux values among V1 and V2, this anisotropy could be due to the asimmetry of the heliosphere. (Balogh et al. 2013)

truth, the definition of HS is too general since the heliopshere structure is not well understood, so in literature the *inner* heliosheath (IHS) is the region between the HP and TS as well as the *outer* heliosheath (OSH) is the zone among the HP and the likely bow shock (BS).

3.3.1 Particles in the heliosheath

The plasma in the IHS is a mixture of SW and LISM, thus it is important to understand the formation processes of the particle populations. The charge exchange is a birth-death course, which happens in presence of a parent neutral atom and a parent ion with non-zero relative velocity. The parent particles disappear, a new neutral atom, with the properties of the parent ion, and a new ion, with the properties of the parent neutral atom, appear. The newly created ion is called *pickup ion* (PUI) and is subjected to the electric field, which accelerates it until its velocity is equal to the surrounding plasma. The newly born neutral atom follows a ballistic trajectory due to the fact that it is not affected by the electric field. They propagate far into the LISM and can experience a new charge exchange from which are created a new population of PUIs and a new population of neutral atom, also called *energetic neutral atoms* (ENAs). It is worthwhile noticing that the distribution function of the PUIs, in the beginning, is a ring-beam distribution. Thus, the distribution becomes a shell-distribution, in which some particles are at lower energies and other particles are at higher energies.

It comes by itself that PUIs are not in equilibrium with the SW and this is another reason to implement the PUI distribution in the mathematical methods and so in the computational models.

The charge exchange between H atoms and PUIs in the IHS results in a relevant momentum and energy removal from plasma to ENAs. This leads to a reduction of the IHS width, with the TS farther from the Sun.

3.3.2 Magnetic field

Thanks to the Voyager probes and their magnetic field instrument (MAG), it is possible to analyse the presence of the heliospheric magnetic field (HMF) turbulence at both small and kinetic scales.

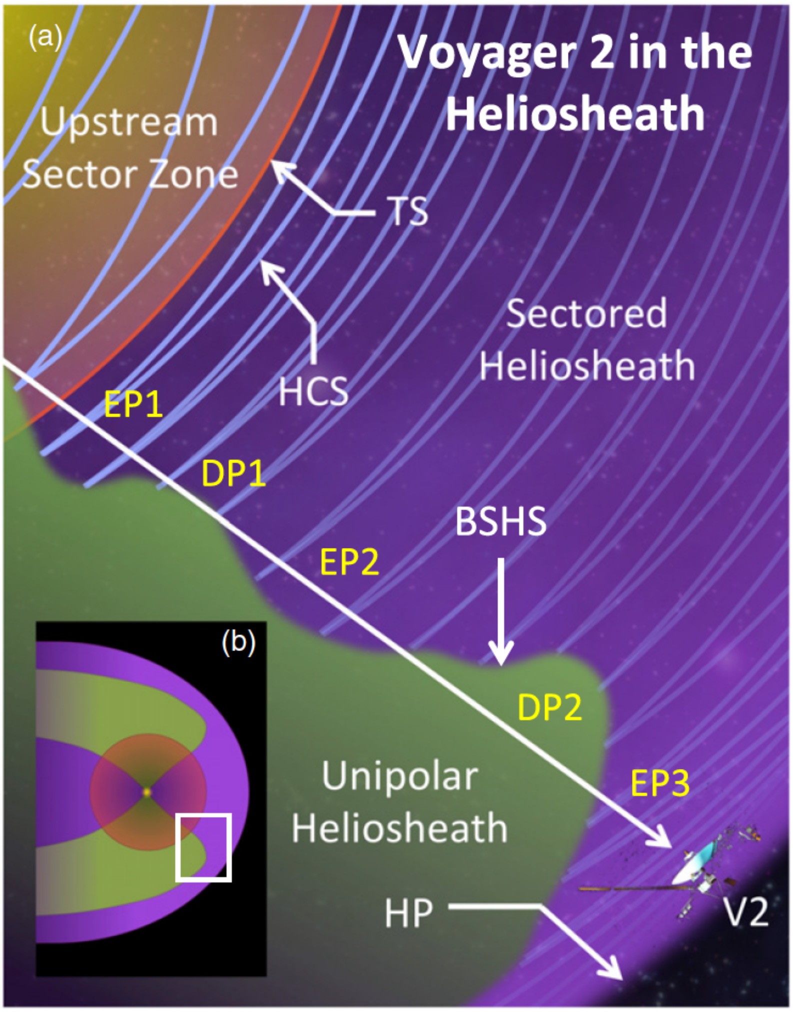

Figure 3.5: Depiction of the HMF in which the V2 trajectory is shown. In the lower left corner there is the global picture. In the green zone there is the unipolar field, while in the purple zone there is the sector region. In the SHS the HCS is shown. The red line is the TS. (Hill et al. 2014)

The HMF is generally separated into two regions: *unipolar* region (UHS) and *sector* region (SHS). The latter is the region where the solar magnetic field changes its polarity and, until now, it has been thought that SHS is only produced by the differential Sun rotation. The SHS is defined by the HCS, which depends on the solar activity. Indeed, the minimum latitudinal extent of the HCS from the solar equatorial plane occurred near solar minimum. As solar activity increases the latitudinal extent of the HCS increases (Burlaga et al. 2017).

The time dependent solar activity affects the sector zone amplitude but also the heliosphere length. In the latter case, one talks about *heliosphere breath* due to the continuous extension and contraction of the heliosphere boundaries. In the former case, the MAG reveals the multiple

V2 crossing of the UHS and SHS boundaries. Moreover, the increasing number of HMF vector reversals, crossing the TS, was revealed. This observation confirms that the TS is a perpendicular (or quasi-perpendicular) shock. In other words, the sectors number increase crossing the TS.

The radial velocity component, theoretically, must tend to zero near the HP. Approaching the HP, the V1 probe has shown negative velocity values; this can be explained considering the nature of the HCS, not only due to the tilt between the Sun's rotation and magnetic axis.

The sector widths are not as small as expected, this supports the thesis according to which the Sun's tilt is not the only cause for the sector boundaries. The HCS can also be created by stream interaction, reconnection and CME.

3.4 The heliopause

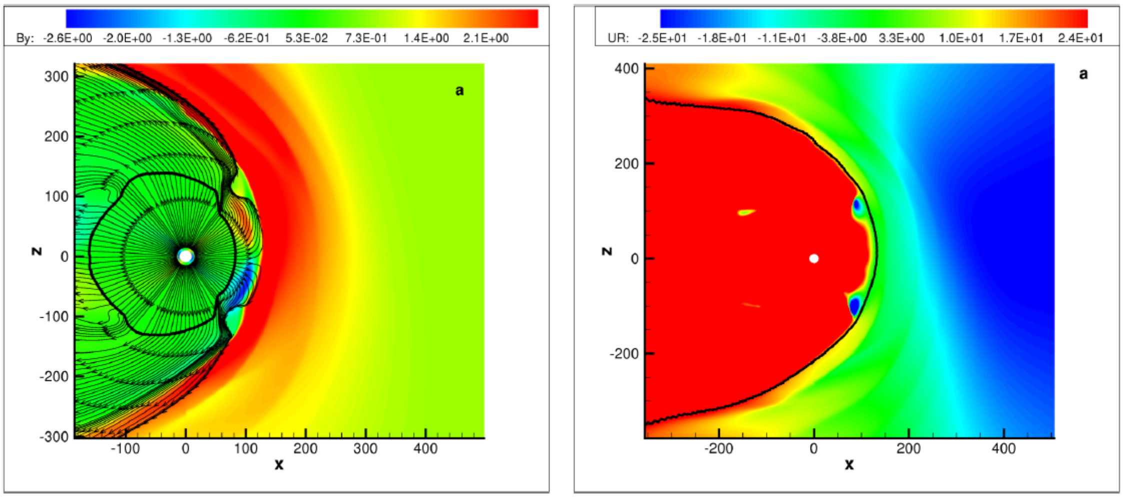

Figure 3.6: The presence of the HP forces the magnetic field to deflect parallel to the HP itself. On the left, the magnetic field lines, which start from 15 au (heliocentric distance). The TS is shown by a thick black line. On the right, the velocity field is shown, where in the IHS there are two bubbles with negative speed. Distances are given in AU. The y-axis is directed into the figure plane. (Pogorelov et al. 2017b)

Generally, two colliding fluids generate a discontinuity along their separation surface. Plasma is a particular kind of fluid, so between the heliosphere and the LISM there is a discontinuity surface. The initial problem is to understand what kind of discontinuity the HP is. In fact, unlike the neutral fluid, the plasma can produce shocks, contact and rotational (Alfvèn) discontinuities, rarefaction waves. The rotational discontinuity cannot exist because no density variation is permitted and a mass flux is needed to realize that. Moreover, the rotational discontinuity speed is the Alfvèn velocity and both the magnetic field and velocity rotate crossing the discontinuity. So, the HP is a contact discontinuity, which is characterized by different density values embracing the surface. This type of discontinuity is also called *tangential* because the magnetic component normal to the surface is zero. Thus, the magnetic field results to be parallel to the HP and for the Alfvèn theorem the speed is parallel to the HP too (as shown in figure 3.6). The total pressure is constant crossing the discontinuity. In figure 3.6, the two bubbles, in which negative radial velocity has been revealed by V1, is reproduced by computational model.

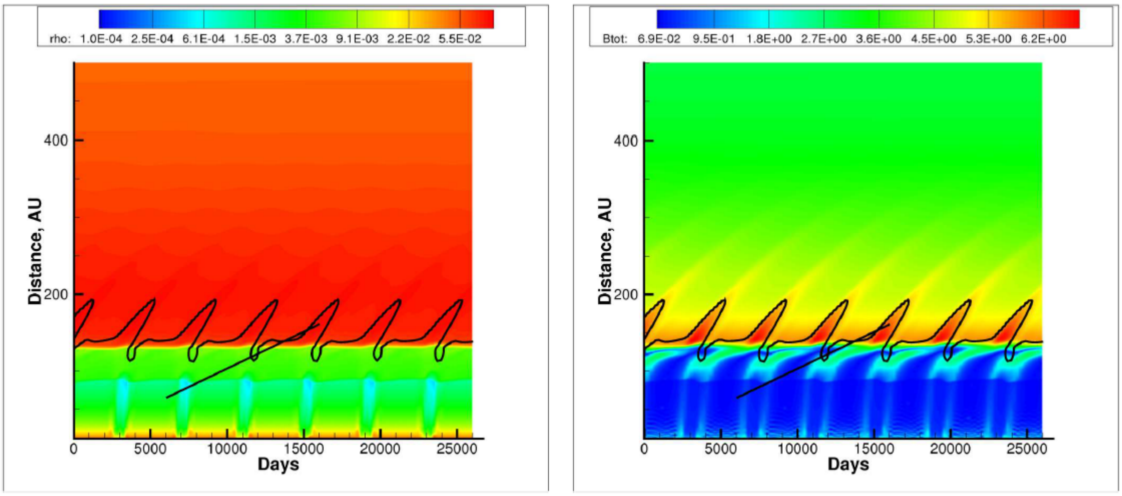

Figure 3.7: Space-time plots of (left) plasma number density and (right) magnetic field magnitude. The black curve represent the zero velocity line. Due to the instabilities, this line moves in time. (Pogorelov et al. 2017b)

Pogorelov et al. (2017b) explained that the HP is not a classical MHD discontinuity due to the charge exchange, which produces both Rayleigh-Taylor and Kelvin-Helmholtz instabilities. These instabilities develop more efficiently when the HMF decreases.

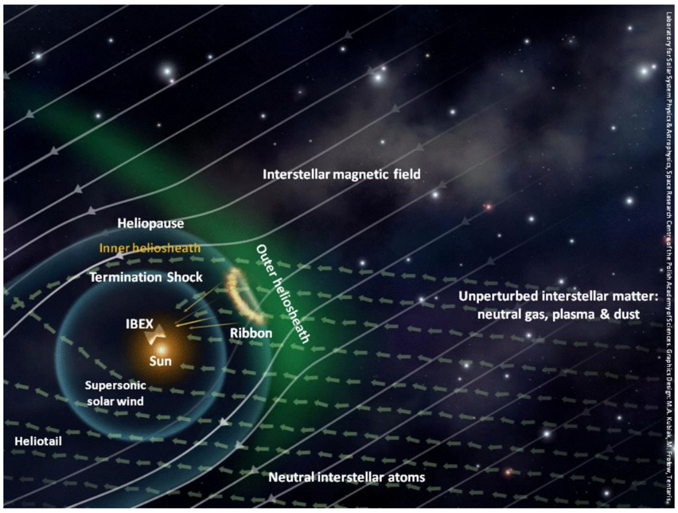

Figure 3.8: Artist's conception of the HP, with ENA ribbon measured by IBEX. The tilt between the magnetic and velocity field is shown. (Sims 2010)

The ISMF is not parallel to the LISM velocity, but is rotated by 45° as explained before. Moreover, the ISMF must be parallel to the HP, so a process of topological changes of the ISMF must occurs. The results is a rotation of the magnetic field, near the HP, from the $\boldsymbol{B}_\infty$ direction. This process is called *draping*.

The HP orientation, with respect to the ecliptic, depends on the pressure balance, which is

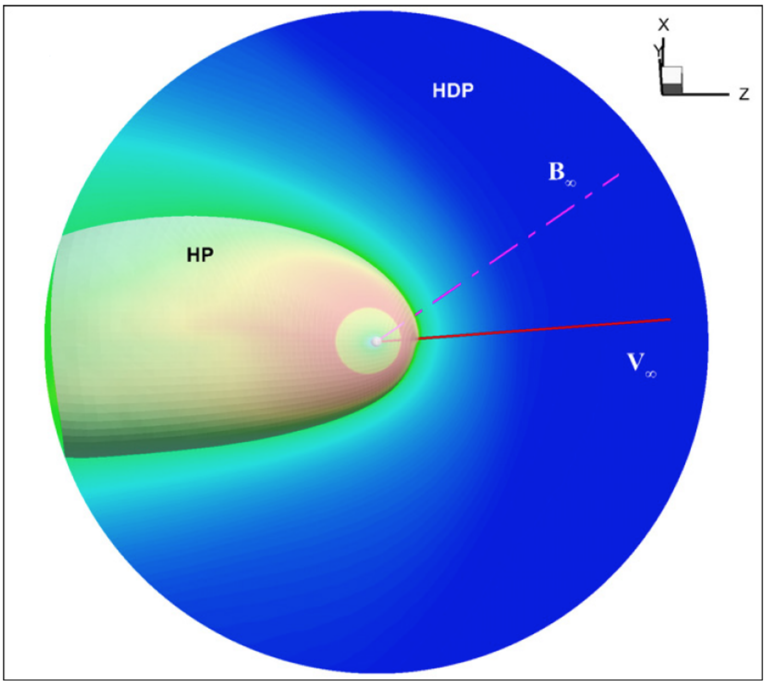

Figure 3.9: The heliosphere structure is partially represented. The $\boldsymbol{V}_{\infty}$ and the $\boldsymbol{B}_{\infty}$ direction is shown as well as the TS. (Pogorelov et al. 2011)

influenced by the PUI and ENA distribution. In particular, thanks to the Interstellar Boundary Explorer (IBEX) measurements is possible to study the ENA distribution without the in situ data. From IBEX data was discovered that the ENA intensities is not equally spread on the HP. The intensity distribution is similar to a *ribbon*. This is a troubling puzzle to solve because the origin of this particular atoms is not yet understood. It is a fact that the HP is not symmetric and Pogorelov et al. proposed an explanation for it. They supposed that the magnetic field rotates the HP clockwise, shifting the LISM stagnation point northward. Since in the stagnation point, the plasma number density increases, the charge exchange too. Therefore, the ion production is increased and this surplus of particles is decelerated from the HP. The result is a pressure increase in the north region of the HP, which rotates the HP counterclockwise. Summarizing, the ISMF tends to make asymmetric the HP, while the charge exchange symmetrizes it.

3.5 The heliotail

Differently from other stellar systems, for which one may have an external view, in the Sun system this is impossible. So, understanding the global structure of the heliosphere is an arduous challenge. For this reason, the only signs as ENA distribution, ACR and GCR anisotropy, must be investigated. Usually, this information is used to validate the computational models, whose aim is to reproduce the data trend.

Pogorelov et al. (2017b) considered the observations of $1-30$TeV GCR anisotropy, from which, taking into account protons, the gyro radii may be as large as 500 au. Therefore, the heliotail must be very long (likely about 2×10^4 au) to produce an observable anisotropy of 10 TeV.

The heliotail shape depends on the kind of computational model chosen. in fact, if the LISM is supermagnetosonic ($B_\infty \sim 3\,\mu\mathrm{G}$) the kinetic treatment on neutral H atoms becomes critical.

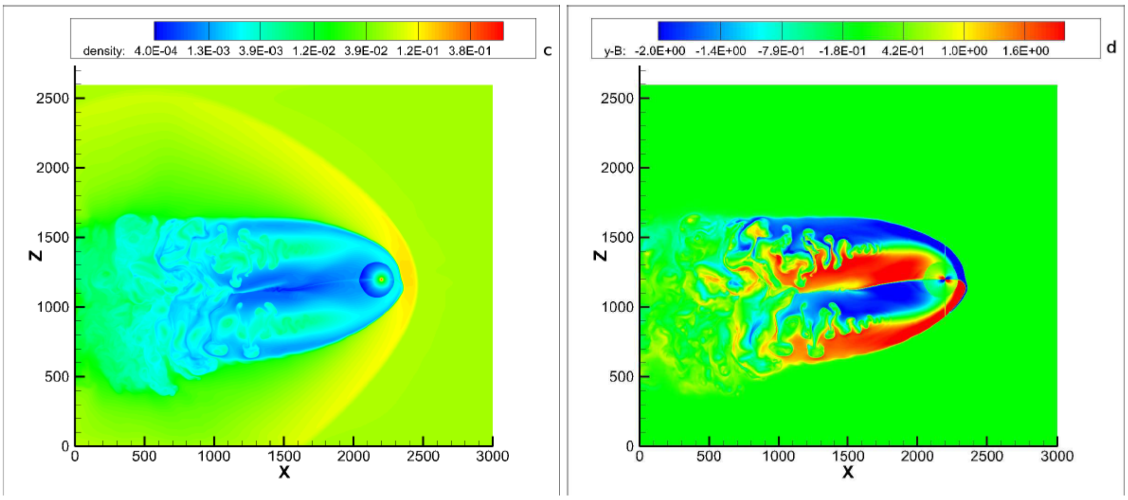

Figure 3.10: The results of n plasma number density and B_y out of plane component comes from a multi-fluid approach, considering a HCS flat,i.e. there is no angle between the Sun's rotation and magnetic axes. In the left panel the hydrogen wall in front of the HP is visible. (Pogorelov et al. 2017b)

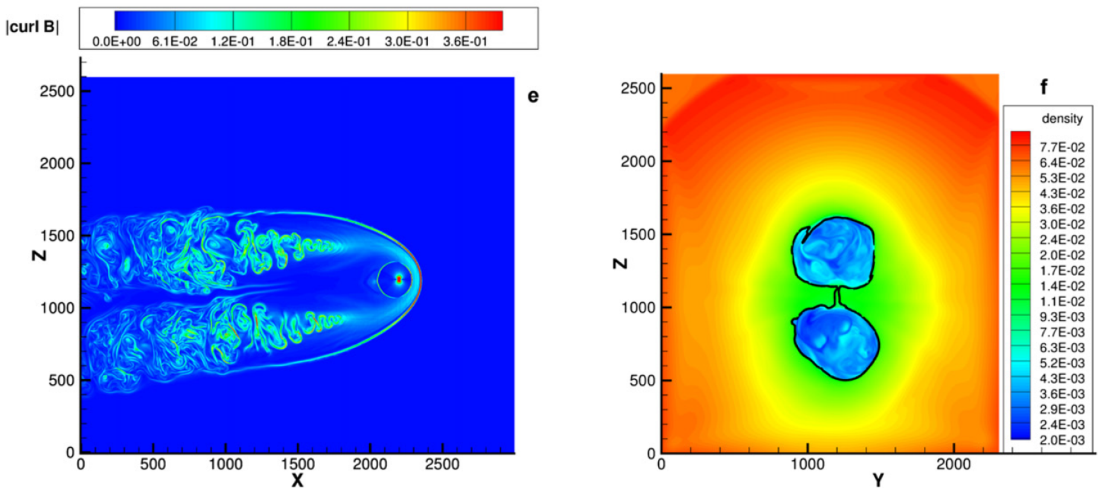

Figure 3.11: (*Left panel*) The curl of B shows clearly the kink instability and the current in the lobes. (*Right panel*) The distribution of the plasma density across the tail ($x = 200\,\mathrm{au}$) shows the northern and southern lobes. The solid line outlines the heliopause. (Pogorelov et al. 2015)

Making the computational work easier, it is possible to disregard the angle between the Sun's rotation and magnetic axes. The result is a flat HCS, in which solar cycle effects are numerically neglected. As shown in figure 3.10, in the heliospheric structure appears two lobes, which are due to the SW plasma gathered inside the Parker spiral field line deflected to the tail by the interaction of the SW with the HP. The heliosphere length is not so long, because of the kink instability which affects the spiral field line, as shown in figure 3.11 . So, the necessity of plasma concentration inside the lobes disappears. This kind of heliosphere structure is called *croissant-like*.

This type of structure is only supported by numerical simulations where the ISMF is parallel to the Sun motion, or the Sun happens to be at rest relative to the LISM (Czechowski et al. 2019).

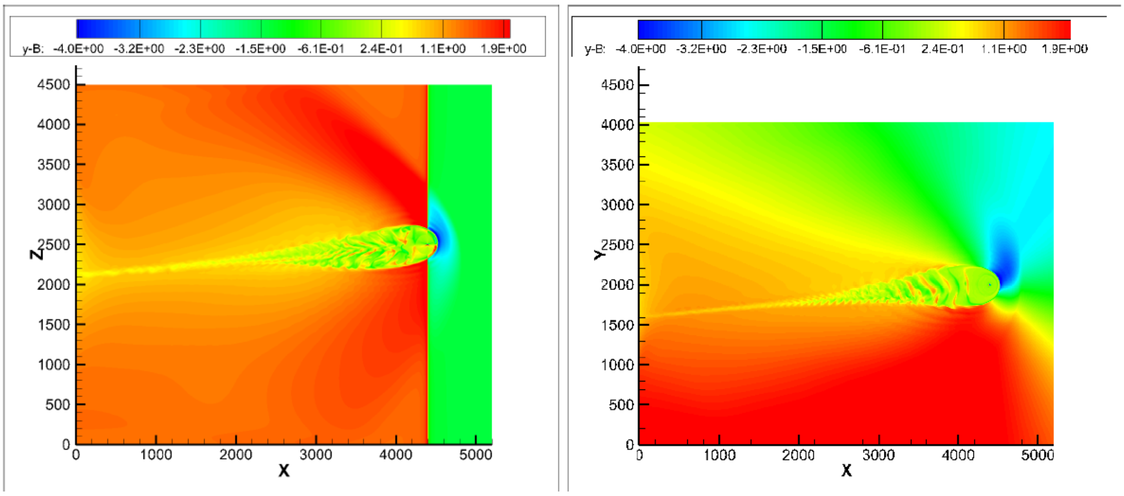

Figure 3.12: Heliosphere structure in the multi-fluid numerical approach, taking into account solar cycle effects. (*Left panel*) Meridional plane. (*Right panel*) Ecliptic plane. (Pogorelov et al. 2017b)

Considering the solar cycle, the two lobes disappears and the SW plasma concentration is higher near the equatorial plane, where the slow SW is. The new heliosphere configuration is called *comet-like*.

It was observed that ENA fluxes coming from upstream and downstream regions are similar in strength. From this observation, a *bubble-like* (or spheroidal-like) structure was hypothesized. The heliotail results to be shorter than the comet-like structure.

A recent study (ibid.) compares the ENA flux observational data, with the data provided by a multi-fluid approach. A wide range of spectra, provided by Voyager probes and IBEX, is considered. As a result, the bubble-like structure is not able to provide the same outcomes of the comet-like structure.

Taking into account the GCR anisotropies and the ENA fluxes, no structure can perfectly reproduces their behaviour. This is likely due to the turbulence, which affects the LISM. From this observation is clear how much is important to understand how MHD turbulence works, in order to implement it into numerical models.

Chapter 4

Magnetic turbulence

In the neutral fluid flows, the concept of turbulence is well known. This kind of motion is characterised as a flow which does not follow the deterministic rules of classical dynamics, thus its details are not predictable. Turbulence is experienced when the flow speed is high. The SW is super-Alfvénic and supersonic, hence the plasma flow can be turbulent as well as the neutral fluid.

Through spacecraft, it is possible to study collisionless plasma characteristics *in situ*. The Voyager probes show that the magnetic field, coupled with the velocity field, modifies the energy cascade. Nowadays, the data available are affected by sparsity and noise, especially in the highest frequency values. For these reasons, the kinetic range cannot be physically evaluated and the studies are focused at low frequencies where large amplitude fluctuations have been observed. It is worth highlighting that this kind of fluctuations are described within the MHD realm.

The chapter is organized as follows. In section 4.1, general information about MHD turbulence equations, energy cascade, Taylor's hypothesis and scaling features of the physical phenomena are given. In section 4.2, statistical tools are explained. E.g. how the fluctuations can be evaluated, or the definition of anisotropy (focusing attention on the difference between trace and variance anisotropy). In section 4.3, velocity and magnetic field spectra of the SW at 5 au (before the TS) are shown. In the last section, the magnetic field spectrum is shown at 88, 106 and 136 au. Hence, at two different points in the IHS and at one point in the OHS (or VLISM; *Very Local InterStellar Medium*). Moreover, differences among IHS and VLISM magnetic field spectra are discussed.

4.1 Theoretical framework

The turbulence is ubiquitous in the space as well as the magnetic field and it is characterised by randomness both in space and in time. This phenomenon is a non linear process in which chaotic dynamics and stochastic process coexist.

There are turbulence typical *structures*, viz. eddies or vortices, which are present at all dynamical scales. When the turbulence is fully developed, there is an infinite number of scales and the flow appears chaotic because of the presence of the eddies. This leads to three gross features:

1. the spatio-temporal evolution of the electromagnetic field appears disordered;
2. a wide range of dynamical scales (inertial range) which overlap one another;
3. the impossibility to predict the flow evolution in detail, but only on average;

thus in a collisionless plasma, as the SW, the turbulence plays an important role in the energy and momentum transport.

The simplest and widest description of the plasma behaviour is MHD. Remembering that this is a particular regime of the one fluid theory, in which the relativity effects are neglected. This approximation allows to model the evolution of plasma with a frequency lower than the ion cyclotron (Larmor) one ω_c.

The shape of the MHD equations for the incompressible case is discussed in section 1.5, here gathered together:

$$\begin{cases} \dfrac{\partial \rho}{\partial t} + \nabla \cdot (\rho \boldsymbol{U}) = 0 \\ \rho \dfrac{d\boldsymbol{U}}{dt} = -\nabla P + \dfrac{1}{c} \boldsymbol{J} \times \boldsymbol{B} \\ \dfrac{1}{\gamma - 1} \rho^{\gamma} \dfrac{d}{dt} \left(P \rho^{-\gamma} \right) = \dfrac{J}{\sigma} \\ \dfrac{\partial \boldsymbol{B}}{\partial t} = \nabla \times (\boldsymbol{U} \times \boldsymbol{B}) \\ \nabla \cdot \boldsymbol{B} = 0 \end{cases}$$

where the CGS is used instead of the MKS units. [1] These equations can be reduced in two dynamical relations and two constraints

$$\begin{cases} \rho \dfrac{d\boldsymbol{U}}{dt} = -\nabla P + \dfrac{1}{c} \boldsymbol{J} \times \boldsymbol{B} \\ \dfrac{\partial \boldsymbol{B}}{\partial t} = \nabla \times (\boldsymbol{U} \times \boldsymbol{B}) \\ \nabla \cdot \boldsymbol{U} = 0 \\ \nabla \cdot \boldsymbol{B} = 0 \end{cases}$$

from which there are three quadratic invariants: the *total energy* $E = \langle U^2 \rangle /2 + \langle b^2/2 \rangle$ ($b = B/\sqrt{4\pi\rho}$ is the magnetic field expressed in units of Alfvén velocity), the *cross helicity* $H_c = \langle \boldsymbol{U} \cdot \boldsymbol{b} \rangle$ which states the degree of correlation between the velocity and the magnetic field (it measures the relative importance of Alven waves in the global fluctuations), and the *magnetic helicity* $H_m = \langle \boldsymbol{a} \cdot \boldsymbol{b} \rangle$, where $\boldsymbol{a}$ is the vector potential and H_m is a measure of the linkage between magnetic flux tubes (it indicates the lack of reflectional symmetry in the flow and is related to the dynamo effect). It is useful to introduce the normalized cross helicity σ_c, which is correlated to the self-production of turbulence and can change in the range $-1 < \sigma_c < +1$ (Iovieno et al. 2016).

The two energy invariants, E and H_c, can be combined in terms of the energy of the Elsässer's variables $E^{\pm} = \langle |z^{\pm}|^2 \rangle = E \pm H_c$ (Vlahos et al. 2009), where the reference equation is the (1.38). This considers the magnetic and velocity fields background and it is written according to the perturbations.

It is worth highlighting that the smallest scale evaluable with the MHD equations must be greater than c_a/ω_c, and that a Maxwellian distribution function for ions and electrons is formally assumed (Turner 2013). Furthermore, non linear coupling occurs only between opposite direction waves, hence the energy is transferred to small scales less efficiently than in the Kolmogorv cascade (K41).

[1] The temperature is measured in K, the electric charge is expressed in the electric CGS system and all the others quantities are measured in the electromagnetic system. In this way, in the equations appear factors as c, but this issue is compensated by the fact that the dimensional check is easier.

4.1.1 Scaling features

The Navier-Stokes dimensionless equations depend on the Re and M (Mach number). In the limit of ideal flow, the equations change into the Euler equations, whose dimensionless shape formally keep their original appearance. Therefore, the flow field reaches a limit configuration in which the adimensional values of the variables do not change. In other words, there is a class of solutions which is invariant under scaling transformations (Bruno et al. 2013).

When taking care of the magnetohydrodynamic case, a scaling transformation $l \to \lambda l'$ must be considered. Doing the same thing to the following variables

$$\boldsymbol{u} \to \lambda^h \boldsymbol{u'} \quad \boldsymbol{B} \to \lambda^\beta \boldsymbol{B'}$$

the MHD equations remain unchanged and provide

$$P \to \lambda^{2\beta} P' \quad T \to \lambda^{2h} T'$$

from which $\rho \to \lambda^{2(\beta-h)}\rho'$. Obviously $h \neq \beta$ in general, thus magnetic and velocity fields have different scalings. In the incompressible limit $\rho = const.$, hence $h = \beta$ due to the exponent of the scaling function $2(h-\beta) = 0$. Said differently, in the incompressible limit there is no difference between velocity and magnetic field scaling features.

4.1.2 The energy cascade

Richardson theorised that turbulence is made by vortices at all scales. Thus, energy is injected at a large scale L and is piled out to small scale due to non linear interactions, up to the dissipation scale l_d. The energy rate at the injection scale is given by $\epsilon_L \sim U^2/\tau_L$, where $\tau_L \sim L/U$ is the characteristic time at this scale. Regarding the dissipation scale, the energy rate is $\epsilon_d \sim U^2/\tau_d$, where $\tau_d \sim L^2/\nu$ is the time scale at which dissipation acts. The ratio between the two energy rates is

$$\frac{\epsilon_L}{\epsilon_d} \sim \frac{\tau_d}{\tau_L} \sim Re$$

hence, the larger is the Re value, the bigger is the distance between the injection and the dissipation scale. In other words, the system is not able to dissipate the whole energy leading into the injection scale, therefore the excess of energy must be dissipated at small scales (in which the characteristic length is also smaller then the Reynolds number and the dissipation becomes more efficient). The turbulence is said as *fully developed* when both the Re and the number of scales tends to infinity.

Assuming periodic boundary conditions, the phenomenon can be investigated through the Fourier coefficients method. In addition, to simplify the problem, MHD equations must be written in the Elsässer's variables, resulting in

$$\left(\frac{\partial \boldsymbol{z}_{\boldsymbol{k}}^{\pm}}{\partial t} \mp i\boldsymbol{k} \cdot \boldsymbol{c_a} \boldsymbol{z}_{\boldsymbol{k}}^{\pm}\right) = -i\boldsymbol{P}(\boldsymbol{k}) \int_{\boldsymbol{k}} \boldsymbol{z}_{\boldsymbol{p}}^{\mp} \boldsymbol{z}_{\boldsymbol{q}}^{\pm} d^3\boldsymbol{q} \tag{4.1}$$

where $\boldsymbol{P}_{ilm}(k) = k_m[\delta_{il} - (k_i k_l/k^2)]$ and $(\boldsymbol{k}, \boldsymbol{p}, \boldsymbol{q})$ are the wave vectors related by the triangular relation $\boldsymbol{k} = \boldsymbol{p} + \boldsymbol{q}$. This equation demonstrates the difference between the hydrodynamics and the MHD: two Alfvén waves, which propagate in opposite directions along the mean field, are coupled by the non linear effects.

Including the Alfvén wave in the field definition

$$\widehat{\boldsymbol{z}_{\boldsymbol{k}}^{\pm}}(t) = \boldsymbol{z}_{\boldsymbol{k}}^{\pm}(t) e^{\mp i\boldsymbol{k}\cdot\boldsymbol{c_a} t}$$

where $\boldsymbol{r} = \boldsymbol{c_a} t$ is the position vector with respect to the reference system. The divergence-less condition leads to the insight that not all the Fourier modes are independent. The modes available in the MHD are two: $z_1^{\pm}(\boldsymbol{k},t)$ describes the amplitude behaviour of the Alfén mode and $z_2^{\pm}(\boldsymbol{k},t)$ represents the amplitude of the magnetosonic mode (remembering the incompressible limit).

The Fourier governing equation (4.1) becomes

$$\frac{\partial \widehat{\boldsymbol{z}_{\boldsymbol{k}}^{\pm}}}{\partial t} = -i\boldsymbol{P}(\boldsymbol{k}) \int_{\boldsymbol{k}} \widehat{\boldsymbol{z}_{\boldsymbol{p}}^{\mp}} \widehat{\boldsymbol{z}_{\boldsymbol{q}}^{\pm}} e^{\mp i\boldsymbol{p}\cdot\boldsymbol{c_a} t} d^3\boldsymbol{q} \tag{4.2}$$

clearly the integral oscillates except when $\boldsymbol{p}$ and $\boldsymbol{c_a}$ are orthogonal.This means that there are no resonant modes apart from in the previous case.

After some algebra and introducing the spectral pseudo energy $E^{\pm}(k,t) = 4\pi k^2 q^{\pm}(k,t)$, where $q^{\pm}(k,t)$ is an arbitrary odd function of k, it is possible to demonstrate that the non linear term of the governing equations conserves the $E^{\pm}(t)$ separately. Besides, the redistribution of the energy over different wave vectors is due to the non linear terms.

Iroshnikov-Kraichnan cascade

Differently from the K41 theory, Iroshnikov and Kraichnan studied the energy cascade considering the magnetic field, in particular the strong magnetic field case. The main assumption is the *isotropic* turbulence. This theory is based on the Alfvén effect, which is the decorrelation of interacting eddies. The physical meaning lies in the fact that interaction occurs only among opposite propagating fluctuations. This can be seen in the equation (4.2), in which the absence of resonant modes is due to the lower intensity of the non linear effects compared to the neutral case. Therefore the energy cascade is slowed down. It is worth knowing that another effect of the magnetic field is to make the cascade anisotropic.

Introducing the field increments $\Delta z_l^{\pm}(\boldsymbol{r}) = [\boldsymbol{z}^{\pm}(\boldsymbol{r}+l) - \boldsymbol{z}^{\pm}(\boldsymbol{r})]\cdot\boldsymbol{e}$- where $\boldsymbol{e}$ is the longitudinal direction and $\Delta z_l^{\pm}$ a stochastic quantity representing the fluctuations across eddies at the scale l and for the scale invariance $\Delta z_l^{\pm} \sim l^h$- all the properties of the stochastic field variables are functions of the scale l, of the pseudo energy dissipation rates per unit mass $\varepsilon^{\pm}$ and of the viscosity ν. Keeping in mind that the viscosity dependence is only felt at small scales. The pseudo energy dissipation rates are scaled as $\varepsilon^{\pm} \sim (\Delta z_l^{\pm})^2/T_l^{\pm}$, where $T_l^{\pm}$ is the characteristic time needed to transfer the energy from an eddy to another one. Unlike the fluid case, wherein the characteristic time corresponds to the *eddy turnover time* [2], in the magnetically dominated case the characteristic time is increased by a factor $t_l^{\pm}/t_A$, where $t_A \sim l/c_a < t_l^{\pm}$ is the Alfvén time [3]. Then the characteristic time is $T_l^{\pm} \sim (t_l^{\pm})^2/t_A$ and the pseudo energy rates are

$$\varepsilon^{\pm} \sim \frac{[\Delta z_l^{\pm}]^2[\Delta z_l^{\mp}]^2}{lc_A}$$

where it is clear that the energy rates follow the same scaling laws for each $\pm$ modes, highlighting the fact that the amplitude of both ε^+ and ε^- can be different.

As in paragraph 4.1.1, the dissipation rate is scaled like $\varepsilon \to \lambda^{1-4h}\varepsilon'$. Hence, when $\varepsilon^+ \sim \varepsilon^-$, the scaling law results

$$\Delta z_l^{\pm} \sim (\varepsilon c_A)^{1/2} l^{1/4}$$

[2]The eddy turnover time is the typical time scale for an eddy of length scale l to undergo significant distortion, and it is defined as $t_l \sim l/u_l$ (in the magnetically dominated case $t_l^{\pm} \sim l/\Delta z_l^{\mp}$).

[3]This is the Alfvén effect. The cascade is slowed down even if there is no background field, because the Elsässer's field at a certain scale faked the effect of a stochastic mean field c_a^s in the lower scale. Thus, the Alfvén interacting packets need more time to decay into lower wavelenght packets.

from which the pseudo energy spectrum is found as

$$E^{\pm}(k) \sim (\varepsilon c_A)^{1/2} k^{-3/2} \tag{4.3}$$

named *Iroshnikov-Kraichnan spectrum* (IK), where $k \sim 1/l$ is the wave length.

When the linear Alfvén time t_A and the non linear time scale $t_l^{\pm}$ are of the same order of magnitude, the energy cascade is said *critically balanced*. In this eventuality, the power spectrum is scaled as $f^{-5/3}$ if $\theta_B \sim 90°$, where θ_B is the angle between the flow direction and the mean field direction, otherwise the spectrum is scaled as f^{-2} if $\theta_B \sim 0°$. In the latter case, the spectrum would also have a smaller energy content than in the other case.

The main difference between the K41 and the IK consists in the different dependence on the frequency, the K41 is $\propto k^{-5/3}$, while the IK is $\propto k^{-3/2}$, but both the theories are referred to the isotropic turbulence case.

Goldreich-Sridhar cascade

The first *anisotropic* turbulence theory, in the MHD inertial range, was developed by Goldreich and Sridhar in the 1995, from which it took its name.

By considering the equation (4.1), non linear fluxes depend on the angle among the mean field and the wave vector direction ($\boldsymbol{k} \cdot \boldsymbol{c_a}$). Thus, assuming wave packets with small parallel component and a strong equilibrium mean field, the turbulence in the perpendicular field results to be the same as those in three dimensional hydrodynamic, the K41. In this case, the bidimensional MHD is valid in the perpendicular plane and the propagating Alfvén waves couple different planes along B_0. This leads to $\tau_{\parallel} \sim \tau_{\perp}$, which corresponds to the distance that the perpendicular plane must be advected in the parallel direction before a loss of correlation. In other words, the critical balance condition explaned before can be written as

$$c_a k_{\parallel} \sim \mathcal{U}_{\perp} k_{\perp}$$

where $\mathcal{U}_{\perp}$ is the typical speed in the perpendicular plane and $k_{\parallel}$, $k_{\perp}$ are the components of the wave vector with respect to the mean field. Due to the K41 validity in the perpendicular plane $\mathcal{U}_{\perp} \propto k_{\perp}^{-1/3}$, hence

$$k_{\parallel} \sim k_{\perp}^{2/3}$$

the anisotropy increases with decreasing scale. The energy spectrum depends on both the components of the wave vector as

$$\begin{cases} E^{\pm}(k_{\perp}) \sim k_{\perp}^{-5/3} \\ E^{\pm}(k_{\parallel}) \sim k_{\parallel}^{-2} \end{cases} \tag{4.4}$$

calling that *Goldreich-Sridhar* theory (GS95). Highlighting that the parallel spectrum develops only if $k_{\parallel} < k_{\perp}$ and the cascade in the $k_{\perp}$ direction follows the K41 law because the magnetic field influence motion which bends it. Obviously, perpendicular eddies are smaller than the parallel ones, therefore bending the magnetic field lines is more difficult.

It is worth noting that when the critical balance condition is not valid ($k_{\parallel}$ too small), the magnetic tension is too weak to affect the dynamics and the turbulence evolves hydrodynamically towards the increasing isotropy direction. Otherwise, when $k_{\parallel}$ is large the magnetic tension dominates, the critical balance is restored and the non linear cascade develops in the $k_{\perp}$ direction.

The MHD turbulence is characterized by two kinds of motion, parallel and perpendicular to the magnetic field, which are waves and eddies respectively. The main result of the GS95 is to show this duality.

4.1.3 Taylor's hypothesis

In this thesis it is important to mention the work carried on by Taylor in 1938. It was originally thought for the hydrodynamic turbulence, but it can be extended to the plasma realm. Taylor hypothesized that time series recorded at a fixed point in space can be used to evaluate the spatial pattern of turbulence. This statement is known as *frozen in* condition and it is valid when the mean flow velocity is much greater than the root mean square (rms) of the fluctuations.

This hypothesis is essential to change the reference frame without affecting the properties of the flow. Indeed, the Voyager probes send time series signal in the spacecraft (SC) reference frame. Throughout the *Doppler shift* relationship, the plasma and SC reference frame can be linked together

$$f_{SC} = f_{PL} + (2\pi)^{-1}\boldsymbol{k} \cdot \boldsymbol{U_{rel}} \tag{4.5}$$

where $\boldsymbol{U_{rel}} = \boldsymbol{U_{SW}} - \boldsymbol{U_{SC}}$ is the relative speed among the SC and the SW.

If the Taylor's hypothesis is valid, $|\boldsymbol{k} \cdot \boldsymbol{U_{rel}}|(2\pi)^{-1} \gg f_{PL}$, the wave number in the relative wind flow direction can be evaluated starting from the frequencies measured in the SC reference frame. In the SW, at large scales, the flow is super Alfvénic and supersonic, thus the frozen-in condition occurs, due to the low speed of the SC compared to the SW. Indeed, upstream the TS the ratio $U_{SC}/U_{SW} < 0.05$, but in the IHS the condition may change. At V2 $U_{SC}/U_{SW} \sim 0.1$ and considering that the angle between B and U is approximately $\pi/2$, the perpendicular wave number can be calculated as $k_\perp \approx 2\pi f_{SC2}/U_{SW}$, using the Taylor's hypothesis. At V1 the condition validity may be subordinated to the SW region. In fact in the slow wind region the frozen in condition is no more valid. (Fraternale et al. 2019a)

4.2 Statistical tool

A turbulent flow is sensitive to small perturbations due to the intrinsic instability of the dynamics. Small perturbations are ubiquitous in space, then it is important to understand how data sets must be elaborated to study the turbulence.

4.2.1 Fluctuations

The averaging process takes a fundamental importance in the statistical approach. Predictability in turbulence it can be reached only for the global quantities, while fluctuations depend on the initial perturbations in the boundary conditions.

The term fluctuation can be interpreted in different ways, but it still indicates the deviation from the equilibrium. Defining ψ as a physical quantity, which is a time-series vector, the general relation for the fluctuations is

$$\delta\psi(x,t) = \psi - \langle\psi\rangle \tag{4.6}$$

where brackets stand for some kind of averaging process. The first way to calculate the average of ψ is through the *ensemble average*, which is time independent and is used when different time-series, named realizations, are available. The realizations must be achieved under the same external conditions. The second type of average is the *time average*, which is time dependent and can be used when only one realization is available. This is useful just if the turbulence is statistically stationary. The last way to compute the average is the *space average*, where the fluctuations at scale l are indicated as $\Delta\psi_l$. This is useful only with statistically homogeneous flows.

The data sets provided by probes can be considered as time-series at single points[4], therefore

[4]The Voyagers data are manged by NASA and are provided freely on the official web site (https://omniweb.

the time average is the best choice. Besides, through the *ergodic theorem* the time and the enseble averages coincide. It is worth noticing that Matthaeus et al. (1982) concluded that, excluding coherent and organized structures in the data sets, the interplanetary magnetic field (IMF) behaves as a stationary and ergodic function of time. This is no longer valid in the solar wind, where the magnetic field depends on the time scales and on the type of wind (interacting region, slow or fast flow).

4.2.2 Power spectral density

Determining the dissipation and the energy transfer rates is of fundamental importance in the turbulence problems. The simplest way to obtain these quantities, from the in situ data, is by means of the *power spectral density* (PSD). PSD can be defined as the energy, per unit frequency, of the signal and it is a positive even function.

Before showing how the PSD is computed, the two-point two-time *correlation tensor* R^{ψ}_{ij}, for the generic quantity ψ, must be presented

$$R^{\psi}_{ij}(\boldsymbol{r}, t) = \langle \psi_i(\boldsymbol{r}, t)\psi_j(\boldsymbol{r} + \Delta\boldsymbol{r}, t + \tau)\rangle$$

where $\boldsymbol{r}$ is the vector position with respect to the reference frame used, t is the time, $\Delta\boldsymbol{r}$ and τ are the space and temporal scale of separation, respectively. Usually, the speed of the SC is much lower than the SW speed and the spatial scale is much bigger than the SC dimension. Therefore, the measurements can be considered as taken at a fixed-point. Through the Taylor's hypothesis $\Delta\boldsymbol{r} = U\tau\boldsymbol{e_r}$ can be written, where U is the module of the speed of the SC and $\boldsymbol{e_r}$ is the versor in the radial direction. Replacing $\Delta\boldsymbol{r}$ in the definition of correlation tensor, one obtains

$$R^{\psi}_{ij}(\Delta\boldsymbol{r}) = \langle \psi_i(\boldsymbol{r})\psi_j(\boldsymbol{r} + \Delta\boldsymbol{r})\rangle \tag{4.7}$$

the two-point one-time correlation tensor. Considering the perturbations of the field ψ, the statistical information about the state of the turbulent flow are contained in this definition. The magnetic field auto-correlation tensor is

$$R^{b}_{ij}(\Delta\boldsymbol{r}) = \langle b_i(\boldsymbol{r})b_j(\boldsymbol{r} + \Delta\boldsymbol{r})\rangle, \tag{4.8}$$

the velocity auto-correlation tensor

$$R^{v}_{ij}(\Delta\boldsymbol{r}) = \langle v_i(\boldsymbol{r})v_j(\boldsymbol{r} + \Delta\boldsymbol{r})\rangle, \tag{4.9}$$

and the cross-correlation tensor

$$R^{vb}_{ij}(\Delta\boldsymbol{r}) = \langle v_i(\boldsymbol{r})b_j(\boldsymbol{r} + \Delta\boldsymbol{r}) + b_i(\boldsymbol{r})v_j(\boldsymbol{r} + \Delta\boldsymbol{r})\rangle, \tag{4.10}$$

naming v and b as the fluctuations of the velocity and the magnetic field respectively. The auto-correlation is an even positive function. Sometimes the correlation is normalized by dividing it by the standard deviation of both the signals. In this case $-1 < R_{ij} < 1$. It is worth noticing that in the homogeneous turbulence these tensors are invariant.

`gsfc.nasa.gov/coho/`). The data are available in different resolutions, the finest is the 48 s. This time-series are averaged before they are published. The magnetic field is sampled at rate of 2.08 samples per second.

Applying the Fourier or the wavelet transformation to the correlation tensors, it is possible to define the PSD tensor [5] as

$$P_{ij}^{b}(\boldsymbol{k}) = \frac{1}{2\pi}\int R_{ij}^{b}(\Delta\boldsymbol{r})e^{-i\boldsymbol{k}\cdot\Delta\boldsymbol{r}}d^3r \tag{4.11}$$

$$P_{ij}^{v}(\boldsymbol{k}) = \frac{1}{2\pi}\int R_{ij}^{v}(\Delta\boldsymbol{r})e^{-i\boldsymbol{k}\cdot\Delta\boldsymbol{r}}d^3r \tag{4.12}$$

$$P_{ij}^{vb}(\boldsymbol{k}) = \frac{1}{2\pi}\int R_{ij}^{vb}(\Delta\boldsymbol{r})e^{-i\boldsymbol{k}\cdot\Delta\boldsymbol{r}}d^3r \tag{4.13}$$

where $\boldsymbol{k}$ is the wave vector. The information provided by in situ experiments are detected by a single probe, then the space separation scale is one-dimensional $\Delta\boldsymbol{r} = (\Delta r_1,0,0)$. Therefore, only reduced spectrum can be computed

$$P_{ij}^{\psi} = \frac{1}{2\pi}\int R_{ij}^{\psi}(\Delta r_1,0,0)e^{-i\boldsymbol{k_1}\cdot\Delta\boldsymbol{r_1}}dr_1 = \int P_{ij}^{\psi}(\boldsymbol{k})dk_2dk_3 \tag{4.14}$$

integrating over the two transverse k; complete information of the PSD get lost, unless the flow is isotropic (in this case the spectral information are the same in any direction).

It should be highlighted that the Fourier transformation was used, hence the quasi-stationarity condition was implicitly assumed. It is well known that the SW is not a steady flow, but in specific ranges of time this condition can be considered valid, so the data time intervals have to be chosen accurately.

Remembering that the physical meaning of power is the energy amount converted per unit of time, one can conclude that defining the PSD of a time series and multiplying it by the temporal interval, the energy spectral density (ESD) can be obtained.

4.2.3 Generalized structure functions

In statistics, the *moments* of a function are quantitative measures of the shape of the function's diagram. The *generalized structure functions* (GSF), or shortly the structure functions, are a way to quantify the scaling behaviour of moments of a *probability distribution function* (PDF).

Considering the increments of a generic quantity $\Delta\psi(\boldsymbol{r}) = \psi(\boldsymbol{r}) - \psi(\boldsymbol{r}+l)$, as done in section 4.1.2. It is impossible to have the values of ψ in different position at the same time. Therefore the Taylor's hypothesis should be evoked, in this way the time series provided by in situ measurements can be used. The p-th structure functions are defined, for speed and magnetic field respectively, as

$$R_p(\tau) = \langle|\Delta u_\tau|^p\rangle \tag{4.15}$$

$$S_p(\tau) = \langle|\Delta b_\tau|^p\rangle \tag{4.16}$$

where p is the order moment, $\Delta u_\tau = U(t+\tau) - U(\tau)$, $\Delta b_\tau = B(t+\tau) - B(\tau)$ and τ the time lag. Considering that Δu_τ is the radial velocity component, regarding Δb_τ, the longitudinal component can be chosen in accordance with one among three different reference systems (RNT, local background magnetic field or minimum variance direction; see appendix...).

It is worthwhile remembering that the only exact relations, which define the inertial range, are the Kolmogorov's law

$$\langle\Delta v_l^3\rangle = -\frac{4}{5}\epsilon l$$

[5]The *variance anisotropy* is the study of the anisotropy among the various elements of the PSD tensor. The *trace anisotropy* is the study of the trace of the PSD tensor.

and the Yaglom's law[6]

$$\langle \Delta z_l^{\mp} \left|\Delta z_i^{\pm}\right|^2 \rangle = -\frac{4}{3}\epsilon_{ii}^{\pm} l,$$

which are valid assuming: global homogeneity, local isotropy, incompressibility, kinematic viscosity equal to magnetic diffusion ($\nu^{\pm} = \nu^{\mp} = \nu \to 0$). Notice that l is the separation along the streamwise x-direction.

The second and the third order moments are direct measurements of the energy density and dissipation rate respectively, as shown by the Kolmogorov's and Yaglom's laws. The odd moments have a large degree of uncertainty, indeed the number of dataset points will increase as much as the value of p increases.

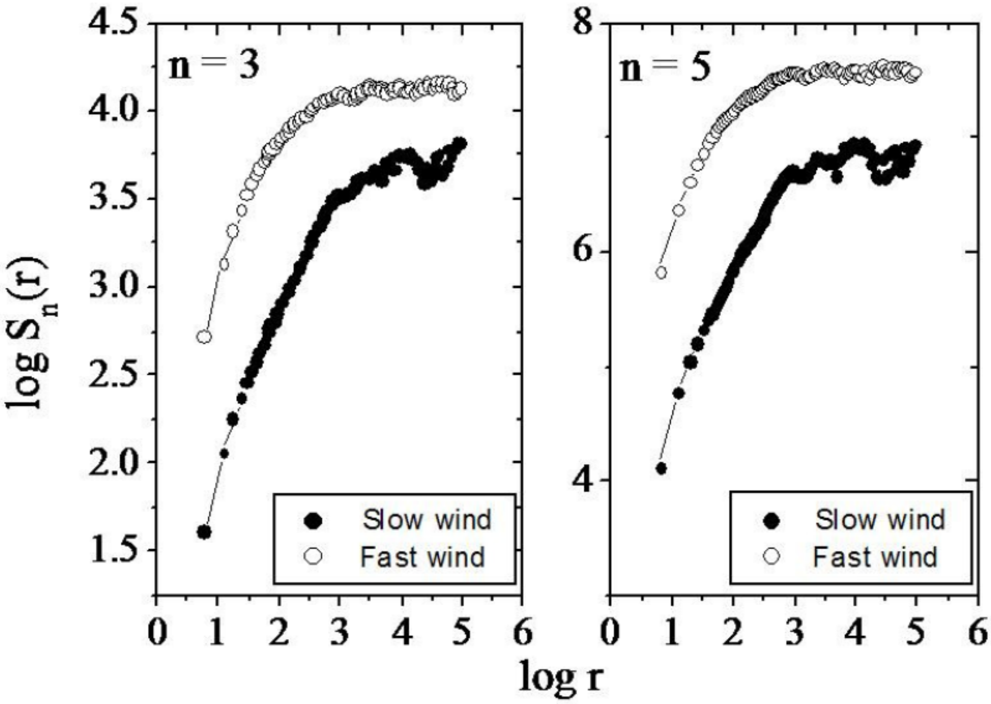

Figure 4.1: Structure functions of magnetic field for slow and fast wind at 0.9 au. The orders considered are $n = 3$ and $n = 5$. In this image the time scale is expressed as r. (Bruno et al. 2013)

Looking at figure 4.1 it is clear that at large scales the structure functions reach a limit, viz. the fluctuations at large scales are uncorrelated. But in the region where S_p increases, the Extended Self-Similarity (ESS) can be used. Therefore, in the inertial range a power law can be found for both the magnetic and velocity field

$$S_p(\tau) \sim \tau^{\xi_p}$$
$$R_p(\tau) \sim \tau^{\zeta_p}$$

[6]The third order moments is different from zero, hence there is a phase correlation or a non Gaussian feature at work. Furthermore, the minus sign means that there is a direct cascade towards smaller scales.

where ξ_p and ζ_p are the scaling exponents, which can be computed through a linear fit. An empirical criterion exists defining the limit of the order moments calculable, $p_m \simeq \log N$, where N is the number of points in the datasets. When $p > p_m$, structure functions cannot be determined accurately.

4.2.4 Intermittency

Up to now the inertial range has been considered as well defined, but this is not true. Indeed figure 4.1 shows that the situation is similar to the low Reynolds case in the hydrodynamics realm: the inertial range is not well defined.

Considering the hydrodynamic case, the three-dimensional turbulence is made of vortex tubes, which are created and stretched because of the non-linear effects. The vortex stretching is a phenomenon in which vortex tubes decrease their cross-sectional area and increase their vorticity. These tubes are characterised by a width similar to the Kolmogorov dissipation scale and length similar to the integral scale; thus, the turbulence has a filamentary structure. Remembering that the vorticity is strictly related to the speed gradient, there are areas with higher speed gradients, since the tubes are unequally distributed throughout space. The energy dissipation rate depends mainly on the speed variation in the space, thus there are areas with stronger dissipation than the surrounding ones. This phenomenon is called *intermittency.*

Intermittency is also observed in the MHD turbulence and the role of the vortex tubes is thought to be taken by the current sheets, in other words, current sheets are responsible for intermittency in MHD turbulence (Turner 2013).

As said before, the only exact relations known are the Kolmogorv's and Yaglom's laws, for the hydrodynamic and the MHD respectively. In these theories, the energy dissipation rate is considered as constant, i.e. the spatial average values is taken into consideration. Taking into account that ϵ is related to the third order GSF, the dissipation rate of the p-th order can normalized with the third order moment

$$S_q(\tau) = [S_3(\tau)]^{\alpha_3(q)}$$

where $\alpha_3(q)$ is the relative exponent.

It is worthwhile highlighting that in the ESS case, the structure functions follow a linear relation, that is $\xi_p = hp$. Thus the aim of the intermittency studies is to predict the non self-similar behaviour of the SW, through the comparison between the ESS and real cases. It is proved that the magnetic field is more intermittent than the velocity field.

The intermittency has consequences in the PDF, as a matter of fact the Gaussian PDF implies the self-similarity of the solution, but the current sheets (vortex tubes in the HD case) are unequally distributed in space thus the PDF has a fat tail, which scales as $\exp(-|x|)$.

4.2.5 Anisotropy

When the Elsässer's variables have been introduced, the difference between the hydrodynamic and MHD has been explained. Namely, in the Navier-Stokes equations the background field can be removed troughout a transformation. Because of the coupling of the magnetic and velocity field, in the MHD does not exist a transformation able to remove the background field, therefore, there is a preferred reference of system.

Variance anisotropy

The Alfvén waves are an exact solution of the MHD equations, apart from their amplitude. The SW turbulence is said Alfvénic because the main role is played by the Alfvén waves and considering that fluctuations are incompressible, the Alfvén waves are perpendicular to the background magnetic field. This does not exclude the presence of parallel fluctuations, which are a proxy for density compression. In other words, the Alfvén waves are consistent with the compressive modes, which play a minor role.

Definition. The study of the components of the fluctuations with respect to the background magnetic field is called *variance anisotropy.*

Considering that in this case the anisotropy must not be confused with any anisotropy of the wave vector distribution (Smith et al. 2005).

Many authors observed the anisotropic behaviour in both IMF and velocity fluctuations, thus following the general equation of the fluctuations 4.6, the magnetic field can be decomposed into the background $\boldsymbol{B_0} = B_0\hat{\boldsymbol{e}}_z$ and the fluctuations $\delta\boldsymbol{B}$ fields. The latter field is made up of parallel fluctuations $\delta B_\parallel = \delta\boldsymbol{B}\cdot\hat{\boldsymbol{e}}_z$ and perpendicular fluctuations $\delta\boldsymbol{B}_\perp = \delta\boldsymbol{B}\times\hat{\boldsymbol{e}}_z$. Noticing that the perpendicular field is a vector made of two components. The SW velocity direction $\hat{\boldsymbol{e}}_v$ can be used as a reference axis, which allows completing the reference frame as $\hat{\boldsymbol{e}}_x = \hat{\boldsymbol{e}}_z\times\hat{\boldsymbol{e}}_v$, $\hat{\boldsymbol{e}}_y = \hat{\boldsymbol{e}}_z\times\hat{\boldsymbol{e}}_x$ and $\hat{\boldsymbol{e}}_z$. Thus, the fluctuations field is $\delta\boldsymbol{B} = (\delta B_\parallel, \delta B_{\perp x}, \delta B_{\perp y})$. In the SW was found that the average power is anisotropically distributed in the coordinate system $(\hat{\boldsymbol{e}}_x, \hat{\boldsymbol{e}}_y, \hat{\boldsymbol{e}}_z)$ as 5:4:1.

Using the minimum variance method, this anisotropy in the power distribution is more clear. This method consists in changing the reference system minimizing the eigenvalues λ of the matrix

$$S_{ij} = \langle B_iB_j\rangle - \langle B_i\rangle\langle B_j\rangle$$

where i and j are the components of the magnetic field in the given reference system. The three eigenvectors $\tilde{V}$ are directed along the three axes of the new reference system. One of the eigenvalues is always much smaller than the others $\lambda_1 \ll \lambda_2, \lambda_3$ and it indicates the minimum variance direction. Moreover, the magnetic fluctuations are confined in the plane defined by $(\tilde{V}_2, \tilde{V}_3)$ perpendicular to $\tilde{V}_1$. In this plane the fluctuations are anisotropically distributed $\lambda_3 > \lambda_2$, namely typical values are $\lambda_3 : \lambda_2 : \lambda_1 = 10 : 3.5 : 1.2$. The direction $\tilde{V}_1$ is nearly parallel to the background magnetic field $\boldsymbol{B_0}$. In the OHS the degree of anisotropy (the ratio among the power perpendicular to and that along $\tilde{V}_1$) decreases with the heliocentric distance. At odds, in the inner heliosphere, the degree of anisotropy increases with distance (Bruno et al. 2013). Regarding the velocity fluctuations, the minimum variance vector is aligned with the radial direction.

Trace anisotropy

The trace anisotropy is the study of the diagonal components of the PSD tensor, which represent the energy density of the fluctuations. As explained in section 4.2.2, only the reduced one-dimensional spectrum can be computed and the trace is $P^T = \sum_i P_{ii}$.

The power is found as always being anisotropic, thus the importance of this kind of studies is looking for the spectral exponents and the relative powers $P^T_\parallel$ and $P^T_\perp$. This is of interest to verify theories, like the GS95, which predict the behaviour of the anisotropic flows.

4.3 Turbulence before the termination shock

The Voyager 2 probe (V2) was launched on 23 August 1977 and crossed the TS at 84 au in 2007, before this shock the SW has been detected as super-Alfvénic and supersonic. In the following section the turbulence structure at 5 au (reached in the 1979) is analised, by using the V2 data.

The sampling rate of the instruments on board are 96 s and 48 s for the plasma and the magnetic fields respectively. Thus, obtaining the PSD is only possible whether six month time series is considered. For this reason, both Fraternale et al. (2016) and Gallana et al. (2016) considered the data from 1 January to 29 June 1979, which period corresponds to the day-of-year (DOY) $1-180$.

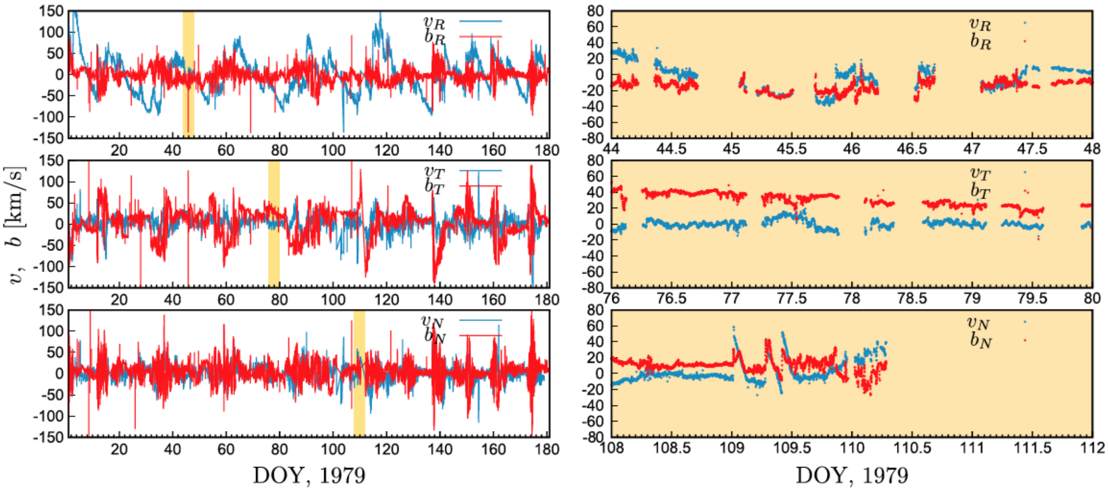

Figure 4.2: In the left column are shown the plasma velocities (red lines) and the magnetic fields (blue lines) provided by V2 in the first 180 day of 1979. Noting that the magnetic field is reported in Alfvén units, in this way it allows a direct comparison with velocity fluctuations. In the right column different zooms, made on the 180 day time period, are shown to highlight the irregular distribution of the data sparsity. The RTN reference system is adopted. (Gallana et al. 2016)

Table 4.1: Data information about plasma and magnetic field during the 1979. n is the total number of samples. δt_s is the data resolution. δt is the temporal range between two consecutive data points. The ensemble average is indicated by the angle brackets. The length of a subset without missing points is L_s. (Fraternale et al. 2016)

1 January-29 June	n	δt_s[s]	δt_{min}[s]	δt_{max}[s]	$\langle\delta t\rangle$[s]	$L_{s,max}$[h]	Missing data
Plasma	115 102	96	9.6	44.7	134	19.8 (at DOY 176)	28%
Magnetic field	248 159	48	4.8	44.6	63	19.5 (at DOY 168)	24%

Voyager 2 data are affected by sparsity, mainly due to the Canberra Antenna of the Deep Space Network being the only one able to track and to receive the V2 data, but the field-of-view is limited to $12\,\mathrm{h\,d^{-1}}$. Moreover, there are smaller gaps and noise because of the interference between instruments, errors in measurement chain and temporal sequence of both the propulsion and thruster system. It is worth highlighting that the structure of the data gaps influence the power spectra of the physical quantities, this is why the method chosen to recovery the gaps is of primary importance. In particular, the algebraic decay is underestimated and the PSD inherits the characteristic of the gapped signal, showing discrete peaks. This feature can be neglected when data sparsity is lower than 10%, is mildly evident around 30% and is destructive when reaches 90%. During the 1979, the amount of data sparsity was 25% overall (see figure 4.2), whose 24% of magnetic field and 28% of plasma velocity (see table 4.1).

4.3.1 SW behaviour near 5 astronomical units

The reference system adopted is the RTN Heliographic, which is spacecraft (SC) centered. The radial (R) axis starts from the Sun and passes through the SC. The tangential (T) one is recovered by a cross product between the Sun rotation axis, which is northward oriented, and the R one. The normal (N) axis is achieved using the right-hand rule.

As said in the previous chapters, the SW velocity is not constant; quite the opposite, it can be fast or slow and in any case it decreases moving away from the Sun. This leads to the formation of interacting regions and shocks. Most of the SW at 5 au has been shocked at least once: this has an effect on the PSD.

Table 4.2: Average quantities from V2 data in the period 1979 (DOY $1-180$).

	Parameter	Value
U_{SW}	Mean velocity	$4.54 \times 10^2\,\mathrm{km\,s^{-1}}$
B_0	Mean magnetic field	$9.81 \times 10^{-1}\,\mathrm{nT}$
c_a	Alfvén velocity	$4.94 \times 10^1\,\mathrm{km\,s^{-1}}$
c_s	Ions sound speed	$1.93 \times 10^1\,\mathrm{km\,s^{-1}}$
E_v	Kinetic energy	$1.20 \times 10^3\,\mathrm{km^2\,s^{-2}}$
E_m	Magnetic energy	$1.37 \times 10^3\,\mathrm{km^2\,s^{-2}}$
E	Total energy	$2.57 \times 10^3\,\mathrm{km^2\,s^{-2}}$
H_c	Cross helicity	$15.8\,\mathrm{km^2\,s^{-2}}$
H_m	Magnetic helicity	$2.10 \times 10^6\,\mathrm{nT^2\,s^{-2}}$
σ_c	Normalized cross helicity	1.23×10^{-2}
r_A	Alfvén ratio	8.66×10^{-1}
n_i	Numerical denisy	$0.23\,\mathrm{cm^{-3}}$
β_p	Ions plasma beta	0.22
L_{E_v}	Kinetic correlation length	$3.68 \times 10^7\,\mathrm{km}$
L_{E_m}	Magnetic correlation length	$3.75 \times 10^7\,\mathrm{km}$
f_{ci}	Ions Larmor frequency	$0.02\,\mathrm{Hz}$
f_{ip}	Ions plasma frequency	$0.10\,\mathrm{kHz}$
r_{ci}	Ions Larmor radius	$4.29 \times 10^3\,\mathrm{km}$
r_{ip}	Ions inertial radius	$1.58 \times 10^2\,\mathrm{km}$

The period considered corresponds to the slow wind, where the mean velocity is less than $500\,\mathrm{km\,s^{-1}}$ and the fluctuations are larger than in the fast SW. In the slow wind the magnetic energy per unit mass is higher than the kinetic one and it is included between 53% and 70%, in the period evaluated it is about 53% (Fraternale et al. 2016). Looking at figure 4.2, the speed fluctuations are higher than those of the magnetic field in the radial direction, while in both the tangential and normal directions the magnetic field fluctuations are slightly higher. As a matter of fact the β-parameter is lower than 1, hence the magnetic pressure is larger than the kinetic one, viz. the magnetic effects are dominant with respect to the hydrodynamic effects. It must be noticed that the integral scales are quite the same.

The anisotropy shown in figure 4.2 can be better appreciated through the PDF (see figure 4.3). In the radial direction the magnetic field follows more closely the Gaussian function than the velocity; in fact, considering that the Gaussian distribution has $Sk = 0$ skewness, the magnetic field skewness is higher than the velocity one (look at table 4.3). In order to study the anisotropy, the mean field direction must be considered; so defining the angle between the local vector field

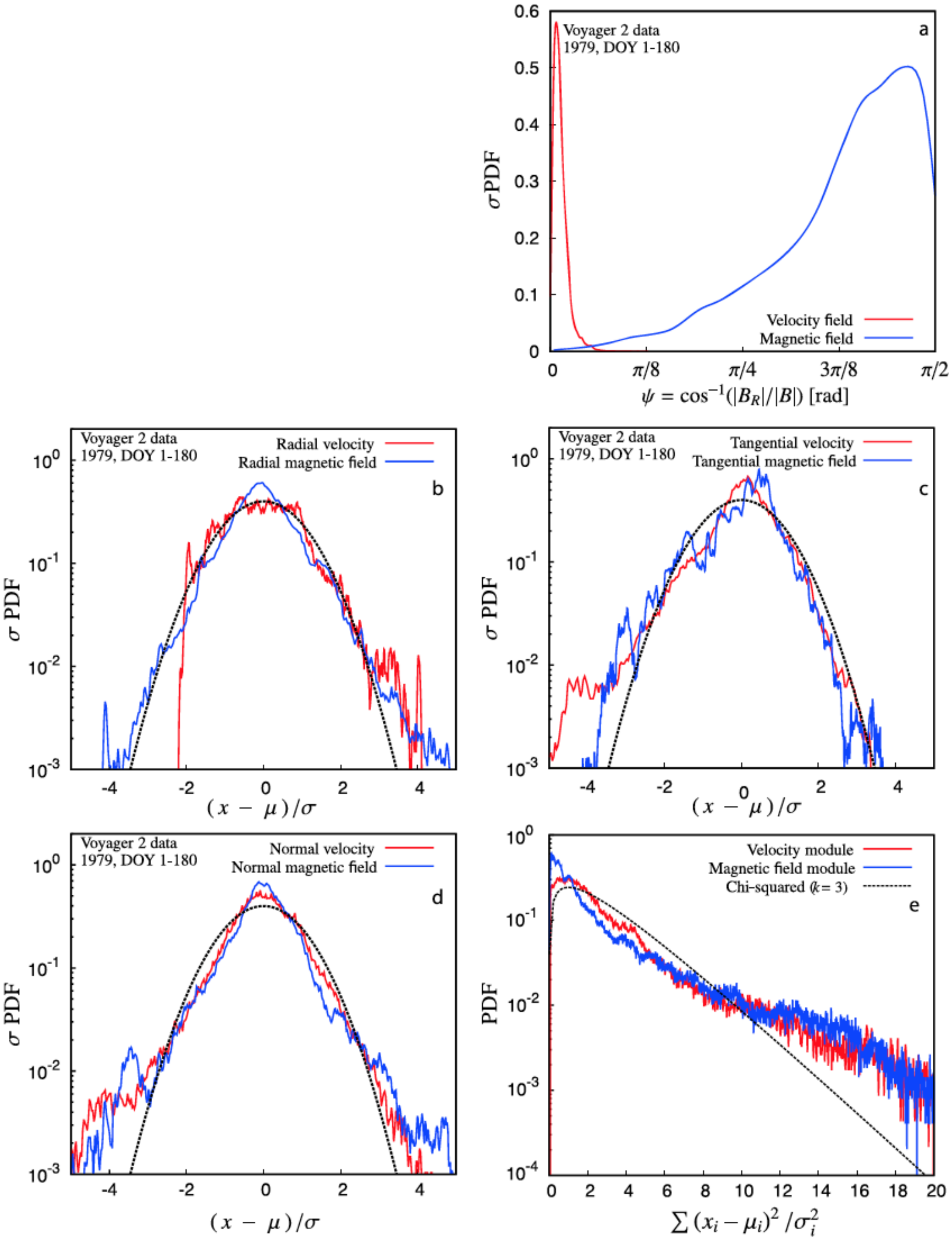

Figure 4.3: Normalized probability density function of both velocity and magnetic fields. (a) Ψ indicates the angle between the velocity (red) and the magnetic field (blue) directions. The velocity field is directed toward the radial direction ($\Psi \sim 0°$). The magnetic field is almost perpendicular to the velocity ($\Psi \sim 85° \div 105°$). (b) Radial, (c) tangential, (d) normal directions. (e) Comparison of velocity and magnetic field modules with respect to the chi-square distribution. Picture taken from Gallana et al. (2016).

Table 4.3: Intermittency and anisotropy are quantified through the statistical moments. μ is the first moment and indicates the mean value. σ is the second moment and indicates the variance. Sk is the third moment and indicates the Skewness. Ku is the fourth moment and indicates the Kurtosis. The modules of the fluctuations (first two raws) are computed using standard-normalized vector components ($|\delta\boldsymbol{\psi}|^2 = \sum_i (\psi_i - \mu_i)^2/\sigma_i^2$), then their statistical moments are dimensionless. Regarding the velocity components, the units of measure are $\mathrm{km\,s^{-1}}$ and $\mathrm{km^2\,s^{-2}}$ for mean and variance, respectively. Instead for the magnetic field the units are nT and nT^2. (Fraternale et al. 2016)

	μ	σ^2	Sk	Ku
$\lvert\delta\boldsymbol{U}\rvert^2$	3	10.47	2.40	10.27
$\lvert\delta\boldsymbol{B}\rvert^2$	2.48	17.41	3.17	14.90
U_R	454	1893	0.43	3.41
U_T	3.21	252.9	−0.99	7.35
U_N	0.51	250.3	−0.36	5.80
B_R	−0.04	0.173	0.53	6.71
B_T	0.06	0.85	−0.72	10.2
B_N	0.10	0.34	−0.24	7.65

and the radial direction as

$$\Psi_v = \cos^{-1}\left(\frac{|\boldsymbol{U_r}|}{\boldsymbol{U}}\right)$$
$$\Psi_b = \cos^{-1}\left(\frac{|\boldsymbol{B_r}|}{\boldsymbol{B}}\right)$$

the PDFs of these angles (see figure 4.3-a) display the perpendicular orientation of the velocity and magnetic field. Indeed, the former shows a sharpened distribution near the radial direction $\Psi \sim 0°$, while the magnetic field has a wider distribution with a peak between 85° and 105°. However, this analysis seems to confirm the Parker's spiral theory.

The intermittency can be appreciated looking at the PDFs of the field modules, in particular at figure 4.3-e, in which is shown the magnetic and plasma field is shown compared with the χ-square distributions. The χ-square distribution is the PDF of the normal distribution and is used as a test function. Qualitatively, one can state that the velocity field intermittence is lower than the one of the magnetic field, especially at the lower scales where the PDFs of the considered fields diverge from the PDF of χ-square. The skewness Sk quantifies the anisotropy as the kurtosis Ku quantifies the intermittency. In fact, the kurtosis describes the shape of the PDF throughout a measure of the tailedness. The normal distribution has $Ku = 3$, thus the PDFs with $Ku < 3$ are called *platykurtic* (thin tail) and those with $Ku > 3$ are called *leptokurtic* (fat tail). Both the plasma velocity and the magnetic field are leptokurtic, but the Ku related to the magnetic field is larger, in particular at the small scales.

Considering the values in table 4.2, the magnetic energy covers approximately 53% of the total energy, hence the Alfvén ratio averaged above all scales

$$r_A = \frac{E_v}{E_m},$$

is less than 1. Moreover, this imbalance tends to be less prominent at small scales; probably the increase of magnetic energy at the large scales is due to the waves generated by the PUIs, which initially have a ring distribution (Iovieno et al. 2016).

The normalized-cross helicity states the cross-correlation between the plasma velocity and the magnetic field. The SW moves away from the Sun as the correlation decreases. This is likely due to compressibility, velocity shears and density gradients, which can drive the turbulence toward a lower level of correlation, overwhelming the effect of the dynamic alignment.

4.3.2 Spectral analysis at 5 astronomical units

As explained in section 4.2.2, the characterisation of the inertial range of the MHD turbulence is strictly related to the definition of the energy spectrum

$$E(k) \propto k^{\alpha}$$

where α depends on the way the energy is transferred through the scales. Considering the K41 theory, vortices widely separated wavenumbers do not interact (Kolmogorv's concept of independence), thus $\alpha = -5/3$. When both the large and small scale eddies interact, the big vortices move in the opposite direction compared to the smaller ones and the energy cascade follows the IK theory, $\alpha = -3/2$.

For the reasons explained in section 4.2.2, only the one dimensional PSD can be computed, thus the frequencies must be converted to the radial wavenumbers $k_{\|}$. Looking at table 4.2, the SW is super-Alfvénic and supersonic, hence the Taylor's hypothesis can be applied.

Table 4.4: Spectral index of both velocity and magnetic field (also expressed in Alfvén units) computed in the four frequency decades. In the higher frequency range the peak has been not considered. (Fraternale et al. 2016)

f range	$\|\boldsymbol{U}\|$	$\|\boldsymbol{B}\|$	$\|\boldsymbol{b}\|$
$10^{-6} \div 10^{-5}$	-1.85	-1.23	-1.38
$10^{-5} \div 10^{-4}$	-1.72	-1.75	-1.63
$10^{-4} \div 10^{-3}$	-1.26	-1.75	-1.63
$10^{-3} \div 10^{-2}$	-1.35	-1.93	-1.80

The decades examined are four ($10^{-6} \div 10^{-2}$) and the aim is to identify the extent of the inertial range. Fraternale et al. (2016) studied both plasma and magnetic field spectral index in this frequencies range. Averaging on the whole domain, the velocity spectral index is approximately -1.5, the one predicted by Iroshnikov-Kraichnan. It must be considered that the exponent is not constant throughout the frequency range; in particular at large scales the value is high (-1.85), but it decreases below -1.35 after $f = 2 \times 10^{-3}$ Hz (see table 4.4 for more details about index values in the four decades). When the flow is characterised by a strong mean value with respect to the fluctuations, the turbulence is called weak. This is the assumption done by IK and the value $-3/2$ is recovered. Instead when the turbulence is strong, the spectral index follows the K41 value $-5/3$. It is worth highlighting the peak in figure 4.4-a, which is associated to the data acquisition frequency. As summarised in table 4.5 the radial velocity is higher than the other two components at large scales. At $f \sim 4 \times 10^{-4}$ Hz the PSD change behaviour, the radial component is flatter than the tangential and normal velocity. Moreover, at low frequencies the kinetic energy shows an exponent of $\alpha \sim -1.67$, which corresponds to that predicted by the K41 theory. At high frequencies the spectral index decreases at $\alpha \sim -1.33$. The fact that the K41 law has been uncovered does not mean that the turbulence is strong and isotropic. Indeed, more phenomelogies can interfere with this statement, first of all the intrinsic anisotropy of the MHD. Either to confirm or to exclude the validity of the K41, the eddy turnover time must be evaluated when the inertial cascade begins. Gallana et al. (2016) did it in their work and find that the eddy turnover time is as large as 5 times

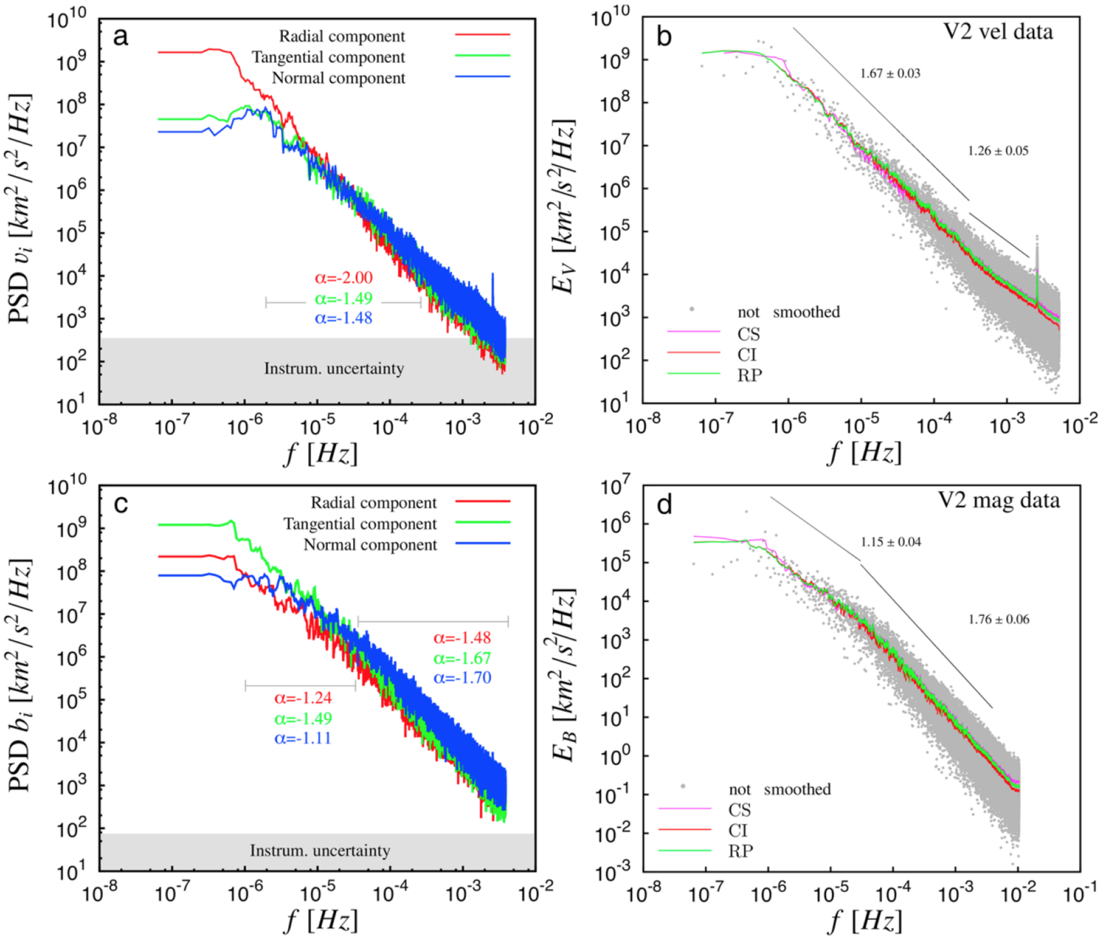

Figure 4.4: Data from V2, 1979 DOY 1-180. The spectra of both B and U components are computed using the correlation method with linear interpolation. RTN reference frame used. (a) Spectra of the velocity components; in the low-frequency realm the radial component is dominant, but in the high-frequency domain the normal and tangential fluctuations components are larger. (b) Spectrum of the kinetic energy behaves as predicted by Kolmogorov in the low-frequency domain and then it becomes flatter. (c) Spectra of the magnetic field in which the tangential component is dominant at low frequencies, but at high frequencies it becomes steeper. (d) Spectrum of the magnetic energy, which is characterised by index $\alpha \sim 1$ in the low frequencies. There is a spectral break at $f \sim 10^{-5}$ Hz and then the curve becomes steeper. It is to be noted that both kinetic and magnetic energy spectra are computed using three different techniques: compressed sensing (CS), correlation spectrum with linear interpolation (CI) and Rubycki&Press maximum likelihood recovery. The grey curves are the unsmoothed spectra. (Gallana et al. 2016)

Table 4.5: Spectral index values for velocity, magnetic field and energy components. The magnetic field is also expressed in Alfvén units. (Gallana et al. 2016)

f range	U_R	U_T	U_N	E_v
$10^{-6} \div 4 \times 10^{-4}$	-2.00	-1.49	-1.48	-1.67
$4 \times 10^{-4} \div 5 \times 10^{-3}$	-1.18	-1.26	-1.48	-1.33
f range	B_R	B_T	B_N	E_B
$10^{-6} \div 3 \times 10^{-5}$	-1.06	-1.46	-0.85	-1.21
$3 \times 10^{-5} \div 5 \times 10^{-3}$	-1.56	-1.72	-1.77	-1.72
f range	b_R	b_T	b_N	E_b
$10^{-6} \div 3 \times 10^{-5}$	-1.24	-1.49	-1.11	-1.34
$3 \times 10^{-5} \div 5 \times 10^{-3}$	-1.48	-1.67	-1.70	-1.65

the age of the plasma. Hence, the spectrum cannot refer to active turbulence. Moreover, through the figure 4.4-a it can be stated that at low frequencies the radial fluctuations, which are associated to the SW variation near the Sun, dominate. It must be noted that the flattening can be due to the level of noise.

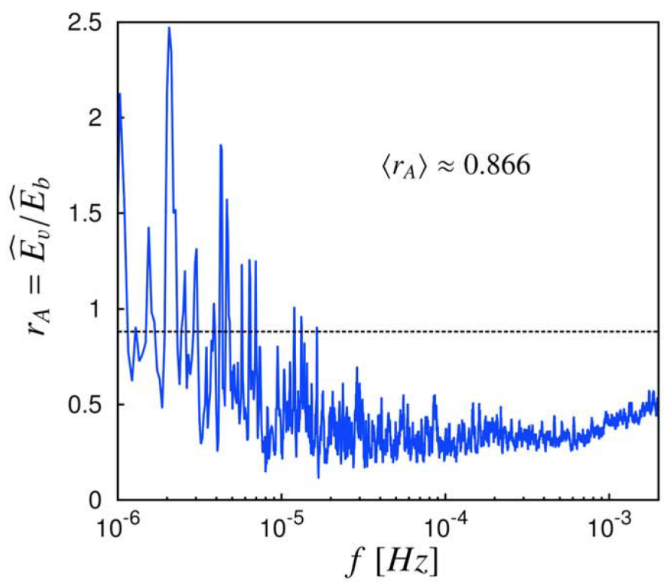

Figure 4.5: Spectral analysis of the Alfvén ratio. There is a gradual reduction of the ratio value as the frequency increases. All frequencies higher than $f \sim 10^{-5}$ Hz show $r_a < 0.5$. The dotted line represents the Alfvén ratio computed using the averaged magnetic and kinetic energy. (Gallana et al. 2016)

The magnetic field presents on average a higher spectral index than the velocity, in fact in the frequency range $f \sim 10^{-5} \div 10^{-2}$Hz the slope is -1.75. The magnetic field spectrum has the same breakpoint as the velocity one, but it is located at frequency $f \sim 5 \times 10^{-5}$ Hz. Looking at figure 4.4-c, it is clear that the tangential component dominates in the low frequency range, remembering that it is associated with the magnetic field strength variations which can be due to shocks or current sheets (as in the Parker's spiral). Another explanation of the steeper trend at the high scales can be the Alfvén waves generated at the solar corona. The magnetic energy has ~ -1.65 slope at low frequency, as predicted by Kolmogorov. At high frequency the index decreases up to -1.34.

The Alfvén ratio has been defined at the end of the previous section and expresses the imbalance between the kinetic and the magnetic energy. The Fourier transformation of r_A allows to estimate the extent of the inertial range. Normally in the searched range $r_A < 1$, therefore looking at figure 4.5 one can conclude that the inertial range starts at $f \sim 5 \times 10^{-5}$ Hz. The lowest limit of this range is set at $f \sim 5 \times 10^{-3}$ Hz because of the low reliability of high frequency data.

4.4 Turbulence in the heliosheath (IHS and OHS)

In this last section, the characteristics of the turbulence in the heliosheath, both inner and outer, are discussed. It is worth highlighting that the OHS is also called LISM; in particular, the very local interstellar medium (VLISM) is the nearest region of the LISM that surrounds the Sun and it is affected by the heliospheric processes (Zhao et al. 2020). The V1 and V2 crossed the HP in 2012 (121.5 au) and 2018 (119 au), respectively (ibid. and reference within). The HP width is about 0.3 au (Fraternale et al. 2019a).

Data used further on come from both V1 and V2; they are provided in the RTN reference system, but in most cases it is better to rotate the latter to the mean field coordinates. Since the background magnetic field is nearly orthogonal to the SW flow, the components of the field are $B_{\parallel} \sim B_T$, $B_{\perp 1} \sim B_N$ and $B_{\perp 2} \sim B_R$ (where $B_{\parallel}$ is aligned with the background mean field $\boldsymbol{B_0}$).

Most of the data get lost due to tracking problems, in the IHS the 72% of 48 s data are missing and the average frequency of the largest gap is around $f \sim 2.4 \times 10^{-5}$ Hz. The level of noise 0.006 nT must be considered, moreover there are errors due to calibration (± 0.02 nT for V1 and ± 0.03 nT for V2), and thus the total uncertainty is about 0.1 nT. The level of noise and its distribution is actually unknown, hence the white noise model is assumed but it is likely that the real noisy level is lower.

The change of reference system is done because the Plasma Science instrument is not operative and the bulk SW velocity is computed through other kinds of analysis. Analysing the velocity spectra is impossible, therefore the background magnetic field reference system is the best choice.

The magnetic field is studied at different distances from the Sun. The V1 periods considered (in the IHS) present almost the same polarity (northern) save for the last period (see figure 4.6). The time ranges are called A1,B1,C1 and D1. The Taylor's hypothesis is not always valid during these periods, so attention must be paid when frequencies are considered in the plasma or in the spacecraft frame.

The V2 probe reveals different fluxes of the energetic particles (ENA), this is probably due to the fact that V2 is close to the boundary between the sector (SHS) and the unipolar region (UHS; see figure 3.5). Different periods are considered, both in the SHS and in the UHS, and they are called SHS1, UHS1, UHS2 and SHS2 as reported in figure 4.6.

In the LISM four periods have been analysed, called L1, L2, L3 and L4. The first and third periods refer to *disturbed* intervals. The second and fourth periods are related to *quiet* intervals [7]. Data available in the LISM further decrease, 48 s alone does not allow to study the statistic features of the SW, therefore there are two possible ways: using some recovery methods or using daily averaged data.

[7] The quiet interval is a region characterised by shocks and disturbances.

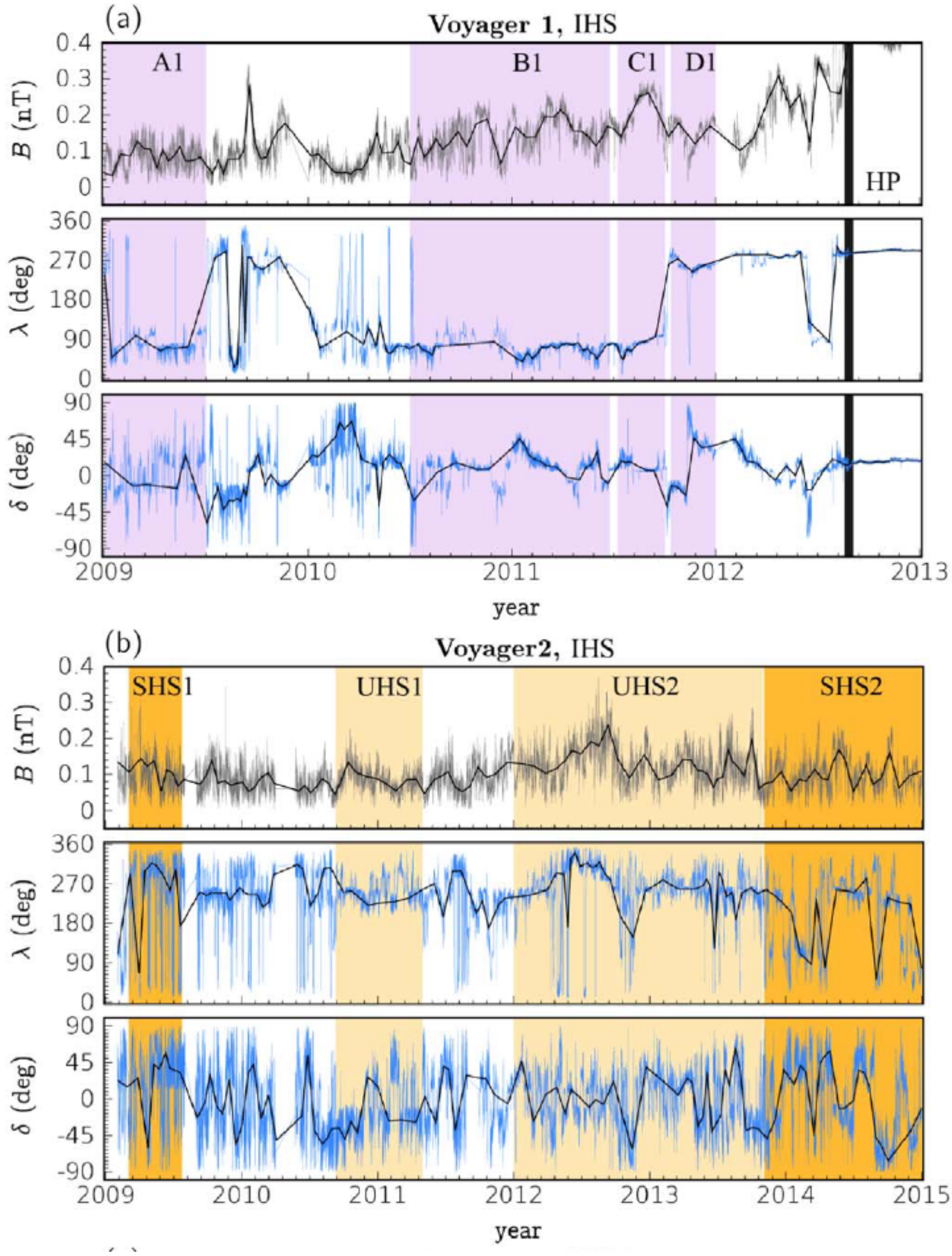

Figure 4.6: Data sets analysed in the IHS. In the top panel the magnetic field magnitude $B = |\boldsymbol{B}|$, in the middle panel the azimuthal angle $\lambda = \tan^{-1}(B_T/B_R)$ and in the bottom panel the elevation angle $\delta = \sin^{-1}(B_N/B)$. All of them in function of the time. Data points with $|B_{R,N,T}| < 0.03\,\mathrm{nT}$ are neglected in the λ, δ computation.(a) V1 and (b) V2 periods considered. (Fraternale et al. 2019a)

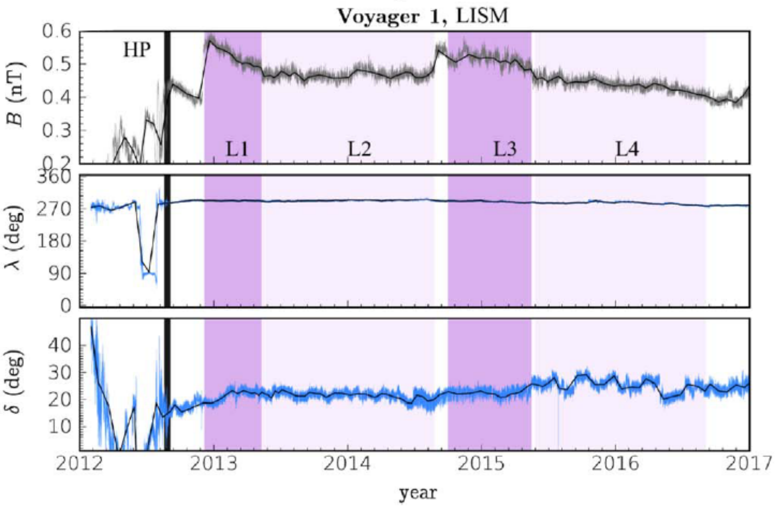

Figure 4.7: Data sets analysed in the LISM, provided by V1. In the top panel the magnetic field magnitude, in the middle one the azimuth angle and in the bottom one the elevation angle. (Fraternale et al. 2019a)

After crossing the TS, the flow results to be compressible both in the IHS and the VLISM. There is the need to quantify the spectral compressibility and this is done by using

$$C(f) = \frac{P(|\boldsymbol{B}|)}{E_m} \tag{4.17}$$

where $P(|\boldsymbol{B}|)$ is the PSD of the magnetic field magnitude and $E_m(f) = \mathrm{tr}(P(|\boldsymbol{B}|)) = P(B_{\parallel}) + P(B_{\perp 1}) + P(B_{\perp 2})$ is the trace of the PSD tensor, which is a proxy for the magnetic energy.

Not all the fluctuations are turbulence, the instruments cannot distinguish between waves and fluctuations due to non-linear interaction, hence the *causality condition* must be considered. A fluctuation experiences one eddy turnover in a period $t = \pi l(\delta U)^{-1}$, where l is the length scale and δU is the velocity scale. Assuming the frozen-in condition as valid, the fluctuation is convected by the wind at $d = U_{SW}t$ distance and the SC measures it at $f_e \sim \pi U_{SW}^2(d\ \delta U)^{-1}$ frequency. The distance d can be rewritten as $d = r_{SC} - r_{source}$, where r_{SC} is the SC position and r_{source} is the distance of the fluctuation source with respect to the origin of the reference system. Considering that the fluctuation moves as an Alfvén wave, $\delta U \sim c_a$ and the frequency limit is

$$f_e \sim \frac{\pi U_{SW}^2}{c_a(r_{SC} - r_{source})} \tag{4.18}$$

frequencies $f < f_e$ do not satisfy the causality condition, hence they represent waves older than the solar wind. Therefore, these waves come from the outer space. In the previous section the Sun has been considered as source location, $r_{source} = 0\,\mathrm{au}$, but in the IHS the best choice is the TS, $r_{source} = 84\,\mathrm{au}$, as confirmed by in situ measurements.

4.4.1 Spectral analysis in the inner heliosheath

The two probes (V1 and V2) revealed different features, hence each analysis is done separately.

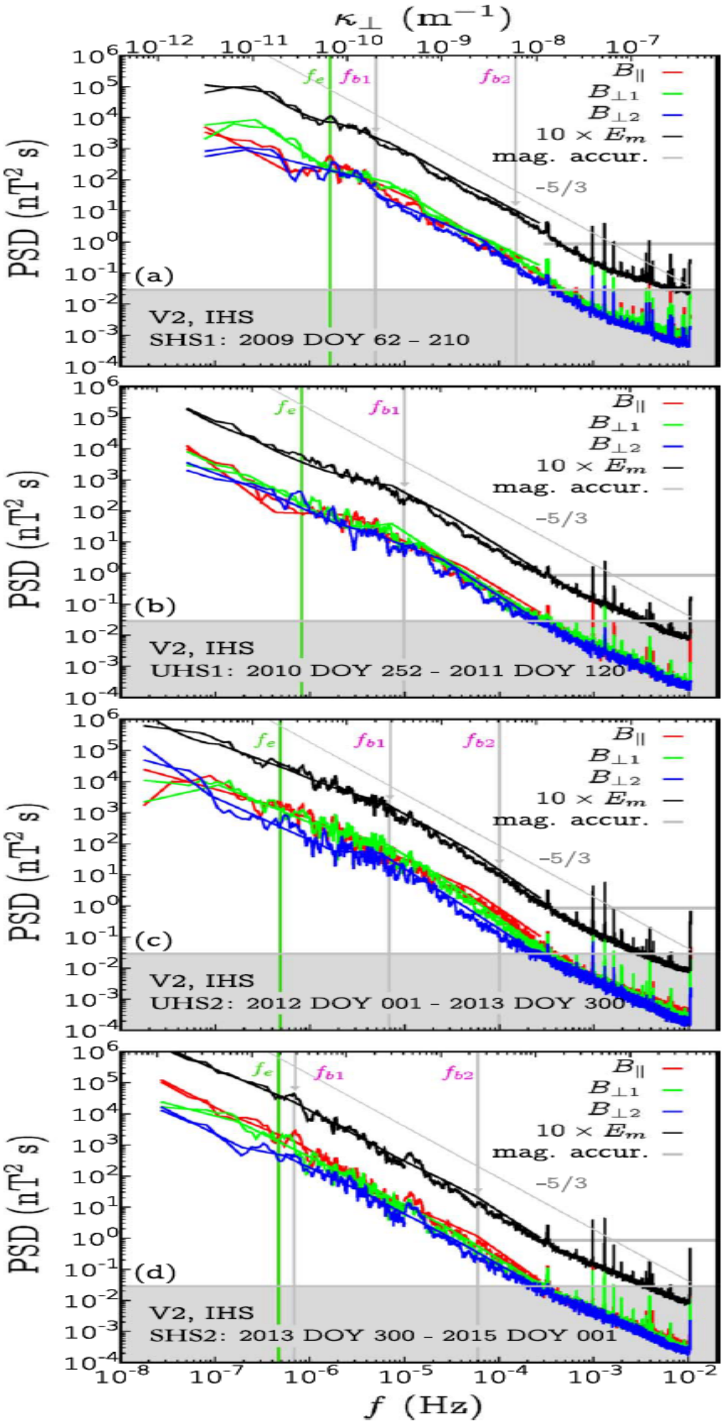

Figure 4.8: V2 data. Power spectral density of magnetic field fluctuation components. The magnetic energy is magnified by a factor of 10. The PSD end at the Nyquist frequency for the 48 s resolution. The grey band represents the uncertainty region. (Fraternale et al. 2019a)

Voyager 2

The Voyager 2 collected 48 s average data in the range frequency $10^{-8} < f < 10^{-2}$ Hz, which includes the energy injection, the inertial cascade and the beginning of the kinetic regime (it starts at the ion cyclotron frequency of the order of mHz).

As previously said, the noise level is assumed equal to the white noise of 0.03 nT amplitude, which corresponds to a power level of $P_{noise} = 0.029\,\mathrm{nT^2s}$. Considering also the errors, the power level increases at value of $P_{noise} = 0.086\,\mathrm{nT^2s}$. This region includes frequencies below 5×10^{-4} Hz, which present a spectral break and the PSD show a flatter behaviour (see figure 4.8). Despite the noise, some information can be extrapolated, indeed the flattening in this region does not correspond to white noise and the spectral slope is around -1. However, one can appreciate the anisotropy, but for the physical behaviour is needed a better data resolution. It is worth highlighting that the observed spikes in the high-frequency range are likely related to the harmonic of the sampling rate and to the instruments interference.

Table 4.6: Average quantities from data provided by V2.

Voyager 2	Quantity	SHS1	UHS1	UHS2	SHS2
r_{SC}[au]	SC distance	89.0	94.1	100.2	104.9
U_{SW}[km s^{-1}]	SW velocity	157	151	154	153
B_0[nT]	Background magnetic field	0.062	0.072	0.090	0.030
β_p	Ions plasma beta	0.54	0.46	0.54	1.00
$\beta_{p1\mathrm{keV}}$	PUIs beta parameter	19.6	24.3	22.2	45.0
c_a[km s^{-1}]	Alfvén velocity	63.4	59.2	63.9	51.6
r_{ip}[km]	Ions inertial radius	6852	7186	5214	5357
r_{cp}[km]	Gyroradius	3502	3301	2485	3038
$f_{ip,SC}$[mHz]	Ions plasma frequency	11.5	10.5	14.8	14.3
$f_{cp,SC}$[mHz]	Ions cyclotron frequency	22.4	22.8	30.9	25.2
f_e[Hz]	One-eddy turnover frequency	1.6×10^{-6}	8×10^{-7}	4×10^{-7}	4.5×10^{-7}

Looking at the values reported in table 4.6, the ratio $c_a/U_{SW} \sim 0.3$ and considering that $U_{SC}/U_{SW} \sim 0.1$ the Taylor's hypothesis can be used ($V_{SC2} \sim 15\,\mathrm{km\,s^{-1}}$). The background magnetic field is 90° tilted respect to the plasma flow, hence it is possible to convert the SC frequency in the perpendicular wavenumber $k_\perp \sim 2\pi f_{SC2}(U_{SW})^{-1}$. In the PSD figure both the wavenumber and the frequency are reported.

Averaged data in table 4.6 are intriguing because they show that the cyclotron frequencies fall in the high-frequency range. This confirms the statement above: the spectra include the beginning of the kinetic regime.

The flatness of the PSD is not only due to the noise, indeed the PUIs density in the heliosheath in the amount of 20% considerably affects data.

The *energy injection* (EI) regime is identified by the presence of a spectral break f_{b1}, the magnetic energy follow the f^{-1} decay. In particular the spectral index is between 0.7 and 1.13 in the sectors considered (Fraternale et al. 2019a). Figure 4.8 clearly shows that this spectral break is not constant, but it depends on distance and on the kind of region (SHS or UHS). In the UHS the EI limit has a larger threshold frequency than in the SHS; moreover, moving away from the Sun, f_{b1} reaches lower values. This is supported by the work of Fraternale et al. (2019b), in which the spectral behaviour of the SW in the sectored region at 106 au is studied. In this work the EI limit reside at $f \sim 7 \times 10^{-7}$ Hz, while in the periods here considered the value for the SHS are 5×10^{-6} Hz and 7×10^{-7} Hz. This scaling has also been observed in the SW upstream the TS and

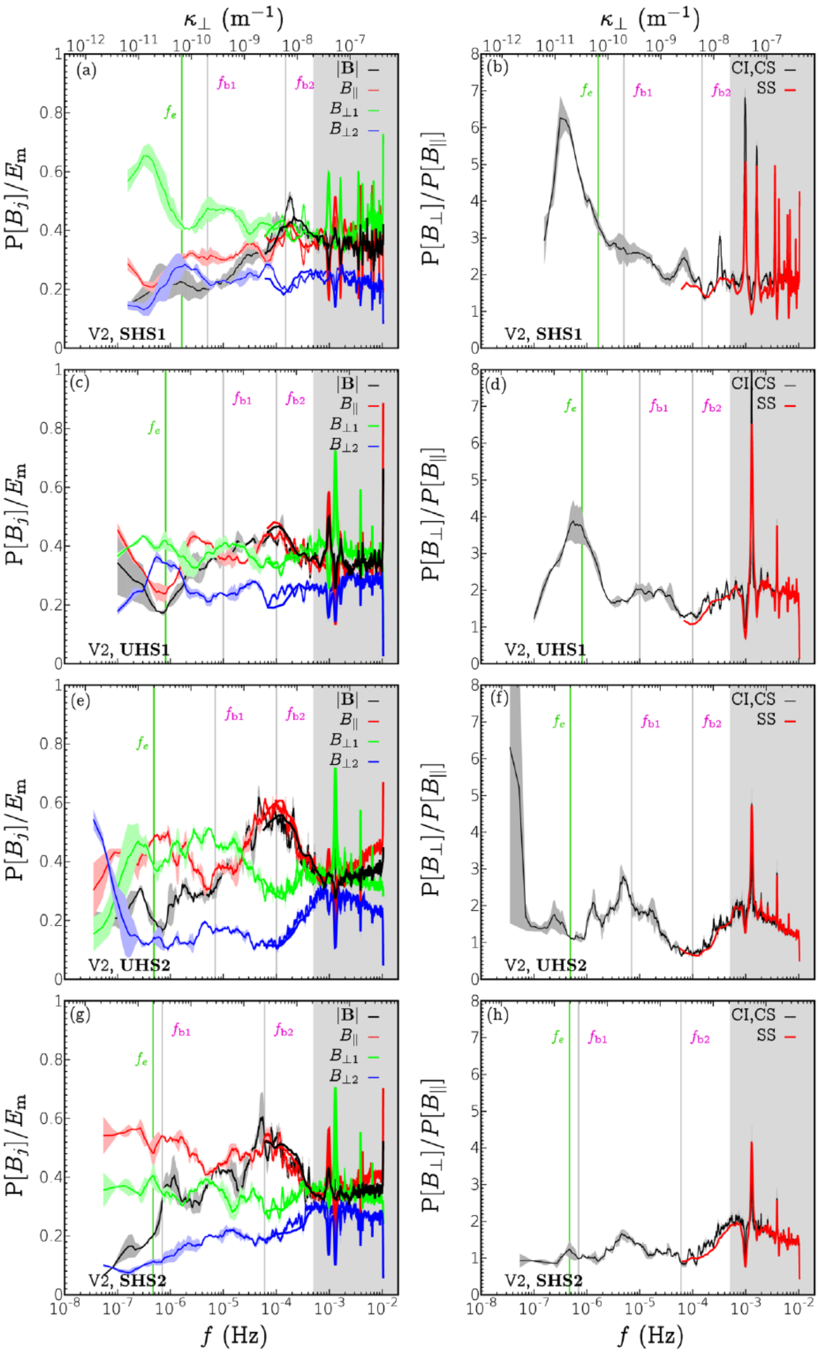

Figure 4.9: Spectral variance anisotropy and compressibility in the IHS (for all periods considered) of V2 data. On the left, variance anisotropy computed as $P[B_j]/E_m$, where $B_j = \{B_\parallel, B_{\perp 1}, B_{\perp 2}\}$. In the same graphs the compressibility $P[|B|]/E_m$ (black curve). On the right, the ratio between the perpendicular component $P[B_\perp] = P[B_{\perp 1}] + P[B_{\perp 2}]$ and the parallel component $P[B_\parallel]$ computed by different methods. CI is the correlation method with linear data interpolation. CS is the compressed sensing spectral estimation. SS is the gap-free subsets. The grey bands in all the pictures represent the uncertainty range and the peaks are due to instrumental interference. (Fraternale et al. 2019a)

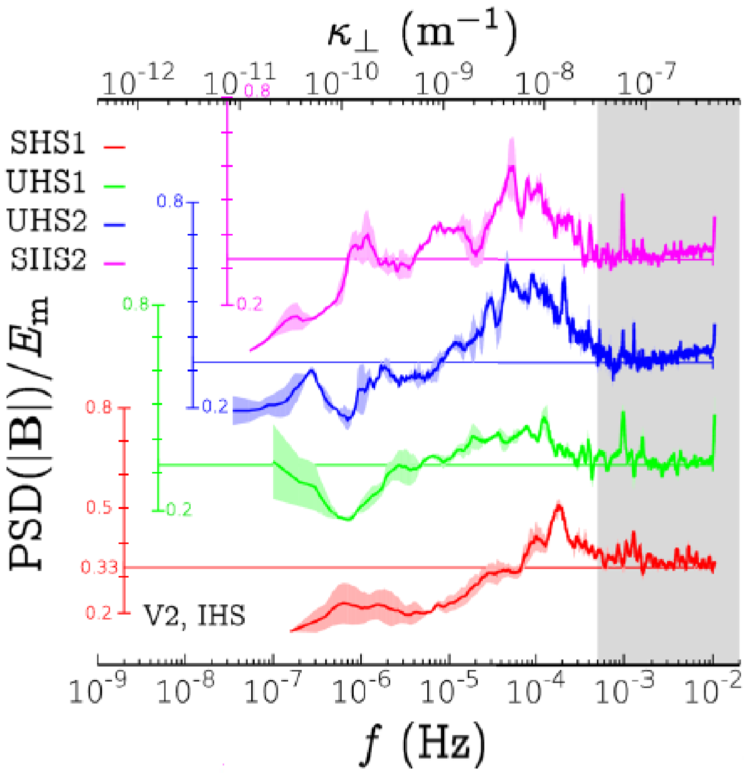

Figure 4.10: V2 spectral compressibility in the IHS. The colored areas represent the variability between different methods. The grey band is the uncertainty region. (Fraternale et al. 2019a)

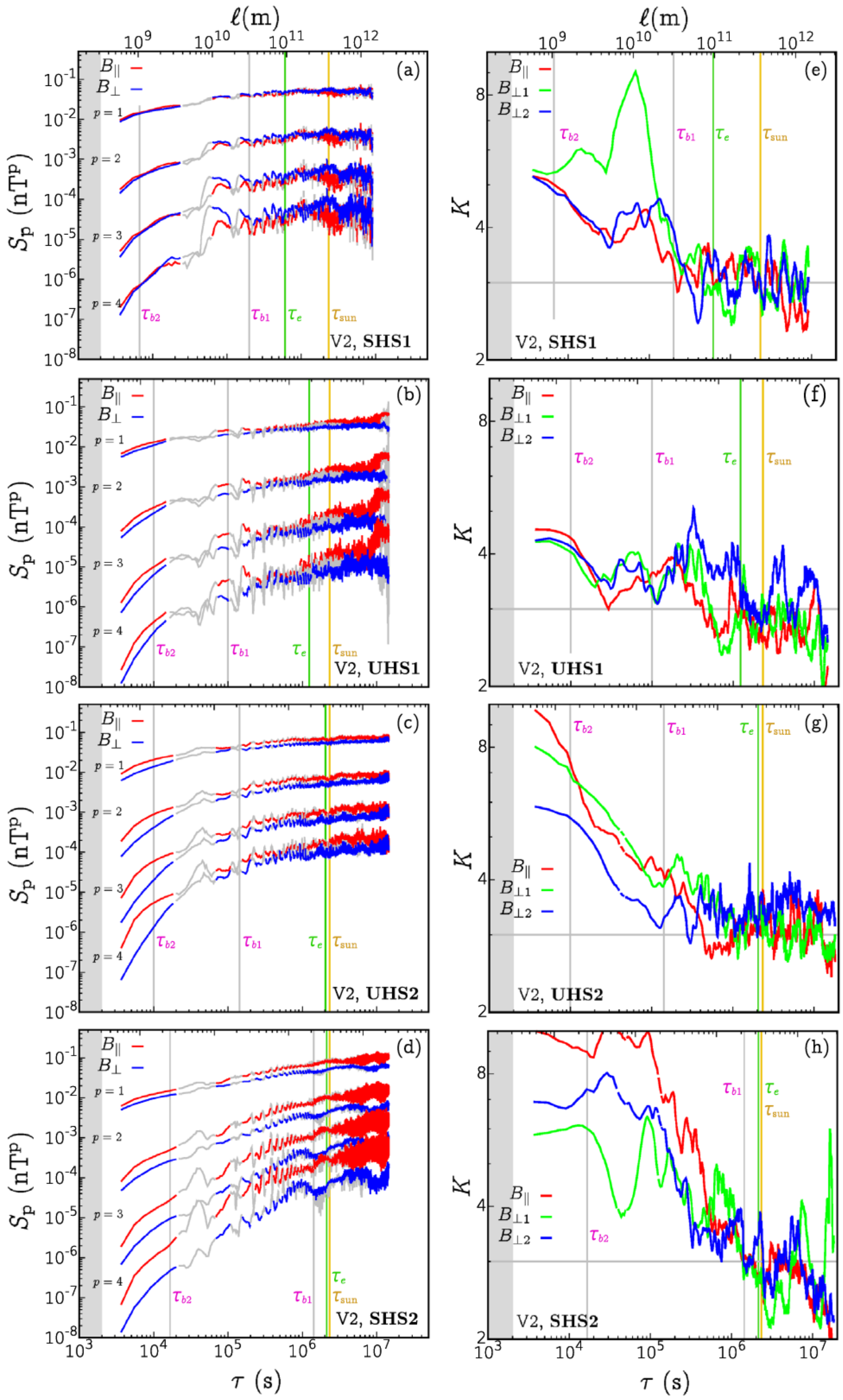

Figure 4.11: On the left, structure funcions of the $B_{\parallel}$ fluctuations (red lines), $S_{p,\parallel}$, and $B_{\perp}$ ones (blue lines) $S_{p,\perp} = (S_{p,\perp 1} + S_{p,\perp 2})/2$. On the right, Kurtosis of the magnetic field increments showing the intermittent behaviour. (Fraternale et al. 2019a)

it is related with the fluctuations Alfvénicity. In the fast wind stream the large-scale Alfvén waves do not experience enough non-linear interaction, thus the turbulent cascade does not originate. The energy of this wave forms a reservoir for the turbulent cascade at lower scale. The UHS are initially mor Alfvénic than the SHS, therefore the f_{b1}-location increases. Besides, considering turbulent structures larger than the outer scale is not reasonable; in this case the outer scale is given by the IHS for the UHS and by the sector width in the SHS. The Sun's rotation works as forcing on the system, at a frequency of $f \sim 4.5 \times 10^{-7}$ Hz, which determines the nominal width of the SHS (2 au).

The spectral break does not follow the same rules in the magnetic field component spectra, indeed the f_{b1} in the $B_\perp$ fluctuations occurs at higher frequencies than in the $B_\parallel$ ones.

The spectral break cannot be evaluated accurately through figure 4.8, but it is better recognized in the structure function diagram in which the curves follows a flatter trend.

Looking at figure 4.10, the compressibility is small ($C \sim 0.2$) in all the sectors considered. Fraternale et al. (2019b) show that in the sector region there is high energy in the parallel fluctuations $\delta B_\parallel$ which is not due to the compressibility, but to the polarity changes.

A recent study demonstrates that the turbulent cascade cannot exist at scales where the fluctuations intensity, defined as

$$I_j(\tau) = \langle \left| \frac{\delta B_j}{B_0} \right| \rangle \quad j = (\parallel, \perp_1, \perp_2),$$

is less then 1. In this case the K41 law cannot subsist and the spectra power law is $1/f$. The Kurtosis values at large scales are about 3, thus there is no intermittency.

The *inertial cascade* (IC) is the range between the EI and the kinetic realm, hence it can be recognised in the frequency extension denoted by $f_{b1} < f < 10^{-3}$ Hz. In this range there are two types of scales of the magnetic fluctuations divided by a spectral *knee* at f_{b2}. The two subranges are called IC1 and IC2. It is worth noting that in the period UHS1 the second knee is absent. However, the different spectral behaviour is more evident in the parallel component $B_\parallel$ than in the perpendicular one $B_\perp$.

Fraternale et al. (2019a) found in the IC1 of the sectored regions, a spectral slope of $\alpha_{IC1} \sim -1.6$ which is consistent with the GS95 theory. In the following work, Fraternale et al. (2019b) found a slightly different slope index $\alpha_{IC1} \sim -1.5$, more similar to the IK theory. Anyway, both the IK and GS95 theories do not take into account the compressibility, which plays an important role in the IHS especially near the HP. During the unipolar periods the spectral slope is steeper, with an exponent index about -1.75. Moreover, during the UHS1 period the second knee is absent while in the USH2 spectrum the second knee exists, but the IC1 is less extended than the sectored regions.

Table 4.7: Frequencies and spectral slopes in the energy injection range and in the splitted inertial range.

Voyager 2	SHS1	UHS1	UHS2	SHS2
f_{b1}[Hz]	5×10^{-6}	10^{-5}	7×10^{-6}	7×10^{-7}
f_{b2}[Hz]	2×10^{-4}	...	10^{-4}	7×10^{-5}
α_{EI}	-0.98 ± 0.10	-1.10 ± 0.03	-1.18 ± 0.05	-1.25 ± 0.13
α_{IC1}	-1.64 ± 0.01	-1.78 ± 0.06	-1.78 ± 0.13	-1.58 ± 0.02
α_{IC2}	-1.84 ± 0.04	...	-2.07 ± 0.04	$-1.86 \pm 0{,}07$

The IC2 range shows a steeper spectrum of the magnetic energy E_m, where the index reaches the value of $\alpha_{IC2} \sim -2$. Comparing the second knee frequency f_{b2} with both the ions plasma frequencies $f_{ip,SC}$ and the ions cyclotron frequency $f_{cp,SC}$, it is evident that the second spectral break is still within the MHD inertial range.

The variance anisotropy is shown in figure 4.9. In the EI range the major role is played by the transverse fluctuations $B_{\perp 1}$, indeed the ratio $P[B_{\perp 1}]/P[B_{\parallel}] \sim 2$ at the beginning of the IC. At f_{b2} the ratio mentioned decreases to values of about 1, hence the parallel fluctuations account for $\sim 50\%$ of the energy. However, approaching the HP the parallel fluctuations become more important.

The compressibility (black curve in figure 4.9 a-g) is about 0.2 in the EI regime, then it increases in the IC1 reaching the maximum value 0.6 at the frequency f_{b2}.

The intermittent behaviour can be observed through the Kurtosis (figure 4.11 e-h). In the EI range the Kurtosis value is approximately 3, which means that the PDF is Gaussian. This result leads to the presence of a self-similar solution in the EI range, thus the energy injection is not intermittent. In the inertial range the intermittency grows and the Kurtosis reaches value up to 10.

Looking at the structure functions represented in figure 4.11 a-d, a flatter trend at large scales can be recognised. This is the EI range and the flattening means that the fluctuations at these scales are not correlated, viz. the non-linear effects are not important. This consideration confirms that the EI range is the effect of the solar rotation. The ESS has been used in the inertial range, both for the perpendicular and parallel fluctuations, and a defined power-law has been found. Moreover, the structure functions allow to accurately define the IC1 and IC2 limit.

From these results, the decreasing trend of the intermittency and of the compressibility at high frequencies can be related. This relation occurs near the kinetic regime and it can be due to a physical process or data noise, but more investigation is needed (Fraternale et al. 2019a).

Voyager 1

Remembering the Doppler-shift relation (eq 4.5), it is possible to recover the vector wavenumber in the direction of the relative wind flow, only if the Taylor's hypothesis ($f_{PL} \ll |\boldsymbol{k} \cdot \boldsymbol{U_{rel}}|(2\pi)^{-1}$) is valid. In the selected periods this assumption does not hold, because the velocity of the spacecraft is $V_{SC1} \sim 17\,\mathrm{km\,s^{-1}}$. Therefore the figures show only the frequencies at the spacecraft reference frame.

Table 4.8: Average quantities from data provided by V1. The PLS subsystem does not work, hence data are taken from Fraternale et al. (2019a).

Voyager 1	Quantity	A1	B1	C1	D1
r_{SC}[au]	SC distance	109.5	115.7	117.9	118.8
U_{SW}[$\mathrm{km\,s^{-1}}$]	SW velocity	65	40	40	40
B_0[nT]	Background magnetic field	0.083	0.132	0.195	0.124
$f_{cp,SC}$[mHz]	Ions cyclotron frequency	1.32	2.14	3.10	0.81

The Canberra antennas are the only ones that can operate the telemetry, thus the V1 data present the same issues of the twin. Consequently, the level of noise is set in the same way, a white noise is considered. Moreover, the Plasma Science instrument (PLS) does not work, then the bulk velocity is recovered by a Compton-getting analysis (ibid. and reference within). In table 4.8 the average quantities available are reported; as one can note the one-eddy turnover time, the beta parameters, the Alfvén velocity and both the ions plasma and Larmor frequency are missing. This lack of information leads to the impossibility to distinguish the waves origin, hence the different ranges of the cascade are challenging to find.

The spectral analysis shows that there is a single spectral break $f_{b1} \sim 10^{-5}\,\mathrm{Hz}$ in the range $10^{-8} < f < 10^{-2}\,\mathrm{Hz}$ considered (see figure 4.12). At low frequencies the spectral slope is around

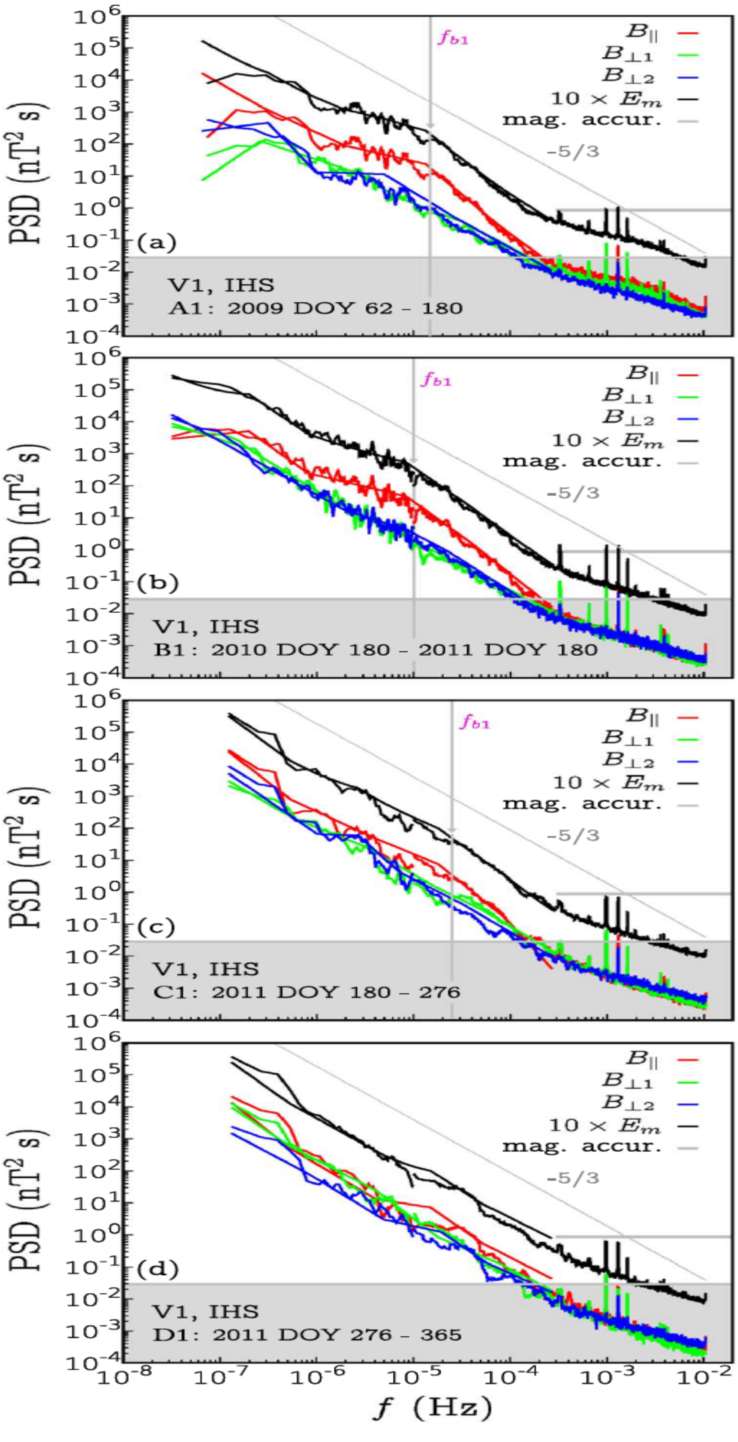

Figure 4.12: V1 data. Power spectral density of magnetic field fluctuation components. The magnetic energy is magnified by a factor of 10. The PSD end at the Nyquist frequency for the 48 s resolution. Differently from V2 data, the second spectral knee is absent. The grey band represents the uncertainty region. (Fraternale et al. 2019a)

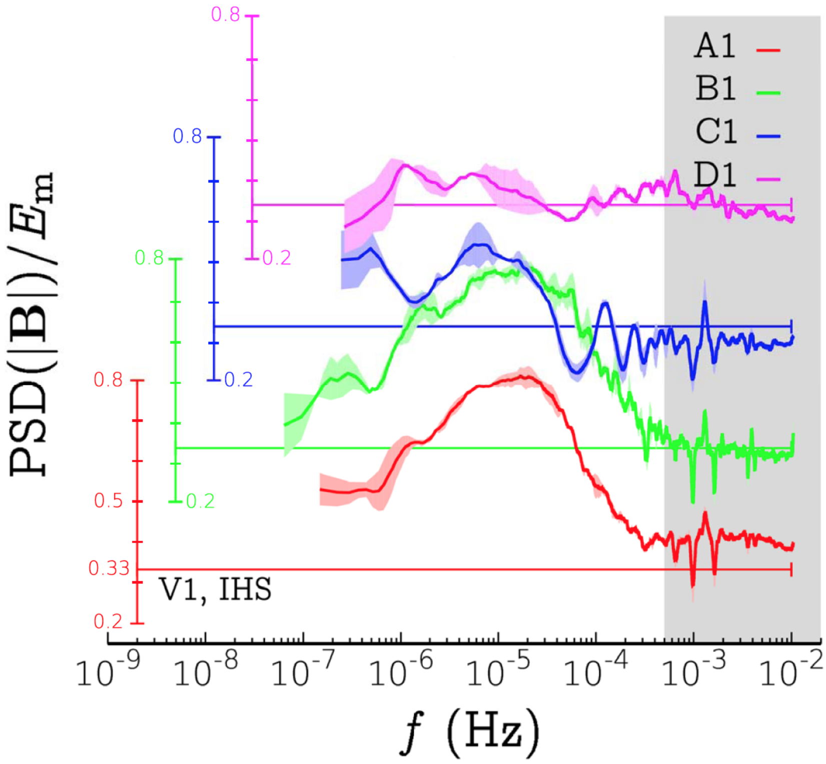

Figure 4.13: V1 spectral compressibility in the IHS. The colored areas represent the variability between different methods. The grey band is the uncertainty region. (Fraternale et al. 2019a)

Table 4.9: V1 magnetic field properties in the IHS.

Voyager 1	A1	B1	C1	D1
f_{b1}[Hz]	2×10^{-5}	10^{-5}	2×10^{-5}	...
α_1	-1.17 ± 0.09	-1.31 ± 0.15	-1.60 ± 0.18	...
α_2	-2.25 ± 0.12	-2.31 ± 0.04	-2.23 ± 0.09	-1.72 ± 0.05

$\alpha_1 \sim -1.2$. After the knee the spectrum is steeper and the index reaches value of $\alpha_2 \sim -2.3$ (more details in table 4.9). Approaching the HP the spectral break becomes weaker, such that in the last period (D1) the knee is absent. This is probably imputable to the physical meaning of the break. As matter of fact, looking at figure 4.13, the compressibility reaches its maximum at f_{b1}, which means that the spectral break is associated to the compressible modes.

However, higher values of compressibility ($C \sim 0.6$) are found in the V1 data with respect to the V2 ones. The parallel component of the magnetic field largely contributes to the fluctuating energy, indeed the ratio $P[B_\perp]/P[B_\parallel]$ is less than 1 in the central range. Another proof of this statement is provided by the spectral compressibility $P[|\boldsymbol{B}|]/E_m$ which amount to the maximum at f_{b1}.

The peak of anisotropy occurs for f_{b1}, but also in the grey region the anisotropy is high. These last decades cannot be physically evaluated because of the noise. In the D1 period the anisotropy is low, the compressibility decreases at value of $C \sim 0.4$ and the spectral break does not exist.

Differently from the fluctuations detected by V2, the V1 ones appears intermittent for all

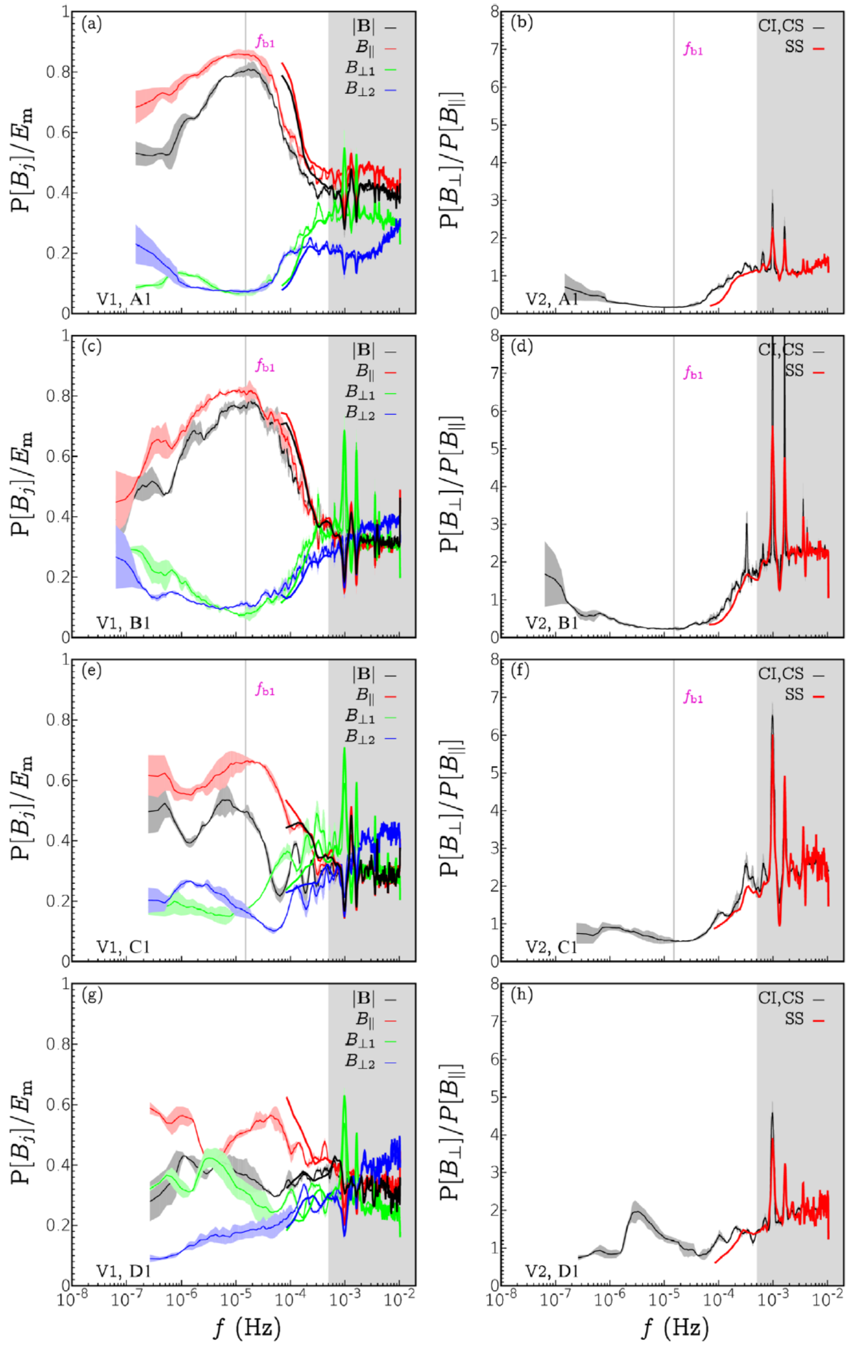

Figure 4.14: Spectral variance anisotropy and compressibility in the IHS (for all periods considered) of V1 data. On the left, variance anisotropy computed as $P[B_j]/E_m$, where $B_j = \{B_\parallel, B_{\perp 1}, B_{\perp 2}\}$. In the same graphs the compressibility $P[|B|]/E_m$ (black curve). On the right, the ratio between the perpendicular component $P[B_\perp] = P[B_{\perp 1}] + P[B_{\perp 2}]$ and the parallel component $P[B_\parallel]$ computed with different methods. CI is the correlation method with linear data interpolation. CS is the compressed sensing spectral estimation. SS is the gap-free subsets. The grey bands in all the pictures represent the uncertainty range and the peaks are due to instrumental interference. (Fraternale et al. 2019a)

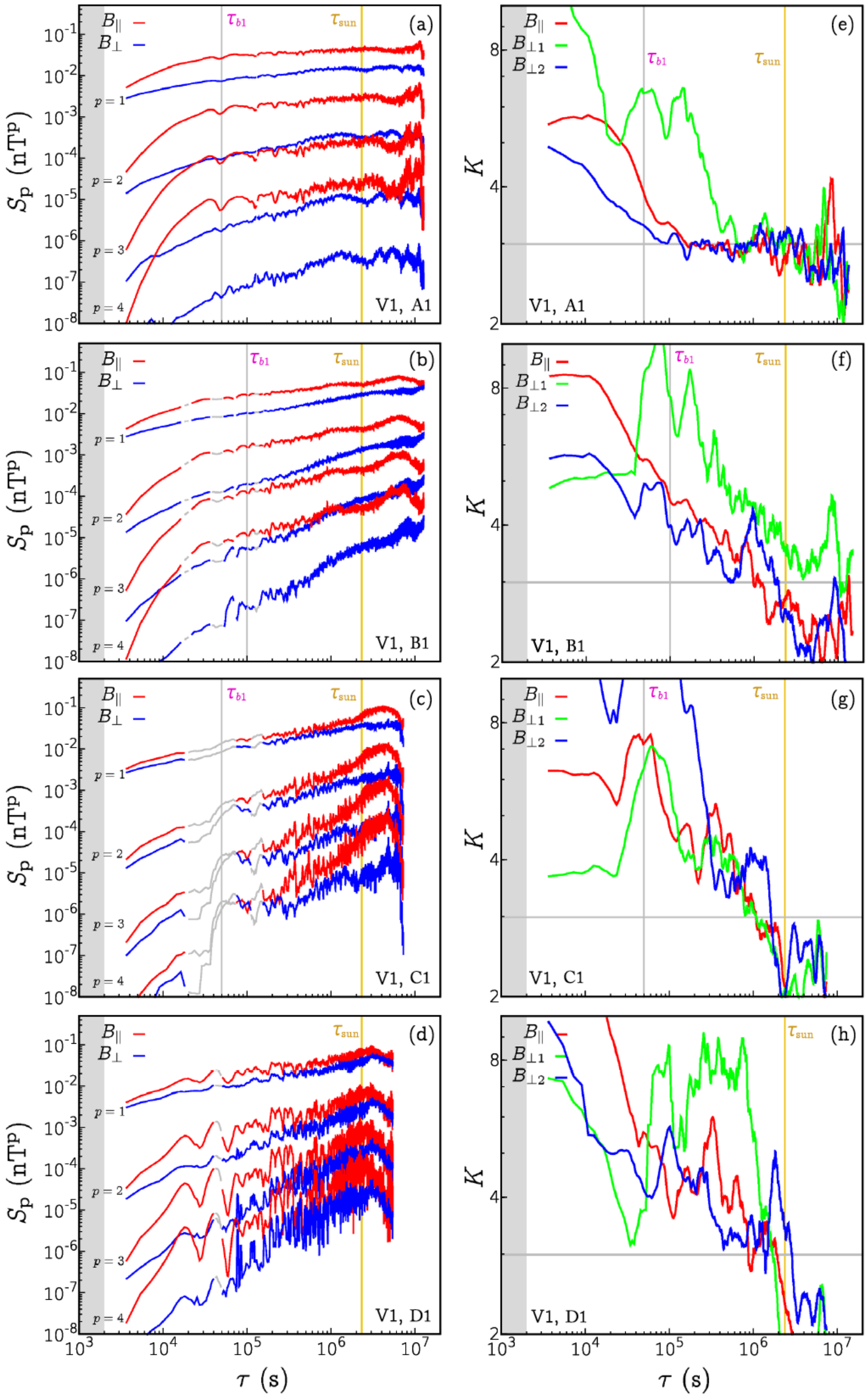

Figure 4.15: On the left, structure functions of the $B_\parallel$ fluctuations (red lines), $S_{p,\parallel}$, and $B_\perp$ ones (blue lines) $S_{p,\perp} = (S_{p,\perp 1} + S_{p,\perp 2})/2$. On the right, Kurtosis of the magnetic field increments showing the intermittent behaviour of the magnetic fluctuations. (Fraternale et al. 2019a)

intervals. The growth starts within the range $\tau \in [10^{-5}, 10^{-6}]$. A particular highlight must be done for the parallel component, which appers to be intermittent before the spectral break (except in the first period).

Different range can be evaluated from the structure functions. An exponent can only be obtained in the high frequency range (low period τ), in which a power law can be recognised. The ESS, indeed, is useful in the whole time range and it allows to compute the related exponents.

It is worth summarising that the shape of the spectra is mostly due to the parallel fluctuations, while the perpendicular ones show the same behaviour which is similar to the Kolmogorov decay in the whole range.

4.4.2 Spectral analysis in the outer heliosheath

Nowadays, the aim of the Voyager probes is to unravel the secrets of the interstellar medium. As said before, the V1 crossed the HP in 2012 and now is moving throughout the outer heliosheat which is the region of the LISM disturbed by the heliosphere. In other words, the OHS is the region of the LISM between the HP and the bow shock/bow wave (Pogorelov et al. 2017a, demonstrated that either the bow shock or the bow wave exists). Burlaga et al. (2015) found that the idea of the draped ISMF can be true and defined the VLISM as the region within 0.01 pc (~ 2000 au). V2 crossed the HP in 2018 and up to now there are no papers discussing its data. This is due to the lack of publicly available data.

Fraternale et al. (2019a), Burlaga et al. (2015, 2018) and Zhao et al. (2020) have worked at V1 data. Meanwhile the latter two focused on the quietest[8] periods, the former studied both quiet (L1 and L3) and disturbed (L2 and L4) intervals.

The data uncertainty is due to the same reasons explained above, moreover the situation gets worse as distance increases. The noise level is unknown, hence a white noise is considered (it is a conservative choice). The noise amplitude is 0.04 nT which corresponds to $P_{noise} \sim 0.05\,\mathrm{nT}^2\mathrm{s}$ and it affects high frequency data up to 4×10^{-5} Hz. It is wothwhile remembering that data are provided in the RTN reference frame, but it is better to use the background magnetic field system.

The turbulence is very weak in the OHS, in fact the intensity of the magnetic field fluctuations is one order of magnitude lower than in the IHS. In order to understand the turbulence origin, it is important to study the quiet intervals. In fact the fluctuations are visible as small perturbation of the magnetic field, therefore periods without disturbances allow to take accurate measurements. Zank et al. (2017) postulated that the turbulence in the outer heliosphere is a superposition of fluctuations coming from the heliosphere through the HP and the pristine interstellar turbulence.

Table 4.10: Averaged magnetic field features in the quiet intervals of the OHS. Interval 3 is the time period considered by Zhao et al. (2020) and it follows the L4 period. (Data provided by Zhao et al. 2020, and reference within).

Interval	B_0[nT]	slope s[nT yr^{-1}]	standard deviation SD[nT]
1	(0.48 ± 0.04)	...	0.0078
2	(0.44 ± 0.02)	(-0.039 ± 0.001)	0.010
3	(0.41 ± 0.01)	(-0.015 ± 0.001)	...

The turbulence in the OHS is curious because the magnetic energy increases in the two later periods (L3 and L4) and the central periods (L2 and L3) are more compressible, in fact $C \sim 0.5$.

[8]The quiet interval is a time period which is free of shocks and other major disturbances.

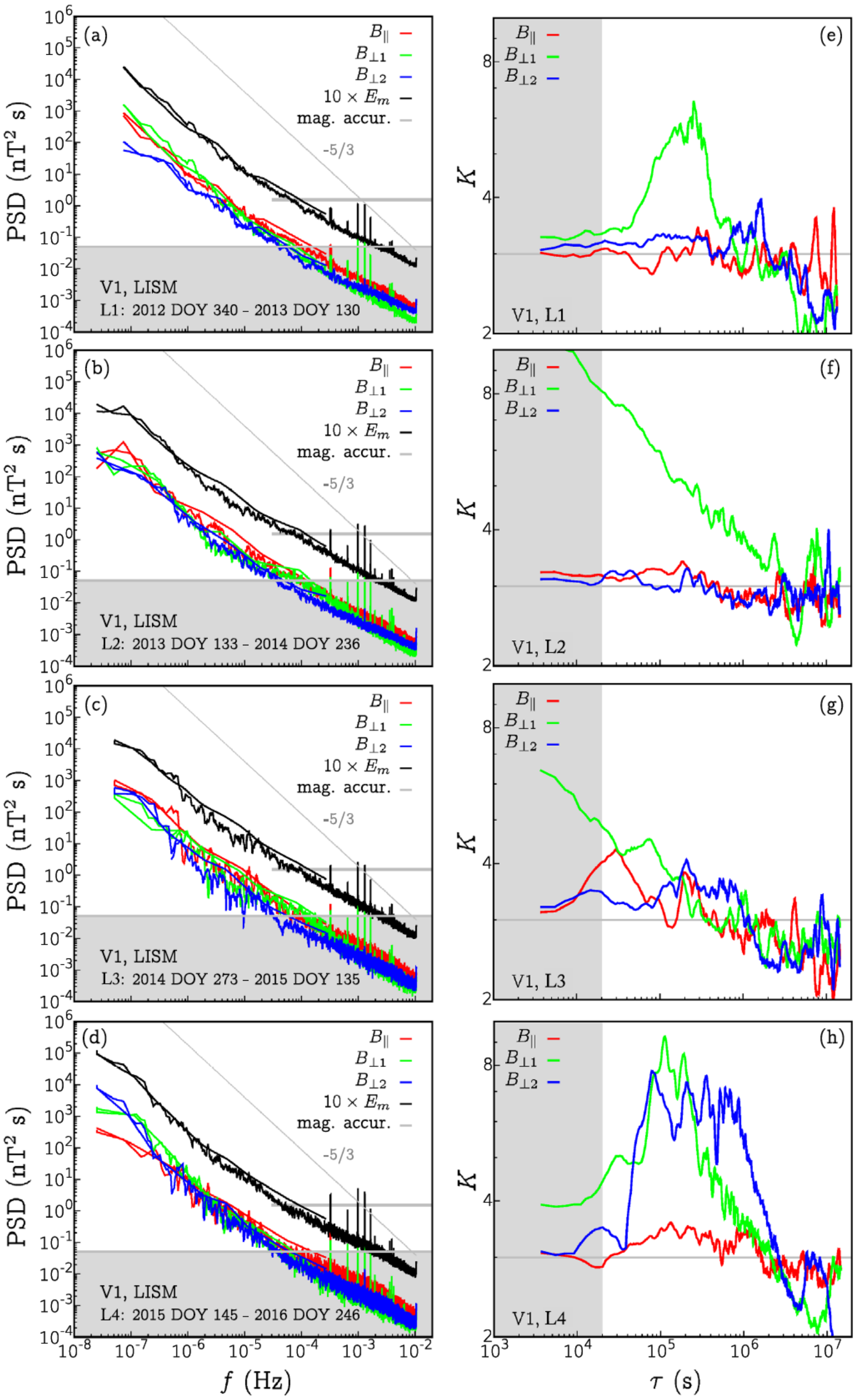

Figure 4.16: V1 48 s data. On the left, the PSD of magnetic field fluctuation components in the four intervals considered. The Taylor's hypothesis is not valid, hence only frequency range is shown. The black curve represents the magnetic energy E_m. On the right, the Kurtosis component of the magnetic field increments for each component is reported. (Fraternale et al. 2019a)

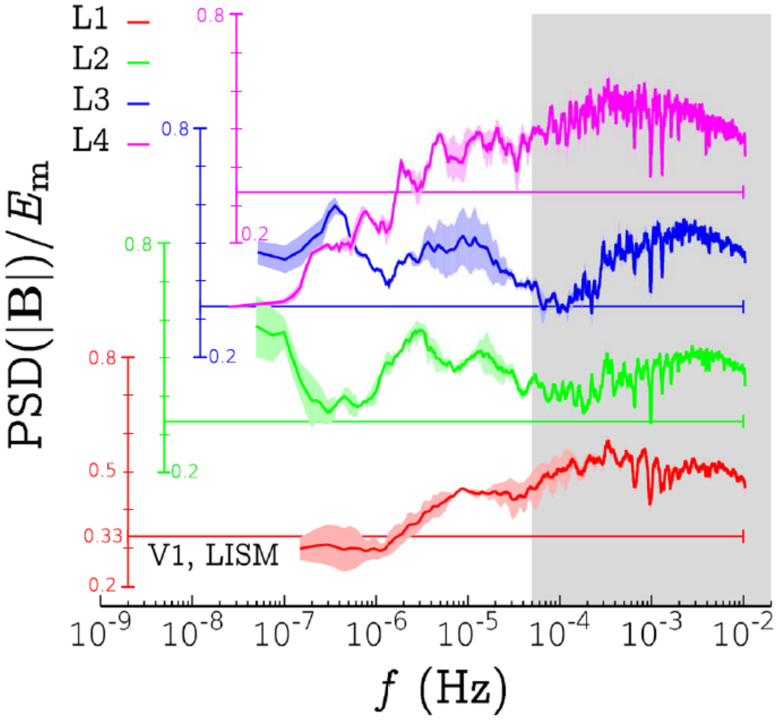

Figure 4.17: V1 spectral compressibility in the OHS. The coloured areas represent the variability between different methods. The grey band is the uncertainty region. (Fraternale et al. 2019a)

It was observed by Burlaga et al. (2015, 2018) that the fluctuating field is initially parallel to the background field, but moving away from the HP the fluctuations become primarily transverse. This is confirmed by the works done by Fraternale et al. (2019a) and Zhao et al. (2020). In particular, looking at figure 4.17, in the low frequencies domain the parallel fluctuations are dominant in the central periods. This increase in the compressibility is probably due to the passage of a shock, since the L2 interval is defined as perturbed.

Table 4.11: Spectral and compressibility data in the OHS from V1 in the four periods considered. The spectral index α are computed in the range frequency $5 \times 10^{-8} < f < 3 \times 10^{-6}$ Hz, thus the errors are larger than those in the IHS. (Fraternale et al. 2019a)

	L1	L2	L3	L4
C	0.30	0.40	0.48	0.12
α	-1.57 ± 0.05	-1.65 ± 0.10	-1.55 ± 0.10	-1.77 ± 0.10
$\alpha_\parallel$	-1.59 ± 0.05	-1.60 ± 0.10	-1.57 ± 0.10	-1.40 ± 0.06
$\alpha_\perp$	-1.54 ± 0.02	-1.60 ± 0.05	-1.54 ± 0.10	-1.90 ± 0.05

At large scale, precisely in the range $5 \times 10^{-8} < f < 3 \times 10^{-6}$ Hz, the magnetic energy E_m follows a Kolmogorv's cascade. It is worthwhile remembering that in the K41 theory the bulk of the fluctuation energy resides at large scales. The spectral index reported in table 4.11 shows good agreement with the Kolmogorov's theory in the quiet intervals (L2 and L4). In the disturbed

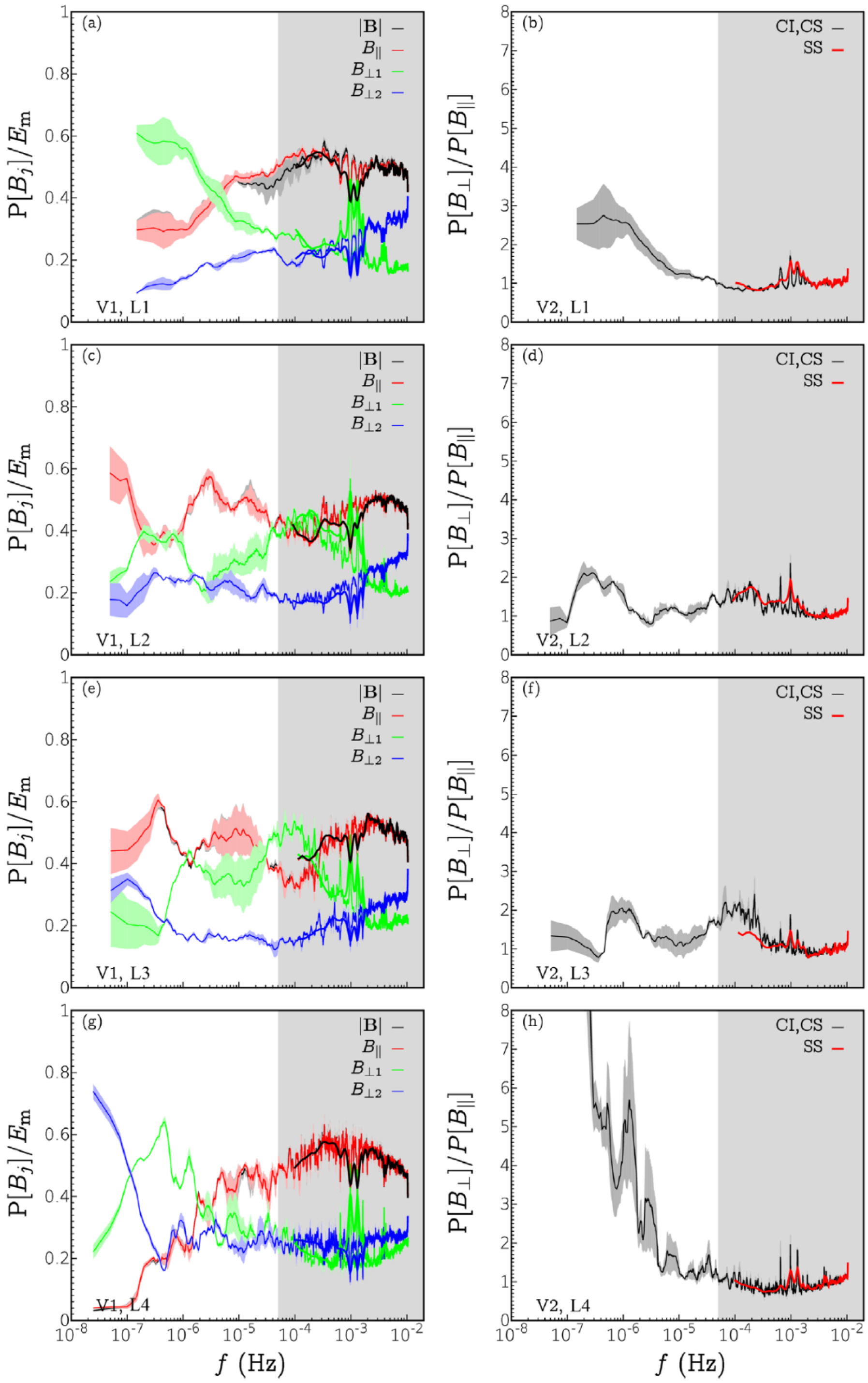

Figure 4.18: V1 48 s. Spectral variance anisotropy and compressibility. The panels description is the same as figure 4.14. (Fraternale et al. 2019a)

periods (L1 and L3) the spectral exponents are lower, i.e. the spectra are flatter at large scales than those of the quiet periods. Attention must be paid; in fact in the L2 interval the spectral break is located at a lower frequency ($f \sim 3 \times 10^{-7}$ Hz), while during L4 the fluctuations change their nature. One may conclude that during L2 the turbulence is either young and locally generated or affected by local structures (as shocks). In the L4, instead, the perpendicular fluctuations presents a much steeper cascade than the parallel ones, therefore something happens to make this change. One possibility is that fast magnetosonic waves pass through the HP and propagate into the OHS after being amplified in the IHS. Then a three interaction mechanism could interven and converts the magnetosonic wave into an Alfvén wave and a convective zero-frequency mode (Zhao et al. 2020). Other possibilities are (i) the presence of a local source of turbulence that becomes more active with time, (ii) the distribution of kinetic and magnetic pressure (the β parameter) changes and affects the parallel and perpendicular fluctuations differently, and (iii) the unwinding of the magnetic field (shown in figure 4.7 through the changing of the δ and λ) could have some effects. However, if the Sun's perturbations transmit through the HP, also the solar activity must be considered.

A flattening is observed at low scales and it coincides with the level of noise considered. Looking at the anisotropy level (see figure 4.14 the grey region), the value is around 0.45 which is high. Moreover, the profiles across the intervals (see figure 4.17) are different. Hence, considering that the white noise tends to uniform these parameters, there is likely less noise than it was assumed.

Finally it must be noted that a small bump occurs in the frequency range $10^{-6} < f < 10^{-5}$ Hz and that the Larmor frequency is one order lower than in the IHS, viz. $f_{cp,LISM} \sim 10^{-4}$ Hz.

A quantification of the quietness is the intermittency, which is a signature of the presence of shock waves or current sheets. The intermittency can be evaluated through the PDF, which is a way to check whether the intervals chosen are quiet. During both the L2 and the L4 intervals there is small intermittency, which means that the turbulence is mostly self-similar. This can be recognised in figure 4.19, where the components of the magnetic field show a shape consistent with the Gaussian distribution. Moreover the values of the Kurtosis, reported in the same figure, are close to 3. Zhao et al. (ibid.) found these values using a time lag of 5 days, hence these values are representative of the large scales. Fraternale et al. (2019a) computed the Kurtosis as a function of frequency (see figure 4.16). At large scales the result obtained by Zhao et al. (2020) is confirmed and the same trend can be extended to the disturbed intervals. At low scales the Kurtosis increases almost in all periods. In the first three intervals, only the $\perp_1$ component shows an intermittent behaviour. During L4 both the perpendicular components exhibit intermittent features, in particular the Kurtosis increases is observed between $10^{-5} < \tau < 3 \times 10^{-6}$ s, where the two components have a steeper spectrum ($\alpha_\perp \sim -1.90$). Anyway, differently from the IHS, no intermittent features are shown by the parallel fluctuations.

The absence of intermittency at large scales could be due to either the passage of shocks or the local production of turbulence. In the former case, the shocks can be seen as a constraint that forces the pristine interstellar fluctuations to become more Gaussian.

Zhao et al. (ibid.) argue that the implicit assumption of stationary state, made using the Fourier method, is not good. Therefore, they used the wavelet and the Hilbert analysis to perform the study of the compressibility as a function of the time. The Hilbert analysis is data adaptive; unlike the wavelet method it sacrifices frequency resolution to preserve the time dependence. The results are almost the same, thus only the results obtained with the Hilbert analysis are shown (figure 4.20 and 4.21).

In the first interval the compressibility is higher than the latter two, which are almost incompressible at large scales. Between the quiet periods there are the perturbed ones, which are more compressive because of some shock events. In the interval 2 (L4) the compressibility is higher in the first 50 days. This is likely due to the shock that occurred in the previous interval. During L2 the compressibility is around $C_B \sim 0.2$ (~ 0.1 for the wavelet method). This means that the fluctuations are almost incompressible, while during L2 the fluctuations are compressible. The

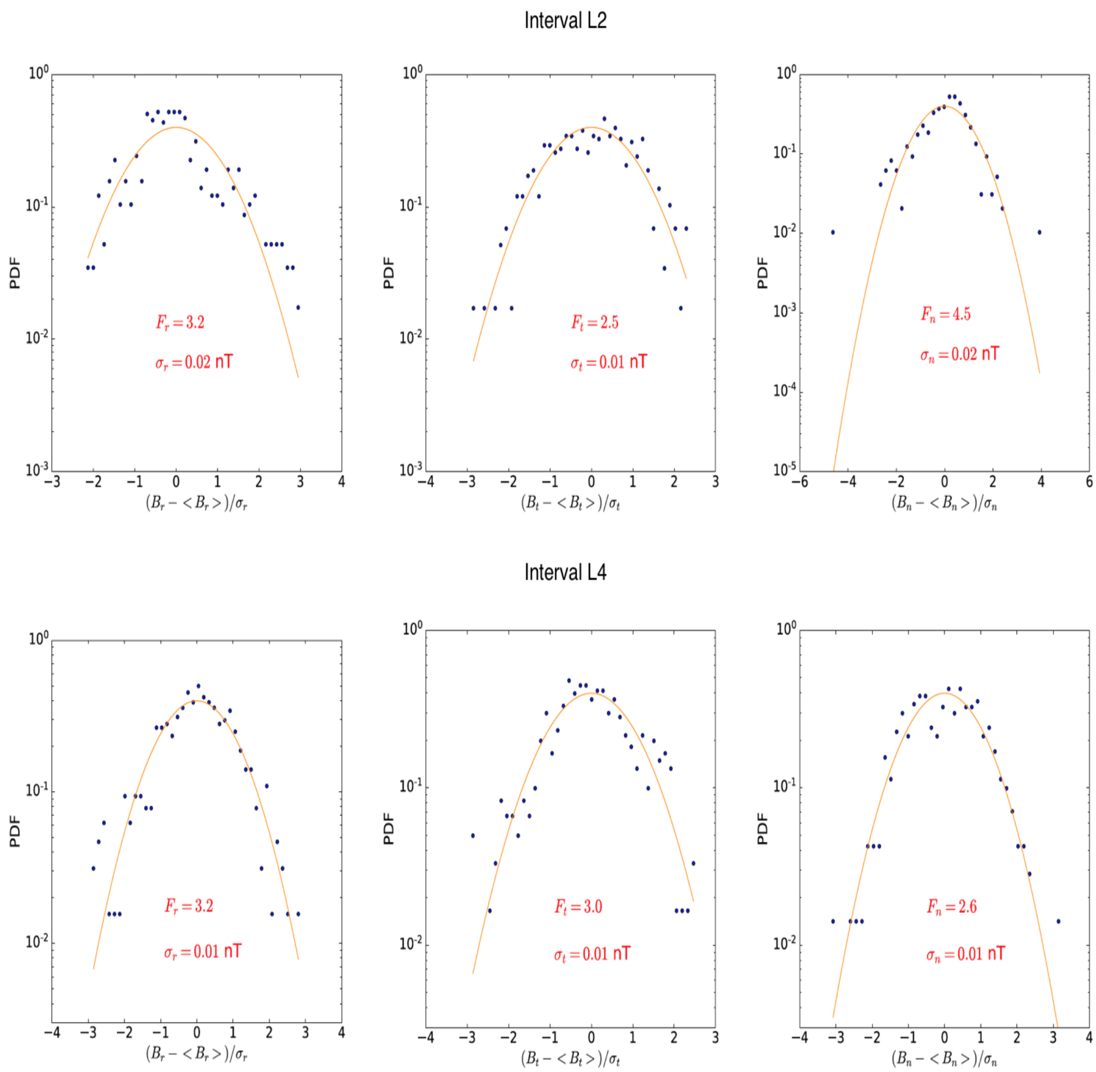

Figure 4.19: PDFs in the quietest intervals in the OHS. The PDFs (dots) are computed for B_R, B_T and B_N respectively. The orange line represents the the Gaussian distribution. For each PDFs the Kurtosis (here F) and the standard deviation σ. (Zhao et al. 2020)

latter period shows the same characteristics as the second period. This analysis is consistent with the Fourier ones, but it allows to highlight the time behaviour. It is worth shedding light to the features of the high frequency scales; indeed when the frequency increases the compressibility also increses. Moreover, at these scales the compressible features of the fluctuations appear as periodic, but the systematic uncertainty and the instrument noise which affects these frequencies does not allow to conclude that this is a physical phenomenon. However, most of the energy is contained at low frequencies, thus the value of C_B at high scales do not change the characteristics observed before.

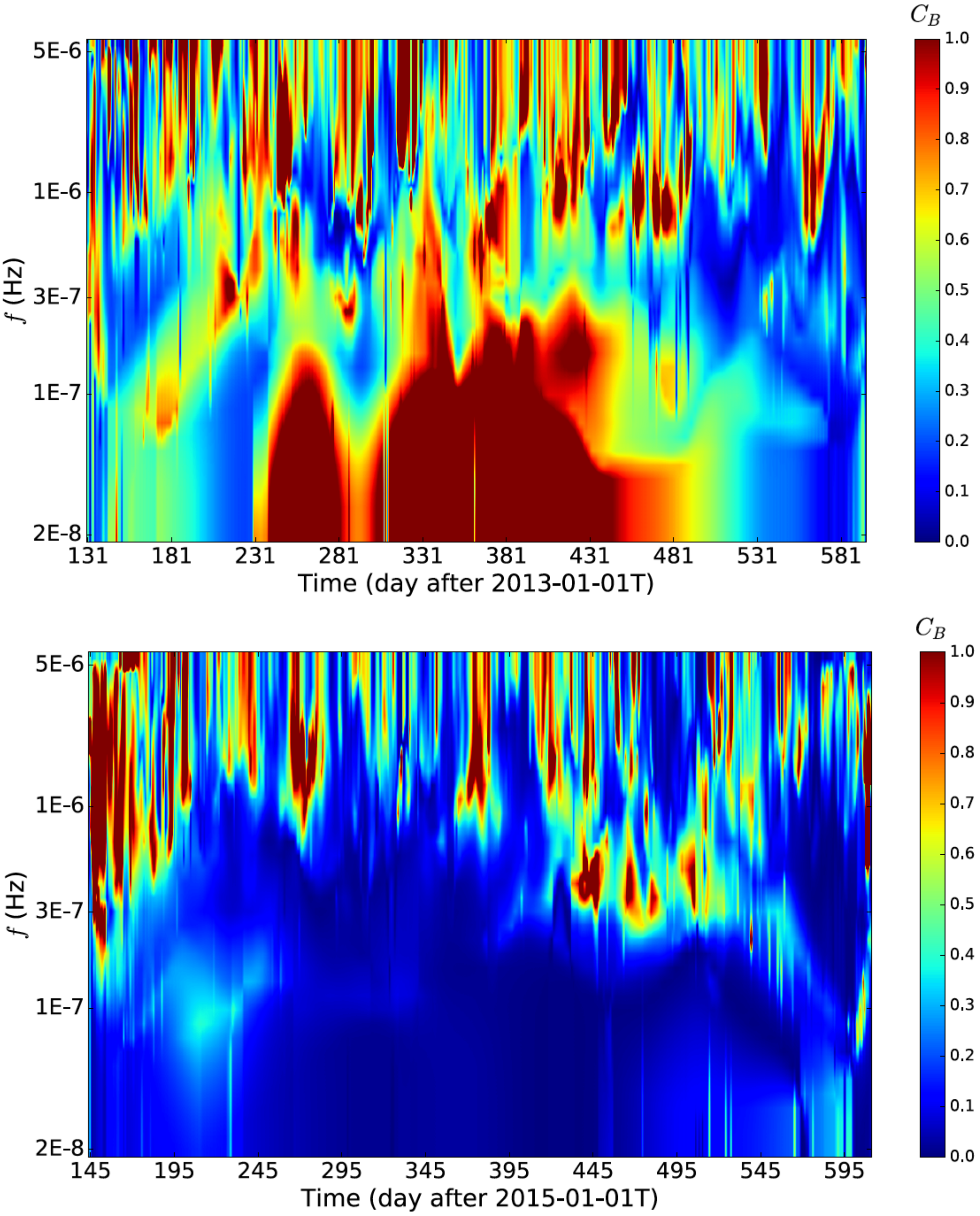

Figure 4.20: Hilbert spectrogram of the magnetic compressibility C_B in the quiet intervals, L2 and L4 respectively. During L2 there is a larger value of the compressibility at large scales with respect to the L4 period. Indeed L2 is characterised by compressible fluctuations, unlike L4 which is incompressible. At small scales the compressibility appears periodic, but uncertainty and noise cannot allow to reach a conclusion. Picture taken from Zhao et al. (2020)

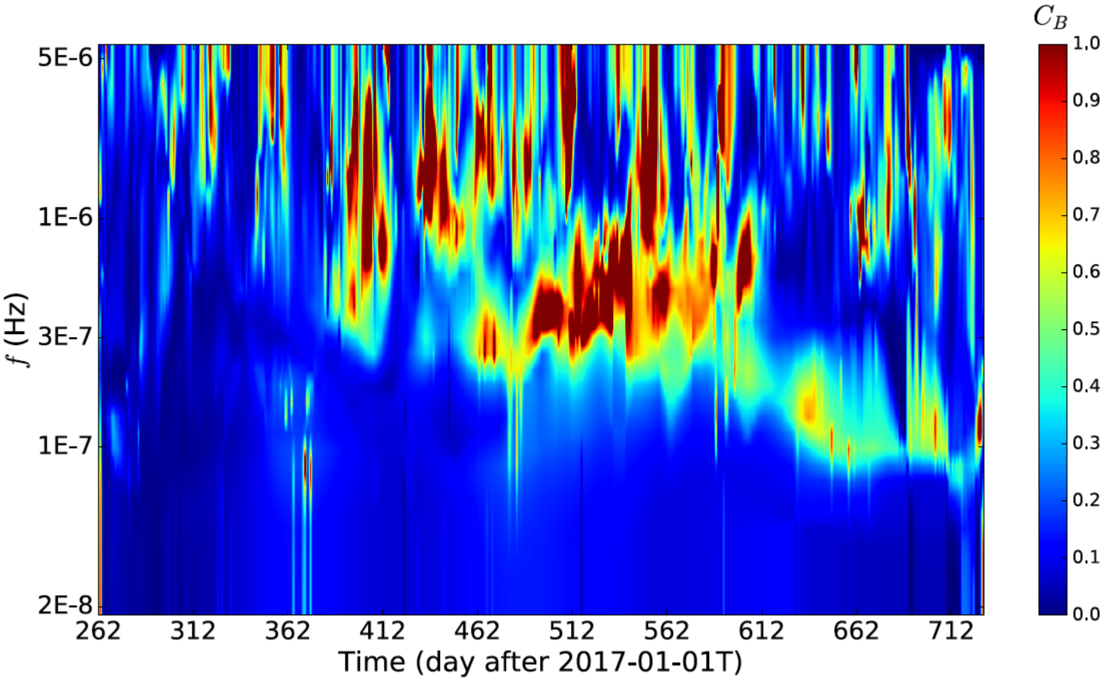

Figure 4.21: Same as figure 4.20, but in the interval 3 (I3) which is the quietest interval after L4 by Zhao et al. (2020). It shows the same feature as the L4 period. (Zhao et al. 2020)

Conclusion

This thesis tries to summarise the major insights about the SW turbulence, which affects the properities of the LISM and has an impact on the heliosphere shape. The work is based on the Voyager probes data at different positions, which confirm or not the theoretical basis proposed at chapter 3. The main problem in these kinds of study is the sparsity of data sets, which increases as well as the distance from the Sun.

The turbulence before the TS has been analysed at 5 au where the V2 was in the slow solar wind region. Assuming the RTN reference system SC as centered, the fluctuations of the velocity are larger than those of the magnetic field in the radial direction (R). In the tangential (T) and normal (N) way, the magnetic field fluctuations appear slightly higher. Through the PSD it is possible to identify both plasma and magnetic field background directions (see figure 4.4-a). The magnetic field is almost perpendicular to the plasma flow direction as expected by Parker's theory. Moreover, the magnetic field fluctuations are incompressible. The energy spectrum of the velocity is compliant with the Kolmogorv's cascade up to $\sim 10^{-4}$ Hz frequency, then the spectrum becomes flatter. The magnetic field, instead, shows a spectral knee at $f \sim 5 \times 10^{-5}$ Hz. Before it, the spectral index is $\alpha \sim -1$ (low frequency range) and then the spectrum becomes steeper $\alpha \sim -1.75$. The first range is called energy injection and it is a reservoir of energy for turbulence. Hence the non linear cascade starts at the spectral knee with the inertial range. Intermittency is experienced at low scales especially in the magnetic field.

In the IHS the magnetic field is still perpendicular to the velocity field and only the first has been analysed. Hence, the reference frame used was the background magnetic field. Data provided by V2 allows to identify the EI and IC, while the kinetic regime is probably in the last decade ($10^{-3} < f < 10^{-2}$ Hz) where the level of noise does not let discuss it. The EI is characterised by a power law of $\alpha \sim -1$, low compressibility and it is not intermittent. The EI ends at f_{b1}, whose value depends on the period considered. However the EI is wider in the UHS which can be due to the more Alfvénicity of these periods. Differently from the interplanetary field, the IC range shows two subranges separated by a second spectral knee f_{b2}. At this frequency the intermittency and compressibility reach the maximum value. However, unipolar periods are featured by a faster energy decay. In the IC regime, the average spectral index appears consistent with the Kolmogorv's law as the one computed at 5 au.

V1 mostly travelled in the unipolar region, but its data are complicated to discuss because the Plasma Science instrument does not work, hence there are no accurate velocity data. Moreover, the low velocity of the SW does not allow using the Taylor's hypothesis.In other words, distinguishing the waves from active turbulence becomes more difficult. The compressibility is higher than that revealed by V2, indeed most of the energy resides in the parallel fluctuations. V1 unravels only one spectral knee f_{b1} that divides the EI from the IC. At large scales the power law decay follows f^{-1} as measured by V2 before the TS and in the IHS. Instead, the IC is steeper than the V2 case, with $\alpha \sim -2.5$. Both compressibility and intermittency change with the frequency. The first reaches its maximum at the spectral break, while the latter starts its growth before the knee.

Only the V1 data are available in the OHS, therefore neither velocity data nor the frozen-in condition can be used. The fluctuation intensity is one order lower than in the IHS and near the HP the turbulence is mostly compressible; in fact the most part of the energy resides in the parallel fluctuations. Increasing the distance from the HP, the nature of the fluctuations change and the perpendicular energy increases. The compressibility decreases with distance growth. The intermittency is only observed in the perpendicular fluctuation. The spectra of the energy decay as the Kolmogorov's law in the range $5 \times 10^{-8} < f < 3 \times 10^{-6}$ Hz and there are no spectral breaks. The small frequency range available does not permit to distinguish between the EI and the IC. The observed OHS turbulence is locally modified by the periodic passage of shocks. Finally, the slope observed in the value of the magnetic field magnitude and of both the azimuthal and the elevation angles, allow thinking that the ISMF is draped around the heliosphere.

Anyway, the data available up to now are not enough to fully understand the magnetic turbulence and the main features of the LISM. New insights can be provided by V2 data, allows studying the plasma velocity more accurately. Moreover, the study conducted by Zhao et al. (2020) leads to wonder whether the Hilbert (or the wavelet) method, which allows to consider the time domain, actually helps to better understand the interaction between the interstellar medium and the heliosphere. Surely, the new works should contemplate the effects of the ENA and of the PUIs on the energy exchange and on the transport properties.

Bibliography

Balogh, A. and R. A. Treumann (2013). "The Heliospheric Termination Shock". In: *Physics of Collisionless Shocks*. Springer, pp. 463–494.

Bemporad, A. (2019). *Elementi di Eliofisica e Meteorologia Spaziale*. PowerPoint slides.

Bruno, R. and V. Carbone (2013). "The solar wind as a turbulence laboratory". In: *Living Reviews in Solar Physics*.

Burlaga, L. F., V. Florinski, and N. F. Ness (2015). "In situ observations of magnetic turbulence in the local interstellar medium". In: *The Astrophysical Journal Letters* 804.2, p. L31.

— (2018). "Turbulence in the outer heliosheath". In: *The Astrophysical Journal* 854.1, p. 20.

Burlaga, L. F., N. F. Ness, and J. D. Richardson (2017). "Transition from the unipolar region to the sector zone: Voyager 2, 2013 and 2014". In: *The Astrophysical Journal* 841.1, p. 47.

Chiuderi, C. and M. Velli (2012). *Fisica del Plasma: Fondamenti e applicazioni astrofisiche*. Springer Science & Business Media.

Czechowski, A., M. Bzowski, J. M. Sokół, M. A. Kubiak, J. Heerikhuisen, E. J. Zirnstein, N. Pogorelov, N. A. Schwadron, M. Hilchenbach, J. Grygorczuk, et al. (2019). "Heliospheric structure as revealed by the 3–88 keV H ENA spectra". In: *The Astrophysical Journal* 888.1, p. 1.

Fraternale, F., L. Gallana, M. Iovieno, M. Opher, J. D. Richardson, and D. Tordella (2016). "Turbulence in the solar wind: spectra from Voyager 2 data at 5 AU". In: *Physica Scripta* 91.2, p. 023011.

Fraternale, F., N. V. Pogorelov, J. D. Richardson, and D. Tordella (2019a). "Magnetic turbulence spectra and intermittency in the heliosheath and in the local interstellar medium". In: *The Astrophysical Journal* 872.1, p. 40.

— (2019b). "The structure of magnetic turbulence in the heliosheath region observed by Voyager 2 at 106 AU". In: *Journal of Physics: Conference Series*. Vol. 1225. 1. IOP Publishing, p. 012006.

Gallana, L., F. Fraternale, M. Iovieno, S. M. Fosson, E. Magli, M. Opher, J. D. Richardson, and D. Tordella (2016). "Voyager 2 solar plasma and magnetic field spectral analysis for intermediate data sparsity". In: *Journal of Geophysical Research: Space Physics* 121.5, pp. 3905–3919.

Hill, M. E., R. B. Decker, L. E. Brown, J. F. Drake, D. C. Hamilton, S. M. Krimigis, and M. Opher (2014). "Dependence of energetic ion and electron intensities on proximity to the magnetically sectored heliosheath: Voyager 1 and 2 observations". In: *The Astrophysical Journal* 781.2, p. 94.

Iovieno, M., L. Gallana, F. Fraternale, J. D. Richardson, M. Opher, and D. Tordella (2016). "Cross and magnetic helicity in the outer heliosphere from Voyager 2 observations". In: *European Journal of Mechanics-B/Fluids* 55, pp. 394–401.

Izmodenov, V. V. and R. Kallenbach (2006). *The physics of the heliospheric boundaries*. ESA Publications Division.

Magyar, N., T. Van Doorsselaere, and M. Goossens (2019). "The Nature of Elsässer Variables in Compressible MHD". In: *The Astrophysical Journal* 873.1, p. 56. DOI: 10.3847/1538-4357/ab04a7. URL: https://doi.org/10.3847%2F1538-4357%2Fab04a7.

Matthaeus, W. H. and M. L. Goldstein (1982). “Stationarity of magnetohydrodynamic fluctuations in the solar wind”. In: *Journal of Geophysical Research: Space Physics* 87.A12, pp. 10347–10354.

Numata, R. (2018). *Magnetic reconnection*. URL: https://rnumata.org/research/recon.

Parker, E. N. (1955). “Hydromagnetic dynamo models.” In: *The Astrophysical Journal* 122, p. 293.

Pogorelov, N., S. N. Borovikov, J. Heerikhuisen, and M. Zhang (2015). “The heliotail”. In: *The Astrophysical Journal Letters* 812.1, p. L6.

Pogorelov, N., J. Heerikhuisen, V. Roytershteyn, L. F. Burlaga, D. A. Gurnett, and W. S. Kurth (2017a). “Three-dimensional features of the outer heliosphere due to coupling between the interstellar and heliospheric magnetic field. V. The bow wave, heliospheric boundary layer, instabilities, and magnetic reconnection”. In: *The Astrophysical Journal* 845.1, p. 9.

Pogorelov, N., J. Heerikhuisen, G. P. Zank, S. N. Borovikov, P. C. Frisch, and D. J. McComas (2011). “Interstellar boundary explorer measurements and magnetic field in the vicinity of the heliopause”. In: *The Astrophysical Journal* 742.2, p. 104.

Pogorelov, N., H. Fichtner, A. Czechowski, A. Lazarian, B. Lembège, J.A. Le Roux, M.S. Potgieter, K. Scherer, E. C. Stone, R. D. Strauss, et al. (2017b). “Heliosheath processes and the structure of the heliopause: modeling energetic particles, cosmic rays, and magnetic fields”. In: *Space science reviews* 212.1-2, pp. 193–248.

Sims, D. (2010). *IBEX Mission Changes its SOCs*. URL: http://www.eos.sr.unh.edu/newsl_1110/ibex.shtml.

Smith, C. W., K. Hamilton, and B. J. Vasquez (2005). “Variance anisotropy in the inertial range”. In: *Solar Wind 11/SOHO 16, Connecting Sun and Heliosphere*. Vol. 592, p. 551.

Tan, B. (2009). “A Physical Explanation on Solar Microwave Zebra Pattern with the Current-carrying Plasma Loop Model”. In: *Astrophysics and Space Science* 325. DOI: 10.1007/s10509-009-0193-5.

Turner, A. J. (2013). “Turbulence in the solar wind”. URL: http://wrap.warwick.ac.uk/57960/.

Vlahos, L. and P. Cargill (2009). *Turbulence in space plasmas*. Vol. 778. Springer.

Zank, G. P., S. Du, and P. Hunana (2017). “The origin of compressible magnetic turbulence in the very local interstellar medium”. In: *The Astrophysical Journal* 842.2, p. 114.

Zell, H. (2013). *The Heliospheric Current Sheet*. URL: https://www.nasa.gov/content/goddard/heliospheric-current-sheet.

Zhao, L. L., G. P. Zank, and L. F. Burlaga (2020). “Turbulence in the Very Local Interstellar Medium (VLISM)”. In: *The Astrophysical Journal* 900.2, p. 166.